Risö Report No. 195

3 Cef

RECEIVED BY DTIE AUG 7 1969

Risö Report No. 195

MASTER

Danish Atomic Energy Commission
Research Establishment Risö

A 4 πβ-Spectrometer with Li-Si Counters

by Verner Andersen

March, 1969

Sales distributors: Jul. Gjellerup, 87, Sölvgade, DK-1307 Copenhagen K, Denmark
Available on exchange from: Library, Danish Atomic Energy Commission, Risö, DK-4000 Roskilde, Denmark

U. D. C.
539.124.164:539.1.074.7

DISCLAIMER

March, 1969 Risö Report No. 195

A $4\pi\beta$-Spectrometer with Li-Si Counters

by

Verner Andersen

Danish Atomic Energy Commission
Research Establishment Risö
Physics Department

Abstract

A $4\pi\beta$-spectrometer has been developed. It is provided with solid-state detectors placed in a magnetic field from a superconducting magnet. The resolution is 0.8% at 1 MeV. The instrument has been used to measure conversion coefficients of different gamma transitions:

^{207}Bi: 570 keV,

$\alpha_K = 0.0160 \pm 3.0\%$, $K/L = 3.45 \pm 10\%$, $L/M \ldots = 2.63 \pm 20\%$

1064 keV,

$\alpha_K = 0.094\ (\pm 10\%)$; $K/LM \ldots = 3.37 \pm 10\%$

^{198}Au: 412 keV,

$\alpha_{total} = 0.046\ (\pm 5\%)$

^{203}Hg: 279 keV,

$\alpha_K = 0.127$; $K/L = 3.28 \pm 4\%$; $L/M \ldots = 3.26 \pm 8\%$.

These values are compared with other existing theoretical and experimental values. Furthermore the instrument has been used for measuring the beta shape of ^{32}P, ^{198}Au and ^{203}Hg.

This report was written in partial fulfilment of the requirements for obtaining the Ph. D. (lic. techn.) degree.

CONTENTS

1. INTRODUCTION

For many years the only precision instruments suitable for measuring electron spectra have been the magnetic spectrometers. The main shortcomings of these instruments are

(1) Small solid angle, giving little transmission;

(2) The necessity of scanning the spectrum in many steps, which is time consuming and demands correction for decay of the source;

(3) Difficulties arising from distortion of the spectrum due to scattering of electrons in the necessary baffles;

(4) The solid-angle determination is very difficult and wanting in accuracy.

The invention of proportional and scintillation counters only partly solved these problems. These counters are highly sensitive to γ-rays, and unless internal-source geometry is used, heavy backscattering distortions are unavoidable.

Magnetic fields constraining the electrons into helical paths have been used successfully to overcome many of these problems. Holloway et al.1) have described a long, high-pressure proportional counter with an axial magnetic field.

At this laboratory another approach has been used2). Two scintillation counters were placed as top and bottom of a long field-line tube in a homogeneous magnetic field. This spectrometer has been used for some years in connection with measurements of the neutron half-life. However, it has a rather bad resolution.

With reasonably large solid-state detectors available, the said principle can be used in the design of a spectrometer that has a rather good resolution. We have built an instrument based on this principle.

Considering the resolution of our instrument, it is reasonable to compare it with magnetic spectrometers. We obtained a resolution (fwhm) of better than 1% at 1 MeV. A magnetic spectrometer of comparable resolution would typically have a transmission of about 10%, which gives our design an advantage of a factor of ten. To this must be added that for a spectrum measured with a magnetic spectrometer, 50-100 runs would be needed to give the same information as one run with our system using a multichannel analyser. Furthermore it is not necessary in our system to correct for decay of the source because all energies are measured simultaneously.

The high efficiency because of the 4π-geometry allows us to use very weak sources, so that scattering and absorption in the source are minimized. At the same time dead-time corrections and random coincidences are greatly reduced.

The solid angle is very well defined. In so far as absorption in the source backing and the detector window - giving spectrum distortion - can be neglected, the solid angle is 100%. When the two detectors are operated in parallel, their backscattering effect is eliminated. Thus there will be a synonymous connection between the energy of the electron and the channel numbers of the multichannel analyser. At the same time the solid angle of 100% will make the instrument applicable for absolute counting. Besides the instrument has been used to measure conversion ratios for ^{207}Bi, ^{198}Au and ^{203}Hg. With the decay type of ^{207}Bi this can be done with a very high accuracy. Also its ability to measure beta shapes has been demonstrated.

2. DESCRIPTION OF THE INSTRUMENT

The principle of the system is that mentioned above for the instrument used to measure the neutron half-life. Two semiconductor detectors (Li-Si-detectors) are placed as top and bottom of a field-line tube in a nearly homogeneous magnetic field from a superconducting magnet. The set-up with the two detectors placed on the axis at either end of the magnet is illustrated in fig. 2.1, which also shows the position of the source midway between the detectors. The 4π-geometry may be obtained by sandwiching the source between the detectors, but with the set-up used the electron-to-gamma efficiency can be improved by more than a factor of 100 because the electrons, beta particles or conversion electrons, will fly in helical orbits to one of the two detectors owing to the magnetic field. The mounting of the detectors and the source is seen in the sketch in fig. 2.2, which gives the dimensions of the counting chamber. We have three sets of detectors: two commercial sets, 2 cm^2 in sensitive area and respectively 3 and 5 mm in sensitive thickness. The third set, which was made in the Health Physics Department of the Research Establishment Risö, is approximately 0.7 cm^2 in sensitive area and 3 mm in sensitive thickness. This sets makes it possible to change the distance between the detectors from nearly zero to 15 cm by using different sets of mounting tubes. The 2 cm^2 detectors can be mounted in the way shown in fig. 2.2 only. The reason for having different thicknesses of the detectors is discussed in a later section.

The source, which is carrier free to avoid scattering and absorption of the electrons, is placed on a VYNS-film ($35\,\mu g/cm^2$) mounted in a ring of aluminium.

The total disassembled system is seen in fig. 2.3. The material of the counting chamber, seen at the bottom of the system, is copper because good thermal and electrical conductivity is wanted. The supporting tube is made of stainless steel and insulated from the counting chamber because of noise problems and to allow measurement of the leakage current of the detectors. All the connections from the chamber, including thermocouples and heating elements, to the top of the system are led through thin monel tubes inside the stainless-steel tube. The choice of materials, stainless steel and monel, aims at minimizing the heat conduction from the top to the bottom of the system. The counting chamber is insulated from a surrounding burnished shield of stainless steel, which is in electrical contact with the supporting steel tube. The shield is thus used as an electrical shield for the chamber as well as a thermal shield between the chamber and the outer wall, which is of stainless steel and in direct contact with the helium bath necessary to run the superconducting magnet. The length of the whole system is adjusted so that the source is placed precisely at the centre of the magnet.

When the total system with dewars is built up in the way shown in fig. 2.4, it is possible to mount or dismount the evacuated system without heating the cryostat including the magnet. The source may therefore be replaced relatively fast.

The electrical set-up used for the results published earlier3) is that seen in fig. 2.5. The wires for thermocouples and heating elements are not shown. The voltage across one of the detectors may be measured between C1 and C2 with the switch S2 in the position wanted, because the resistance of the cooled detector in the bias direction is great compared with the resistances in the circuit. The leakage current of the detectors is measured by the voltage drop between C3 and C2. Both the control box and the top box contain filters to remove ripple from the voltage if any.

The necessary voltage at the detectors may vary from about 400 to about 1700 V according to the detectors used. The wire used for this purpose is a 0.1 mm Cu wire with a special teflon insulation tested to 2500 V.

The signal from the detectors was transmitted as seen in fig. 2.5 with the preamplifiers at the top of the system. The resolution of the preamplifier is highly dependent on the capacity at the preamplifier input, which should therefore be kept as small as possible. It has a fwhm of 3 keV at 0 pF and rises by 0.1 keV/pF. For this reason, special low-capacitance coax cables were constructed to be used instead of ordinary commercial coax cables, which have about 40 pF/m. The cables consisted of a 0.1 mm Cu wire stretched along the axis of a 6 mm monel tube. In this way a capacity of about 13 pF/m was obtained. Because of stray capacities all over the system, especially in the counting chamber, the total capacity to each preamplifier, derived from the system without detectors, was about 30 pF. To this was added the detector capacity, which may be calculated approximately as the capacity of a disc condensor with $\varepsilon_r \approx 12$ for Si-detectors.

With this system we had with a single detector a fwhm of 12 keV for 976 keV electrons. Later this resolution was improved by a factor of more than 2 by reconstruction of the preamplifiers discussed in a later section.

2.1. The Detectors

As mentioned above, the half-life instrument[2)] used scintillation detectors, which are energy sensitive. This is a great advantage because it makes it possible to measure the whole spectrum in one operation with a multichannel analyser. At the same time the scintillation detectors in a homogeneous magnetic field have a very high efficiency because of the 4π-geometry.

On the other hand they have rather big dimentions, and the phototube cannot work in strong magnetic fields. The latter problem can be overcome either by magnetic shielding of the phototube or by withdrawing it from the field by the aid of light conductors. Furthermore the resolution of a scintillation detector is not too good.

All these difficulties have been overcome by the semiconductor detectors, which have the following advantages[4)]:

1. excellent energy resolution;
2. linear response over a wide range of particle types and energies;
3. insensitivity of pulse height to counting rate;
4. small intrinsic gamma efficiency;
5. small size and ease of handling;
6. insensitivity to magnetic fields;
7. ability to operate at low temperatures;
8. high stopping power per unit volume;
9. ruggedness against thermal shock.

Semiconductor detectors depend on the production of free carriers in crystals by the interaction of incident particles with bound electrons. These detectors are analogous to the well-known gaseous ionization chambers. In an ionization chamber the incident particle produces electron - ion pairs; in a solid, the incident particle produces electron - hole pairs. Detection of the incident particle is then a problem of collection of the liberated charge by application of an electric field.

An important difference between the solid and the gas is that many more electron - hole pairs are produced in the solid than electron - ion pairs in the gas per unit energy of the particle. The average energy required to produce an electron - ion pair for instance in argon is 26.4 eV, while the average energies required to produce an electron - hole pair in silicon and germanium are 3.55 and 2.94 eV respectively. These two materials are the only ones from which it is possible to-day to produce single crystals of sufficient purity and crystal perfection to be suitable for semiconductor detectors. The lower average energy leads to a smaller fractional statistical fluctuation in the number of carriers produced and hence to a potentially higher resolution in the measurement of the energy of the incident particle.

Such a comparison, however, is not strictly correct, but has to be corrected by the Fano factor F, which for argon has been measured to be 0.22, while observations on silicon indicate a value less than 0.5[4)]. The Fano factor is introduced by the equation

$$\langle (J - J_o)^2 \rangle_{Av} = F J_o ,$$

where J is the number of electron - hole pairs produced and J_o is the mean value of J. For F = 1 the equation will satisfy a Poisson distribution. The reason for a correction of this is that particles must lose an exact amount of energy when they come to rest in the sensitive part of the detector.

Having realized the advantage of using semiconductor detectors, we must choose among four different types:

1. surface-barrier detectors (silicon);
2. diffused-junction detectors (silicon);
3. lithium-compensated silicon detectors;
4. lithium-compensated germanium detectors.

We want for instance to measure the conversion electrons of 570-keV and 1064-keV decay in ^{207}Bi. When the particle has to give up all its energy in the sensitive volume of the detector, we need in the case of the high-energy decay a depletion layer, which is the sensitive layer, of about 2 mm. In the case of ^{32}P we need to stop beta particles with energies up to 1708 keV, which demands a depletion layer of about 4 mm. Depletion layers of this thickness are only possible in lithium-compensated detectors, also called lithium-drifted detectors.

For a diffused-junction detector with p-type silicon as the bulk material the depletion layer is $W \simeq 0.32\ (\rho v)^{1/2}$ microns$^{5)}$. ρ is the resistivity (100-10 000 ohms cm) of the p-type material, and V is the voltage. In case of n-type silicon as bulk material, which might be used in diffused-junction detectors and is always used in surface-barrier detectors, the depletion layer is 50-80% deeper for a given voltage, depending on the resistivity$^{5)}$. The upper limit to the sensitive thickness of surface-barrier detectors is about 2 mm.

In our case the lithium-drifted silicon detector is preferred for several reasons. We want low sensitivity to γ-rays; this requires a low value for Z, which is 14 for silicon and 32 for germanium. The photoelectric cross section has a Z^5 dependence, the pair-production cross section has a Z^2 dependence (threshold about 1 MeV), and the Compton effect has a Z dependence. Furthermore it is of great importance in detecting electrons that the window of the detector is as thin as possible to avoid distortion in the spectra owing to absorption. In silicon detectors the window may be made as thin as 0.2 μ; in germanium detectors, on the other hand, it is usually thicker to give more mechanical strength, as these detectors are generally used for gamma rays, for which the thin window is not needed. Also practical reasons count in favour of silicon detectors, which can be stored at atmospheric pressure at room temperature and without bias. Germanium detectors have to be kept at low temperatures and preferably with bias to preserve their properties. These circumstances would demand a much more complicated system to make source changes possible.

As mentioned above, the detector has to be sufficiently thick to stop the particles completely to avoid distortion of the spectrum. If on the other hand the detector is thicker than needed, it will introduce unnecessary noise because one of the noise contributions is proportional to the volume of the detector. This is why we have detector sets of different thicknesses. To be sure to avoid the first-mentioned effect we have used 3-mm detectors for energies up to 1 MeV and 5-mm detectors up to 2 MeV. The expected electron ranges in Si at the two energies are 2 and 4.5 mm respectively.

The detector noise is generated by fluctuations in the leakage currents arising both from the detector surface and from the detector volume. The surface-generated leakage current arises in the region where the strong electric field in the depletion layer reaches the detector surface, and it is highly dependent on the surface treatment of the detector. The bulk leakage current, which is produced by the inverse of carrier recombination, may be reduced by cooling the detector. In general we have used the detectors at about 100°K, where the total current for a detector with an area of 1.0 cm^2 and a depletion depth of 3 mm is of the order of 10^{-9} amps.

Another disadvantage of the semiconductor detectors is the trapping effect, which leads to distortion of the spectra. This effect comes from imperfections in the crystal lattice, which may be structural defects or chemical impurities. The trapping cross section of such imperfections depends on complex factors that are not well understood and may vary considerably from one type of imperfection to the other. Experience shows that the trapping decreases with increasing temperature; therefore the choice of temperature must be a compromise based on trapping effect and leakage currents. The trapping effect is also dependent on the time it takes for the carrier to be collected and thus on the velocity μE of the carrier. It will therefore decrease with increasing voltage across the detector. In a spectrum of monoenergetic electrons the trapping effect will appear as a tail to the peak as seen in the spectrum for ^{207}Bi (fig. 3.4), which is discussed later. The dependence of such a tail on temperature and voltage is seen in figs. 3.7 and 3.8 respectively.

To provide the possibility of testing a detector without the use of the spectrometer, which might at the time operate with other detectors, a separate test chamber as shown in fig. 2.1.1 was built. In order that the noise might be decreased, the chamber was built with double shielding. The lead-in bushes, made of glass, had to be covered with black wax because the detectors are sensitive to light. This sensitivity does not matter when the detector is mounted in the spectrometer.

2.2. The Preamplifiers

As said before, the signal from the detectors was transmitted via special low-capacity coax cables to the preamplifiers at the top of the system. Each detector has its own preamplifier for several reasons. The main reason is that we have seen that two detectors may give slightly different pulse heights; if the signals are added inside the system, we have no possibility of correcting for this, and a peak corresponding to a particular energy of the electrons will split up into a double peak in the pulse-height analyser. Another reason is that we have a better possibility of seeing the signal from one detector alone because in a parallel set-up with the signals added inside the system this is only possible by reducing the bias at the other detector, but in that case the latter detector will give a not negligible contribution of noise.

The preamplifiers used were "Nuclear Enterprises NE 5283". They are charge-sensitive preamplifiers, most commonly used for semiconductor detectors because the output pulse height is independent of the capacity connected to the input of the amplifier. This is not the case with the noise contribution as discussed earlier in section 2. The capacity to the input is not stable because the capacity of a semiconductor detector varies more or less with the applied bias according to the type of detector used. The circuit configuration of the charge-sensitive part of the preamplifier is seen in fig. 2.2.1a, where

$C_t = C_d + C_s$
C_d = total detector capacity
C_s = stray capacity
C_k = coupling capacity
C_f = feedback capacity
R_1 = detector bias resistor
R_2 = input resistor in the preamplifier.

Using fig. 2.2.1 b, where $C_p = C_f(1 - A) \simeq -AC_f(|A| \gg 1)$, we have fig. 2.2.1 c with the signal flow graph fig. 2.2.1 d, from which we have

$$\frac{v_3}{q} = \frac{j\omega C_k R_2 A/C}{1 + j\omega C_p R_2 + j\omega C_k R_2} \simeq \frac{C_k A/C}{-AC_f + C_k} ,$$

where

$$C = C_t + \frac{-C_k AC_f}{C_k - AC_f} \simeq \frac{-C_k AC_f}{C_k - AC_f} .$$

From this we obtain

$$\frac{v_3}{q} \simeq -\frac{1}{C_f} \qquad \text{or} \qquad \underline{v_3 \simeq -\frac{q}{C_f}} .$$

The result shows that the output depends only on the feedback capacity and not on the detector capacity or stray capacity provided these are small compared with C_k and AC_f; this is usually the case. The other assumption, that $\omega R_2(AC_f + C_k) \gg 1$, will also be fulfilled with an FET as the first transistor.

With one of the 0.7 cm^2 detectors in the test chamber we had a fwhm of about 10 keV for 976 keV electrons compared with the 12 keV with the detector inside the spectrometer. This showed the advantage of reducing the capacity to the preamplifier, which in the test chamber was only 16 pF from stray capacities, added to the capacity from the detector itself, whereas the stray capacities in the spectrometer were about 30 pF. These stray capacities could be eliminated by mounting the first stage of the preamplifier, i.e. the FET, close to the detectors. Apart from the low capacity to the preamplifier, the FET would be cooled to nearly the same temperature as the detectors, whereby the noise due to the FET would be reduced. To decrease the unwanted capacity at the gate of the FET, also the feedback circuit and the capacity in the test pulse circuit had to be removed to the cooled part of the system. Furthermore the source of the FET was cleaned by a 10 nF capacity to the ground. The set-up of the first stage of the preamplifier in the cooled part is shown in the diagram in fig. 2.2.2 and in the photo in fig. 2.2.3. The connections from this stage to the rest of the system are led separately through 2 mm monel tubes. Nevertheless the signal from the preamplifier oscillated, mainly because of the capacity to ground from the feedback conductor, which gave a phase shift of the signal. This shift could be reasonably compensated by introducing another variable capacity in the preamplifier and at the same time making small changes in some of the components. Nevertheless the signal was not quite cleaned, so the pulse form was as shown in fig. 2.2.4.

This gave a fwhm of about 6 keV at 976 keV; thus the resolution was all right, but the linearity of the preamplifier was completely spoilt because the output stage of the preamplifier could not take the pulse shape made in the charge-sensitive stage; so, after the pulse had been cleaned to the shape shown in fig. 2.2.5 by integrating the pulse after the charge-sensitive stage with about 0.5 μsec, the linearity was regained.

After the reconstruction of the preamplifier the resolution of 976 keV electrons of one of the 0.7 cm^2 detectors was investigated in the instrument as a function of temperature and bias of the detector$^{6)}$. The result is seen in fig. 2.2.6.

The resolution in this set-up is mainly determined by three different effects[4): the drift velocity of the charge carriers, the trapping effect in the detector, and the leakage current; the first of these will, however, mainly act through the second. As seen in fig. 2. 2. 6, the resolution is improved with increasing voltage at a fixed temperature because the drift velocity is increased. At varying temperature the situation is more difficult because the two last-mentioned effects will act on the resolution in different ways. At lower temperatures the trapping effect is increased, which gives a poorer resolution, while the leakage current is decreased, which gives a better resolution. At fixed voltage the resolution vs temperature therefore shows a minimum as seen on the curves. The displacement of the minimum towards lower temperatures at increasing voltage is due to reduction in trapping because of the increased drift velocity.

While the relative courses of the resolution curves are correct, the absolute values might change by ± 0. 4 keV from one run to the other.

To illustrate that the plotted dependence of resolution on temperature is due to the detector and not to the FET, the dependence on the temperature of the latter is shown in fig. 2. 2. 7, in which the detector has been replaced by 10 pF. The figure shows that as compared with the temperature of the total system, that of the FET has a negligible influence on the resolution. Furthermore it appears that cooling of the FET will increase its resolution by about 20% compared with the resolution at room temperature. During the measurement the temperature of the transistor is a little higher than that of the detector. In figs. 2. 2. 6 and 2. 2. 7, for instance, a detector temperature of -60°C corresponds to a transistor temperature of - 53. 5°C, and in the low-temperature region a corresponding set of figures is - 178°C and - 152°C.

The conversion-electron spectrum for ^{207}Bi is shown in fig. 2. 2. 8 for a single detector in the spectrometer and in fig. 2. 2. 9 for parallel-operating detectors. The spectra have been taken at the voltage 1500 V and the temperature - 175°C, and the fwhm is 4. 7 keV at 976 keV with a single detector and 7. 8 keV at the same energy with parallel-operating detectors.

In the case with parallel-operating detectors, which represents the ordinary spectrometer set-up, the resolution has in this way been improved by a factor of nearly 2. 5 compared with that in the set-up discussed earlier in section 2.

2.3. The Remaining Electronics

After the preamplifiers the pulses from the two detectors are summed by means of a simple potentiometer to correct for a possible difference in pulse height from the two detectors. Then the summed pulse is amplified and shaped by means of an "Ortec model 220" linear pulse analysis system. A block diagram of this system is shown in fig. 2.3.1.

The pulses are then analysed in a "TMC" 400-channel analyser. Normally so weak sources are employed that it is not necessary to use any form of coincidence set-up to remove the random coincidences, i.e. coincidences between transitions of different nuclei, and the normal diagram is therefore as shown in fig. 2.3.2.

With a stronger source the random coincidences will be more predominant. Normally, random coincident pulses are not precisely simultaneous, but overlap within a time interval during which the electronics see them as one pulse. To correct for this, a pile-up rejector has been built into the system as shown with a dashed line in fig. 2.3.1. In this rejector the control is made on the time of base-line cross-over, which is later if overlapping occurs.

Fig. 2.3.3 shows the total set-up with cryostat and electronics.

2.4. Magnet Design

The criteria for the magnet are that it has to be used in a 10-cm cryostat, and at the same time the spectrometer should give a 4π-geometry for beta particles or conversion electrons with as high an energy as possible. The length of the winding section was chosen to be 15 cm to give the possibility of a reasonably big distance between the detectors to reduce the solid angle for gamma rays.

The connection between the kinetic energy of the particles and the product $B\rho$ of the magnetic induction and the maximum helical radius of the particles,

$$E = \left\{(m_o c^2)^2 + e^2 c^2 (B\rho)^2\right\}^{1/2} - m_o c^2 ,$$

shows that a high energy demands a high value for $B\rho$. If the bore in the magnet decreases, the product $(B\rho)_{max}$ must decrease owing to ρ because the possible maximum radius must decrease, and the increase in field strength is not enough to compensate for this. $(B\rho)_{max}$ is the maximum possible value for $B\rho$. An increase of the bore makes it possible for ρ to increase, but B will decrease so much that $(B\rho)_{max}$ will again decrease. Therefore it must be possible to find a bore that gives an optimum value for the product and at the same time for the energy at which the spectrometer gives a 4π-geometry. To find this bore one has to know the maximum field that can be obtained with a given type of wire for different inner diameters of the magnet.

Curves of the critical current vs. the magnetic field can be given with about ± 10% for a short sample, which means a superconducting wire of fixed dimentions, in a magnetic field. If the wire makes a coil, the situation is quite different. It appears that the critical current will be greatly reduced, which is named the coil degradation. Experimental experience shows that the premature quenching of the coil at a current below the expected value is initiated by a small length of the wire going normal. The coil current continues to flow, and since the resistivity of the superconductor in the normal state is of the order of 100 times that of copper, the wire temperature at that point rises rapidly. This results in the spread of normality and complete quenching of the coil. Let the wire be coated with a copper layer intimately bonded to the superconductor. Any normal region will then be shunted by a low-resistance path into which the current will be commutated. If the temperature of the composite conductor remains below the critical value while the current is flowing in the copper, the current will return into the superconductor when the transient cause of the latter's going normal has disappeared. If the temperature is higher than critical, the normal region will propagate and the coil will quench. The minimum current at which the propagation can take place is dependent on a number of factors:

(1) the resistance of the composite

(2) the critical temperature

(3) the efficiency of cooling.

D. N. Cornish[7)] has given a range for characteristics of coil performance for a 0.01" dia. Nb 25% Zr wire with copper coating. A mean of these possibilities, shown in fig. 2.4.1, was used to calculate the maximum field that one could obtain with a given inner bore of a solenoid. This field, $H_{oo}(d_i)$, is shown in fig. 2.4.2.

By putting $\rho = (d_i - 0.5)/4$ (ρ and d_i in cm), where d_i is the bore of the magnet and the figure 0.5 takes care of the space used for walls in the system and of the fact that the source is not a point source, we can calculate

$B\rho$, which is shown vs. d_i in fig. 2.4.2. This gives a maximum for d_i = 4.9 cm, and we have chosen d_i = 5.0 cm. Because of the uncertainty in deciding the I-H characteristic this calculation must be seen as a means of making a reasonable decision of the geometry of the magnet and not as an accurate calculation of the optimum geometry.

With the whole geometry of the magnet fixed we can calculate the working line by calculating[8)]

$$\frac{H_{oo}}{I} = \frac{a_1\, f(\alpha,\ \beta)}{A} \quad \text{kgauss/amp} .$$

H_{oo} = axial field at the centre

a_1 = inner diameter of the winding section

$$F(\alpha, \beta) = \text{Fabry factor} = \frac{4\pi}{10}\ \beta \ln \frac{\alpha + \sqrt{\alpha^2 + \beta^2}}{1 + \sqrt{1 + \beta^2}}$$

α = a_2/a_1

a_2 = outer diameter of the winding section

β = b/a_1

b = half the length of the winding section

A = effective cross-section area of the wire (including copper and insulation).

This expression is valid for solenoids with a uniform current density.

In our case we do not need a very homogeneous field. The only criterion that has to be fulfilled is that the field must not dive between the detectors. This is so because there must be no possibility of the particles cycling up and down around the source by mirror effect without arriving at any of the detectors before their direction has been changed by scattering, probably in the source support. We are therefore satisfied with an uncompensated solenoid.

Calculation gives the theoretical value 1.72 kgauss/amp for H_{oo}/I. From the expected curve of fig. 2.4.1 we then have a field strength at the centre of the magnet of about 43 kgauss. The theoretical distribution of the field along the axis is shown in fig. 2.4.3, and in a plane perpendicular to the axis through the centre of the magnet in fig. 2.4.4.

The wire used for the magnet was the following:

Nb 25% Zr	0.010"	(0.254 mm)
copper plating of thickness	0.001"	(0.0254 mm)
nylon insulation of thickness	0.001"	(0.0254 mm) .

The calculated length of the wire needed was 5.515 km, and we ordered 6.0 km, which was delivered in three pieces. Their short sample characteristics given by "Supercon" are shown in fig. 2.4.1. According to these the order of wires from the inner to the outer part of the magnet is 121L, 97L and 100L.

The second factor concerning the minimum propagation current was the critical temperature, which depends only on the superconducting material and therefore cannot be changed. The last factor was the efficiency of cooling, which may be improved by adding thin copper sheets between the winding layers. The copper sheets should be sandwiched between mylar foils to avoid short-circuiting. The ends of the copper interlayers were made to overlap a little, but were electrically separated by mylar sheeting and thus were not shorted turns. Otherwise we might induce heavy currents in the copper foils when passing current into the superconductor. At the same time the copper sheets shielded the layers from each other to prevent energy dissipated in one layer from being transferred electromagnetically into the adjacent layer and thus increasing the current degradation. How much copper sheeting has to be added to a superconducting coil depends mainly on which of the superconducting materials is used. As said above, we used Nb 25% Zr wire, which is quite a stable wire that only demands a copper sheet for every three to five layers. We distributed the copper sheets as follows: one for every three layers over the first 15 layers, one for every four layers over the next 20 layers and one for every five layers over the remainder. The intermediate layers without copper were provided with mylar foils for insulation. The thickness of the copper and the mylar was respectively 0.025 and 0.038 mm. As the superconducting wire was delivered in three pieces, we had to make superconducting joints, which according to "Supercon" can be made by removing the insulation and copper, cleaning the wire surface thoroughly with emery paper and spot welding under carbon tetrachloride. Another way of joining them is used at the department of Professor Særmark at the Technical University of Denmark: the insulation and copper are removed, and the superconducting contact is effected by pressing the superconducting ends together with superconducting filling material in a copper tube. To be sure of a good result we used both these methods at the same time by spot welding the superconducting wires before pressing them together in a copper tube. The copper tube was then soft soldered to the copper plating of the wire. As the current-carrying capacity of the joints is appreciably lower than that of the wire, these joints must be well removed from the maximum field area. Therefore the joints were taken outside the windings and placed in a house at the top of the magnet. The field strength at the joints was then less than 0.3 times that at the centre. The magnetic field degrading the current is the field perpendicular to the wire, and therefore we placed the joints parallel with the axis of the magnet, see fig. 2.4.5.

To make the magnet run persistently we had to short-circuit the ends of the wire with a superconducting switch consisting of a superconducting wire about 3 m long with the copper removed over a length of 1 m. On heating of the switch above the critical temperature this length will go normal and will therefore have a resistance of about 6 ohms, which is enough to force the current into the coil wire. When the wanted magnetic field is reached, the switch heater is switched off and the switch is cooled by the liquid helium, thus short-circuiting the magnet to a closed superconducting circuit.

The current is led to the magnet through 3 mm^2 copper leads with about 2 m in the liquid helium to avoid heat conduction from the room temperature outside the cryostat to the magnet.

After the magnet had been finished, we measured the axial field distribution with a ballistic galvanometer used as a flux meter and found the distribution shown in fig. 2.4.3, where it is compared with the calculated distribution. The working line for the magnet was measured to be 1.92 kgauss/amp as shown in fig. 2.4.1, and the maximum field was measured to be 46 kgauss in good agreement with the measured working line and the expected I-H-characteristic.

The self-induction of the magnet was calculated at 13.05 henries; so the stored energy of the magnet was 3760 joules at 46 kgauss. The stored energy corresponds to an evaporation of about 1.2 l liquid helium.

With the magnet running persistently the average helium consumption is about 0.4 l/h, which makes it possible to operate the system without refilling for about four hours. Normally the cryostat is refilled without the magnetic field being taken off, and therefore the break in accumulating spectra is only very short.

3. MEASUREMENT OF CONVERSION-ELECTRON SPECTRUM

The spectrum we examined during the development of the instrument was that of the conversion electrons from 570 and 1064 keV transitions of ^{207}Bi. The decay scheme for this isotope is seen in fig. 4.1.1. The highest energy of the conversion electrons that can be separated, 1061 keV, belongs to the M-electrons from the 1064 keV transition. This gives a value of $B\rho$ = 4959 gauss cm[9)], where the maximum radius ρ of the helical orbit of the electron occurs when the particle is emitted perpendicularly to the field. To catch such an electron in one of the two detectors, for instance with a detector displacement of 7.5 cm, a source diameter of 1 mm and a sensitive detector diameter of 0.9 cm, we need at least 24.8 kgauss at the detectors, which gives 26.8 kgauss at the centre of the magnet. To find this we used

$$R = r(B_o/B)^{1/2} + 2\rho_B;$$

R = radius of the sensitive part of the detector;

r = radius of the source;

B_o = magnetic field at the centre of the magnet;

B = magnetic field at the place of the detector;

ρ_B = maximum radius of the helical orbit of the electron in the field B.

As mentioned in the introduction, the backscattering effect of the detectors is eliminated when the two detectors are operated in parallel. A particle backscattered from one detector will be caught in the other one because of the magnetic field, giving up the remainder of its energy if not further backscattered.

Now the backscattered particles may have a starting point more distant from the axis than the initial starting point in the source on which we have made calculations above. Therefore the calculated field may not be sufficient. If the field is too weak, the beta particles will go outside the detectors or hit them in insensitive regions. A check on the required field can be made by plotting the total number of counts in the K- and LM-peaks from the 1064 keV decay as a function of maximum magnetic field. This is done in fig. 3.1, from which we find that we are safe with a magnetic field of 30 kgauss in the middle of the magnet.

To get an idea of the backscattering coefficient we made a measurement with the two detectors operated in anticoincidence, and compared it with the case with normal parallel-operating detectors. In the anticoincidence set-up all backscattered particles are omitted, while they are included in the normal set-up. We found a mean backscattering coefficient of about 29% for the conversion electrons from 570 and 1064 keV. This fits very well with the curve of Knop and Paul$^{10)}$.

From fig. 3.1 it is seen that no essential increase in the field strength compared with the calculated 26.8 kG is necessary in spite of the not inconsiderable backscattering. This is so because fast electrons are preferably reflected from the detector at the same angle as the angle of incidence$^{11)}$. In returning, the particles will therefore follow the same field-line tube (nearly cylindrical) as before backscattering.

As an illustration of the effect of the spectrometer, figs. 3.2, 3.3 and 3.4 show the difference between spectra taken under different conditions. To emphasize the effects discussed, the spectra have been drawn in logarithmic scale. Fig. 3.5 gives the same spectrum as fig. 3.4, but in linear scale. Besides the conversion peaks and Compton edges from the gamma rays of 570 and 1064 keV with their sum peaks, one can see in the spectrum fig. 3.4 the K-peaks from 894- and 1430-keV transitions and the K- and LM-peaks from the 1770-keV transition. The Auger electrons are not emphasized in these spectra, but fig. 3.6 shows an example of the splitting-up of the main Auger groups.

Fig. 3.2 is a spectrum taken outside the instrument with a source to detector distance of 0.75 cm. It was taken in the test chamber shown in fig. 2.1.1. It clearly shows tails to the peaks from backscattering and Compton distributions. Fig. 3.3 was taken in the spectrometer with a magnetic field, but with only one detector. The source to detector distance is 3.75 cm. As expected, the Compton distribution is suppressed, but the backscattering is unchanged. Fig. 3.4 shows the spectrum with a magnetic field and with parallel-operating detectors. As said above, the backscattering effect will disappear in this set-up, but still a small tail appears on the low-energy side of the peaks.

Considering the tail to the 1064-keV conversion peaks, one finds it to contain contributions from different effects. First we have a smooth contribution from the bottom of the spectrum up to 858 keV from the ordinary Compton effect. Relative to other effects, this one is so small in this system that the Compton edge cannot be found in the spectrum. Calculations give 32 counts/channel. The Compton contribution from 570-keV transition is more significant, and the calculation of 105 counts/channel fits the experiment all right. Another part of the tail might be due to bremsstrahlung, but the probability of this effect may be neglected at the energies consideres. The last nuclear-physics effect that might explain the tail is the internal Compton effect$^{12)}$. The theoretical contribution from this effect belonging to the two peaks at 976 and 1049 keV is shown by a dashed line in fig. 4.1.2. The distributions were calculated by means of the expression of Spruch and Goertzel$^{13)}$, reduced to the simpler form corresponding to scattered gamma rays of small energy, so the calculations are strictly valid only just under the peaks. The expression of Spruch and Goertzel is based on a Born approximation, which we cannot expect to give very accurate results for heavy elements, but the order of magnitude may be supposed to be correct. In fact later considerations indicate that a larger part of the tail than given by the calculation may be due to the internal Compton (see subsection 5.1).

To see whether the tail should have something to do with the collecting time of the detectors, we used different time constants in the equipment without any significant effect.

From a comparison between the actual tail and the calculated contributions discussed it does not seem that these processes alone can explain the tail. The other part of the tail is due to the detectors. An experimental indication of this may be obtained by taking the counts in the tail in per cent of the total counts in the conversion peak and plotting them as a function of the temperature of the detectors and of the voltage over the detectors. Fig. 3.7 shows that the tail decreases with increasing temperature, but the effect is not very strong. A much stronger effect is seen in fig. 3.8. Here the tail has decreased drastically with a rise in voltage. To ensure that the effects shown in figs. 3.7 and 3.8 are really due to the detector itself, all effects from the transit time in backscattering are reduced by operating the detectors in anticoincidence, so that only the particles that give up all their energy in one detector are accepted. In fact this was not important because the transit time would be negligible compared with the characteristic time, 1-2 μsec, of the electronics. The particles with the lowest rise in helical orbit of course need most time to reach the detector, but with a detector distance of 7 cm, only $1.3 \cdot 10^{-2}$% of the particles with the energy 976 keV need more than 1 μsec.

The two effects connected with temperature and voltage show that part of the trouble presumably comes from trapping in the detectors, and even under well-chosen conditions this cannot be remedied completely in the detectors used. Other effects that might distort the spectrum are self-absorption in the source, absorption in the VYNS film and absorption in the detector window. All these effects are very small at the energies considered and do not account for the presence of the tail because the effect searched for should be able to take away up to half the energy of the particle. Nevertheless the said effects were investigated, but as expected without any result regarding the tail. The self-absorption was investigated by using sources of different strength, and the absorption in the VYNS film was tested by comparing the results obtained with single and double film.

Absorption in the detector window was investigated in two different ways. The first test presupposed that the particles that lose most of their energy in the window must be the particles with the lowest rise in helical orbit because they force the window nearly 90° from normal incidence. If the tail was due to the window, it would be changed by tilting the detector a certain angle. This was done to two different arbitrary angles without any effect. The second test, which was made both alone and combined with the first, took into account that another reason for particles losing much energy in the window is that they are backscattered from the detector. These particles have to force the window three times, twice in the detector from which they are backscattered and once in the other detector, assuming that they are absorbed in the latter. To avoid this, the two detectors were operated in anticoincidence so that only the particles totally absorbed in one detector were accepted. In fact it turned out that the tail was increased by this setup, which indicated that the tail was not due to the detector window. Instead this test might point at the trapping effect in agreement with the abovementioned considerations, for it is reasonable to assume that the trapping effect is more dominant for the holes than for the electrons because of the lower drift mobility. The drift mobility for holes and electrons in silicon is respectively 11,000 cm^2/volt sec and 21,000 cm^2/volt sec at $77^{\circ}K$, and the relative difference will increase at higher temperatures. Therefore pulses from particles that give up all their energy near the negative side of the detector, which is the case with the backscattered particles, will decrease less because of trapping and therefore contribute less to the tail than particles that give up their energy at a greater distance from the negative side of the detector. The assumption of more trapping for holes than for electrons is consistent with the other considerations, but in fact the drift mobility is not sufficient to justify any definite statement about the trapping, which depends on other circumstances as well, see subsection 2.1.

The last effect that might explain the tail was the thickness of the detectors. If the detector is too thin, some particles might pass it without giving up all their energy. To control this, one of the detectors was exchanged for a detector of double thickness (6 mm). It was made at the Health Physics Department, so it could be expected to have the same window thickness as the original one, the only difference being the detector thickness. This change had no visible effect on the spectrum with regard to the tail, so still everything points at the trapping effect as the cause of the instrumental part of the tail.

While working at the spectrometer, we learnt that Shera et al. had had success with an instrument of the same type14). In fact we could not agree with Shera et al. about their explanation of the tail on the low-energy side of the conversion peaks. They explained their tail by an internal Compton effect, but our tail is considerably smaller than theirs, so this explanation must be wrong (compare their fig. 7 with our fig. 3.5). The approximately calculated contribution of the internal Compton process was not even able to explain our tail as shown above. Furthermore we have shown that the latter is still dependent on the working conditions for the detectors and therefore not just a nuclear-physics effect. At the time of publishing our work3) we had a resolution a factor of 2 better than that in the spectrum of Shera et al. The resolution of the spectra in this section is further improved by more than a factor of 2 because of the reconstruction of the preamplifiers.

4. CONVERSION COEFFICIENTS

Whenever a nucleus is formed in an excited state, the excitation energy will be given off by radiative and non-radiative processes. The radiative de-excitation consists of quantum emission of gamma rays. The non-radiative de-excitation processes consist of internal conversion-electron emission, internal Compton effect, internal pair formation or monoenergetic positron emission, and, to a much smaller extent, multiple electron emission. Most transitions of interest have an energy less than 1 MeV, at which the internal conversion process and the single gamma-ray emission are the most common of the non-radiative and the radiative processes respectively. However, transitions between two 0^+ states proceed only through non-radiative processes.

The internal conversion coefficient is defined as the number of electrons divided by the number of gamma rays emitted per unit time, $\alpha = N_e/N_\gamma$, where N_e and N_γ are the decay rates. It was formerly assumed that the conversion electrons were due to absorption of gamma rays, and the same definition of the conversion coefficient was used, giving $\alpha' = N_e/(N_\gamma + N_e) = \alpha/(1 + \alpha)$.

However, it was early suggested[15)] that there was no reason for this assumption and that it was more correct to say that an atom had two modes of getting rid of its excess energy: gamma-ray emission and electron ejection, but it was many years before this concept, which was later supported by calculations of Hebb and Uhlenbeck[16)], gained full recognition as the proper description of the process.

As the energy- and Z-dependence of the conversion coefficient varies with different types of transition, the internal conversion coefficient is important as a tool for determining the multipolarity of transitions in nuclei.

The internal conversion coefficient can be determined in several different ways. Subba Rao[17)] has given a review of the methods employed up to 1966 and a few new ones. Another method, based on $e^- - e^-$ or $\beta - e^-$ coincidence, which is especially suitable for our instrument, is given below with examples of decays to which it has been applied.

The first type of decay is that shown in fig. 4.1 with two gamma decays in cascade following electron capture.

The only things necessary are: (1) that the gamma decays have to be in coincidence compared with the characteristic time of the electronics, which is 1-2 μsec, and (2) that both the decays have a reasonably large conversion ratio.

The idea of this method is the following: With the set-up used with parallel-operating detectors, these will in fact act as a single detector with 4π-geometry. When one of the transitions, say 1, takes place through internal conversion, the output pulse from the detector will depend on whether the other one will take place through gamma decay or internal conversion. In the former case the output pulse will correspond to the energy of the electron from transition 1, which gives one peak in a multichannel analyser, and in the latter case the pulse will correspond to the sum of the electron energies, which gives another peak in the multichannel analyser. By comparison of these peaks the total conversion coefficient for transition 2 can be obtained, and similarly for transition 1.

If all the corrections for the resolution of the system, unwanted coincidences and irrelevant processes that have been mentioned in the example of the decay of this type are ignored, the counting rates can be set up in the equations

$$N_1 = N \frac{\alpha_1}{1+\alpha_1} \omega_1 \varepsilon_1 \left(1 - \frac{\alpha_2}{1+\alpha_2} \omega_2 \varepsilon_2 \right)$$

$$N_2 = N \frac{\alpha_2}{1+\alpha_2} \omega_2 \varepsilon_2 \left(1 - \frac{\alpha_1}{1+\alpha_1} \omega_1 \varepsilon_1 \right) \qquad (4.1)$$

$$N_s = N \frac{\alpha_1}{1+\alpha_1} \; \frac{\alpha_2}{1+\alpha_2} \omega_1 \omega_2 \varepsilon_1 \; \varepsilon_2 \; .$$

N_1 is the counts per unit time in the peak corresponding to transition 1;

N_2 is the counts per unit time in the peak corresponding to transition 2;

N_s is the counts per unit time in the sum peaks;

N is the decay rate;

ω is the solid angle from the source to the detectors, which is 1 in the 4π-geometry;

ε is the intrinsic detector efficiency for electrons, which is 1 for semiconductor detectors;

α is the conversion coefficient defined as $\alpha = N_e/N_\gamma$.

The term $\alpha/(1 + \alpha)$ gives the probability of internal conversion relative to the total decay rate, and the term $(1 - \alpha/(1 + \alpha))$ gives the probability of transition through gamma decay.

From equations (4.1) we find

$$\alpha_1 = \frac{N_s}{N_2} ; \qquad \alpha_2 = \frac{N_s}{N_1} ; \qquad N = \frac{(N_1 + N_s)(N_2 + N_s)}{N_s} \; . \qquad (4.2)$$

In this case it is thus possible to measure the conversion ratios and the absolute source strength. The latter can in this set-up be determinated without utilization of the 100% efficiency of the spectrometer, which is necessary in determining the conversion coefficients. As an example of this type of decay, ^{207}Bi has been used.

The second type of decay that is especially suitable for the instrument is that shown in fig. 4.2.

In the case where a beta particle is in coincidence with a conversion electron it will contribute to a distribution of the same shape as the beta distribution, but reduced by a factor equal to the conversion coefficient and displaced by an energy equal to that of the conversion electron. The total conversion coefficient can then be obtained by comparing the count rates in these distributions. Considering the separation of these, it will therefore be convenient if the energy of the conversion electron is greater than the maximum energy of the beta particles.

Under the same assumptions as above we have

$$N_e = N \frac{\alpha}{1+\alpha} \omega_e \varepsilon_e \qquad N_\beta = N \left(1 - \frac{\alpha}{1+\alpha} \omega_e \varepsilon_e\right) \omega_\beta \, \varepsilon_\beta . \tag{4.3}$$

N_e and N_β are the counts per unit time in the conversion and the beta distribution respectively. N, α, ω, and ε have the same meanings as above. From eq. (4.3) we then have

$$\alpha = \frac{N_e}{N_\beta} . \tag{4.4}$$

^{198}Au and ^{203}Hg have been used to illustrate this type of decay.

4.1. Measurement of Conversion Ratios for ^{207}Bi

The generally accepted decay scheme for ^{207}Bi is seen in fig. 4.1.1.

The e^- - e^- coincidence has been taken between the most intensive of the conversions, the 570-keV and 1064-keV decays, which are marked in the figure.

When these decays are studied in the spectrometer, the prominent features of the spectrum are K, L, M ... lines of the two said transitions and a series of sum lines corresponding to the case where both transitions happen to go via internal conversion. Besides the conversion peaks and Compton edges from the gamma rays of 570 and 1064 keV with their sum peaks one can see in the spectrum fig. 4.1.2 the K-peaks from 894-keV and 1430-keV decays and the K- and LM ...-peaks from the 1770-keV decay.

The spectrum shown in this section was accumulated before the last improvement in resolution by reconstruction of the preamplifiers and is therefore not equal to the spectra in section 3 with regard to resolution.

To calculate the conversion coefficients for the two said transitions it is necessary first to correct the spectrum so that the peaks to be used are as free as possible from distortion from other effects. First the background count has to be subtracted. Then the contributions from the Compton process must be calculated and subtracted. The probability of Compton scattering is the product of the intrinsic gamma interaction probability of the counters and the solid angle between the source and the detectors. The calculation of the intrinsic probability is based on the energy-dependent Compton cross section, which has been taken from tables of Davisson18). As mentioned in section 3, the calculated contributions from Compton interaction for the decays 570 and 1064 keV are 32 and 105 counts/channel respectively. The only interaction from the other gamma rays that is not negligible is the Compton interaction from the 1770-keV decay, which was calculated at 1 count/channel. This was taken into account in finding the content of the sum peaks. The two peak sets then have to be corrected for the internal Compton distribution. The relative contributions were calculated by means of the formula given by Spruch and Goertzel13), reduced in the way discussed in section 3. This expression was integrated over all angles, thus giving the total Compton coefficient, i. e. the number of internal Compton-scattered gamma rays divided by the number of conversion electrons, as12)

$$B_K = \frac{\alpha}{\pi} \left\{ \frac{1}{\beta} \ln \frac{1+\beta}{1-\beta} - 2 \right\} \frac{dq}{q} \ ,$$

which is valid for all magnetic multipoles. α is the fine-structure constant, $e^2/\hbar c = 1/137$, β is the ratio of the velocity of the scattered electron to the velocity of light, and q is the energy of the scattered gamma ray. The expression will be directly valid in the case of the 1064-keV decay, which is an M4 transition, but Iakobson19) found it valid for electric multipoles as well as long as the nuclear transition energy is small compared with the electron rest mass. In the case of the 570-keV decay, which is an E2 transition, the energy is of the same order of magnitude as the said energy, but the expression for B_K will be used as an approximation. The index K in the internal Compton coefficient indicates that it has been calculated for K-shells only, but Spruch and Goertzel show that the B-coefficients are fairly insensitive to the shell where the emission occurs, so it has been used for both K-, L- and M-shells. The last uncertainty is that the expression of Spruch and Goertzel is based on a Born approximation, which demands $2\pi Ze^2/\hbar v \ll 1$ (v is the velocity of the electron), so we cannot expect it to give very accurate results for heavy elements, but the order of magnitude may be expected to be correct. In fact the contributions from the internal Compton process do not need to be known very accurately because they amount to less than 2% of the content of the peaks.

When the internal Compton coefficient vs. the energy of the scattered electrons has been calculated for each conversion peak, the absolute contribution from this effect can easily be found from the total amount of counts in the peaks with belonging tails. On the low-energy side the tails were extrapolated exponentially.

In the case of the sum peaks all problems connected with the tail from the internal Compton effect were overcome in the following way: First the two sets of peaks from the 570-keV and 1064-keV decays, including the contributions from Compton and internal Compton processes, were folded, which gave a result in good agreement with the experimentally found distribution of the sum peaks. Then the two first-mentioned sets of peaks were corrected for irrelevant contributions in the way described above and then folded, which gave the right distribution of the sum peaks. This distribution was used to find the right cut-off of the peaks on the low-energy side.

Because of the very weak source, 0.04 µC, the ratio of random to real sum pulses was kept below 0.6%. In the calculation of the conversion coefficient the random sum pulses, the coincidences between conversion electrons from one decay and Compton electrons from the other and the correction of the sum peaks from gamma interaction and tail from the 1770-keV decay were taken into account. Coincidences between conversion electrons and Auger electrons will be insignificant in the determination of the total conversion coefficients because the resultant pulses are still in the same set of conversion peaks.

Because of the design of the system, with no scattering from the walls, no backscattering effect, thin windows of the semiconductor detectors, and the carrier-free source, no other corrections had to be made with the energies investigated. At very small energies, absorption in the windows cannot be neglected (see subsection 4.2).

The essential contributions to the uncertainties of the counts in the peaks are the extrapolated contributions from the tails, the calculation of the internal Compton effect, and the statistical uncertainty. The extrapolations of the tails were taken as uncertain with their full amounts, and the calculation of the internal Compton effect was taken as uncertain with 50% because of the approximations mentioned above. The final amounts in the peaks obtained by a 100-minute measurement to calculate the conversion coefficients are

$$N_{570} = 178025 \pm 2.0\%$$

$$N_{1064} = 830328 \pm 0.9\%$$

$$N_{sum} = 18555 \pm 1.2\% .$$

The reason for the greater uncertainty of the amount of the 570-keV peaks compared with the 1064-keV peaks is that the former contains contributions from extrapolated tails from both sets of peaks.

Unlike what is the case in the simple decay scheme in fig. 4.1, it is necessary in the case of ^{207}Bi to correct for the branching ratio to the 1634-keV level because only 87% of the decays go through this transition 20). In the case of 570 keV it is reasonable to say that this is a 100% transition because the decay through 1430 keV - 894 keV is negligible (0.16% of the total decay). For this purpose the decay scheme for ^{207}Bi should be replaced by the decay scheme in fig. 4.1.3, and the formulas (4.1) and (4.2) should be replaced by

$$\begin{aligned} N_{570} &= N \frac{\alpha_{570}}{1+\alpha_{570}} \left(1 - \frac{\alpha_{1064}}{1+\alpha_{1064}} \cdot r\right) ; \\ N_{1064} &= N \frac{\alpha_{1064}}{1+\alpha_{1064}} \cdot r \cdot \left(1 - \frac{\alpha_{570}}{1+\alpha_{570}}\right) ; \\ N_s &= N \frac{\alpha_{570}}{1+\alpha_{570}} \frac{\alpha_{1064}}{1+\alpha_{1064}} \cdot r ; \end{aligned} \qquad (4.1.1)$$

$$\begin{aligned} \alpha_{570} &= \frac{N_s}{N_{1064}} ; \qquad \alpha_{1064} = \frac{N_s}{N_{570}} \left(r - \frac{N_s}{N_{570}} (1-r)\right)^{-1} \\ N &= \frac{(N_{570} + N_s)(N_{1064} + N_s)}{N_s} \end{aligned} \qquad (4.1.2)$$

where r is the branching ratio, r = 87%.

In the case of the 570-keV decay, where the result is not influenced by an adopted value such as the branching ratio in the 1064-keV decay, the high-energy peak has been split up into the L- and M ...-peaks to obtain K/L and K/M ... ratios, see fig. 4.1.4.

The α_K coefficients can then be calculated from

$$\alpha_{K570} = \frac{\alpha_{570}}{1 + \frac{1}{K/L} + \frac{1}{K/M\ldots}} ; \qquad \alpha_{K1064} = \frac{\alpha_{1064}}{1 + \frac{1}{K/LM\ldots}} .$$

The results are given in table 1 21)* and compared with theoretical calculations and some of the recent experimental values.

---

[*] In ref. 21 the definition $\alpha = N_e/N_t$, $(N_t = N_e + N_\gamma)$ has been used.

Table 1

		Experimental	Theoretical a)	Other experiments
570 keV	α	0.0224 ± 1.5%	0.0217	
	K/L	3.45 ± 10%	3.53	3.17 b) 3.3 ± 6.1% c)
	K/M ...	9.07 ± 20%	13.61	
	α_K	0.0160 ± 3.0%	0.0160	0.0156 d) 0.0159 ± 3.8% e)
1064 keV	$r \cdot \alpha$	0.1059 ± 2.1%		
	r	0.87 adopted		
	α	0.1217 (± 10%)		
	K/LM ...	3.37 ± 10%		
	α_K	0.094 (± 10%)	0.098	0.090 d)

a) Ref. 22 b) Ref. 23 c) Ref. 24 d) Ref. 25 e) Ref. 26 .

As mentioned earlier in this section, coincidences between conversion electrons and Auger electrons will be insignificant in the determination of the total conversion coefficient. This does not apply to the determination of the conversion coefficients for the different shells because the K/L- and K/M ... -ratios will be influenced by these coincidences. First there is a possibility of Auger electrons because of the electron capture in ^{207}Bi. These are not coincident with the conversion electrons because of the lifetime of the 1634-keV level of 0.8 sec. Auger electrons following conversion electrons are in coincidence with the latter, and the resulting pulse is increased according to the energy of the Auger electron, for example 57 keV for a KL_1L_2 Auger electron. To correct for this we have to know both the Auger yield and the relative intensities of the Auger groups in order to ascertain the effect of the coincidences on the higher-energy peaks. The

Auger yield has been given for K- and L-shells, and the relative intensities for K-Auger groups have been investigated experimentally[27)], but the Auger yield for M shells as well as the relative intensities for L-Auger groups have not been determined either theoretically or experimentally. Consequently it was not possible to make a reasonable correction for this effect. Furthermore a correction of the K/L and K/M ... ratios should take into account the fact that electrons might be ejected by other processes than Auger transitions, for instance a "shake-off" mechanism because of the change in electric field created by the sudden loss of an electron in one of the inner shells by the conversion process[28)]. However, most of these electrons have very little energy, which gives a great possibility of absorption in the detector window.

The K/L- and K/M ... -ratios were therefore taken directly from the peak-values, but given with a correspondingly large uncertainty. In the case of the 1064-keV decay the K/LM ... -ratio was also determined from the peak values, which is not quite correct because the L- and M-peaks do not merge completely.

In spite of the said uncertainties the uncertainty of α_{K570} is rather small, and for both decays the determination of the α_K's is in reasonable agreement with theoretical calculations of Hager and Seltzer[22)] and with earlier experiments. The uncertainty of α_{K1064}, mainly due to the adopted value for r, which is not too accurate, says nothing about the accuracy of the instrument and has therefore only been very roughly estimated.

The forte of the instrument is the possibility of measuring the total conversion coefficient. In the 570-keV decay this coefficient was therefore compared with the theoretical value based on the calculations of Hager and Seltzer. As seen in table 1, the agreement is not as good as for α_K, which might indicate that the calculations for the higher shells, especially the M shells, are not good enough.

4.2. Measurement of the Conversion Ratio for ^{203}Hg

The generally accepted decay scheme for ^{203}Hg is seen in fig. 4.2.1.

Besides this there is perhaps a beta transition directly to the ground state with E_{max} = 491 keV, but this intensity is so weak ($<$ 0.004%) that it will be ignored. The lifetime of 0.28 nsec at the 279-keV level is negligible compared with the characteristic time of 2 μsec in the electronics, so the decays will be seen as in coincidence.

As explained in section 4, the expected spectrum would be a beta distribution with superimposed similar distributions coming from the cases where the 279-keV decay takes place via internal conversion. The superimposed distributions decrease with the respective conversion ratios compared with the original beta distribution, and they are displaced by the energy of the conversion electrons K, L, M ... .

According to the remarks earlier in section 4, this decay should be very suitable for measurement of the conversion coefficient. It has a rather high coefficient, and the energy of the K-conversion electron is only a little less than the maximum energy of the beta spectrum. Nevertheless, considering the simplicity of this measurement, a closer examination will be disappointing.

In fact it appears that, as seen in fig. 4. 2. 2, the spectrum does not look like the expected spectrum; peaks from conversion electrons are superimposed though these always have to be in coincidence with beta particles according to what is said above. In the case with less than 100% efficiency, which is demonstrated in fig. 4. 2. 3 by using only one detector, it is quite clear that conversion peaks will appear because a conversion electron can be detected from a decay where the beta particle will not be detected. With both detectors operating in parallel, which gives 100% efficiency, this should not happen, but still there is a little left in the peaks.

Careful investigations of this phenomenon have shown that the dominating causes for these peaks are the VYNS-film which supports the source, and the thickness of the detector windows, while another obvious cause like self-absorption in the source is not essential with the sources used.

The peaks are produced in the following way: The beta particles with the lowest energies are absorbed in the VYNS-film or in the window of one of the detectors. In these cases the output pulse from the detector, which should be a superposition of the pulses from the beta particle and the conversion electron, when this electron occurs, will only come from the latter and will therefore give a contribution to the conversion peak. In this way the pulses in the peak have been taken from the belonging distribution. This is clearly seen in fig. 4. 2. 4, which shows the spectrum taken with two different sets of detectors with different window thicknesses. The full-drawn spectrum was taken with the detector set made at the Health Physics Department of Risö, which has rather thick windows. The dashed spectrum was taken with the 3-mm commercial detector set, whose window thickness is given as 50 micrograms/cm^2. Integration over the interesting parts of the two spectra gives the same total amount. Apart from the fact that beta pulses lacking in the real beta distribution appear in the conversion distribution as a conversion peak the effect discussed will at the same time distort the spectrum because beta particles that have forced the VYNS-film and the detector window may have lost a good deal of their energy.

It was tried to reduce the window effect by changing the angle of incidence at the detectors. If the detectors were placed in a homogeneous magnetic field, the angle of incidence would be the same as the angle at which the particle leaves the source. In that case the fraction of particles with a glancing angle less than θ would be $\sin\theta$. When the detectors are placed symmetrically in an inhomogeneous magnetic field, which is the case here, the angle of incidence is less than 47° with the set-up used. By an axial displacement of the system in the magnet the angles of incidence are changed both because of a new ratio between the field strength at the source and that at the detectors and because of magnetic-mirror effect, which at the same time unfortunately forces some of the particles a few more times through the source support. A displacement of this kind was tried, but the result was deterioration of the spectrum.

Before the spectrum was used for calculations, it was corrected for background counting. No other corrections have been made because the calculated contribution from Compton interaction is so small that it does not influence the spectrum, and the beta transition directly to the ground level is so weak that it will be ignored as said above. Furthermore random coincidences can be ignored with the source strength used.

In the calculation of the conversion coefficients for the 279-keV decay the total spectrum should be split up into a real beta distribution and the superimposed similar distributions from the conversion electrons in the way explained previously. Fig. 4. 2. 2 shows such a split-up of the total spectrum. The open circles indicate the sum of the individual distributions. Now the formula (4. 5) can be used for each conversion ratio K, L and M ..., but normally the K-coefficient and the ratios K/L and L/M ... are given. We have α_K as the ratio between the areas under the K-distribution and the real beta distribution and the K/L-ratio as the ratio between the areas under the K-distribution and the L-distribution, and similarly for L/M ... .

The results are shown in table 2 and compared with the generally accepted values[29)]. They cannot be compared directly with theoretical calculations for pure transitions because the transition discussed is a mixture of M1 and E2.

Table 2

^{203}Hg	Experimental	Mean of other experiments
α_K	0.127	0.163
K/L	3.28 ± 4%	3.33
L/M ...	3.26 ± 8%	3.23

It is seen that the K/L- and the L/M ... ratio are in good agreement with other experiments, while the conversion coefficient α_K is rather low. In other words, the amount in the beta distribution is too large compared with the amounts in the conversion distributions. One reason for this might be that another beta distribution is superimposed on the spectrum, but an investigation of the gamma spectrum from the source used does not show any impurities, and no change is noticed in the shape of the spectrum with time, so a potential impurity must be beta emitting only, with nearly the same half-life as ^{203}Hg and with nearly the same energies because higher energies would influence the K/L and L/M ... ratios.

A more reasonable explanation is a combination of two other effects: (1) non-linear energy response at low energies, (2) instrumental distortion of the spectrum giving the previously discussed tail to the peaks. The lowest energy used for investigation of the linear energy response is 58 keV from KLL Auger electrons from ^{207}Bi. Below this energy the response is not well known. An unlinear response would cause the horizontal displacement between the real beta- and the K-conversion distribution to be different from the one used in the calculation, where linear response was assumed. If for instance the beta distribution is displaced by 5% of the maximum energy, the α_K coefficient will be changed by about 20%.

With regard to the distortion of the spectrum it is known from section 3 that, besides a peak, monoenergetic electrons will give a tail on the low-energy side of this peak. As mentioned in the said section, the spectrum was taken with the detector set made at Risö, and the tail was believed to be mainly a combination of internal Compton in the source and trapping in the detectors. On comparison of the same spectrum taken with the detector set made at Risö (dashed curve) and the 3-mm commercial detector set (full-drawn curve) it is seen from fig. 4.2.5 that the commercial set gives a significantly larger tail than the other. It is therefore quite clear that the dominating cause of the tail from this detector set is not a nuclear physics effect, but an instrumental effect that must be expected to appear for beta particles as well as for conversion electrons. Therefore this distorting effect will influence the beta distribution once, but the conversion distributions twice, because these come from summing of a beta particle and a conversion electron. Hence, as long as the tail is not so well known that it may be unfolded from the spectrum, it will in principle not be reasonable to compare the beta distribution with a conversion distribution. It was tried to find the energy dependence of the tail by comparing the conversion peaks of 976 keV and 482 keV from ^{207}Bi and of 365 keV from ^{113}Sn, but for the low-energy peaks the tail is in fact overlapped by other contributions such as those from Compton electrons and Auger electrons. The comparison gave the impression that the tail was relatively increased at lower energies, but to clear up the tail problem properly more careful investigations with a coincidence set-up will be necessary.

As to the nuclear-physics contributions to the tail such as internal bremsstrahlung for the beta spectrum and internal Compton for the conversion spectrum, the distributions from which are very similar$^{12)}$, we may again talk of an effect influencing the beta distribution once and the conversion distribution twice.

The effect of the non-linear response at low energies is seen to be very great, and it is believed, in agreement with the result of measurement of the total conversion coefficient for the 412-keV transition in ^{198}Au, that this is the dominating of the effects (1) and (2) discussed above. However, also distortion because of the window effect is important at the low energies in the spectrum of ^{203}Hg.

In the case of comparison between two conversion distributions we have: (1) known linear response in the energy region considered and (2) similar distortions of the distributions; so they can be compared, giving the K/L- and L/M ... ratios if only the tail is assumed not to change significantly in the energy interval corresponding to the displacement of the conversion distributions. Therefore these ratios have been given with an estimated uncertainty in the table, while the conversion coefficient has been given as a figure only.

4.3. Measurement of the Conversion Ratio for the 412-keV Decay in ^{198}Au

The generally accepted decay scheme for ^{198}Au is seen in fig. 4.3.1.

If the most intensive transitions marked in the figure are considered, it is seen that the decay type is the same as that of ^{203}Hg. The differences between the two decays are the maximum energy of the beta distribution and the ratio between this energy and that of the conversion electrons. Again the lifetime of the level connecting the beta- and the gamma transition is negligible compared with instrumental times, so the two transitions may be considered to be in coincidence.

Because of the higher maximum energy in ^{198}Au the relative contribution to the conversion peaks, which was an important problem for ^{203}Hg, is much smaller. On the other hand it is more difficult to separate the real beta distribution from the conversion distributions because they are overlapping to a very great extent. The uncertainty in separating the K- from the L- and M ... -conversion electrons, as in the case of ^{203}Hg, is significant, so it was not tried. Instead the K, L, M ... distributions were taken as one distribution used for the calculation of the total conversion coefficient α. The relative displacement between K and L compared with the maximum energy of 962 keV is about 7%. The horizontal displacement of the total conversion distribution is taken so as to correspond to the energy of the K-conversion electrons.

The problem is to fit two distributions, a beta distribution and a combined KLM ... conversion-electron distribution which satisfy the following conditions: first their sum has to give the measured total spectrum when they are displaced by the right energy, and secondly they must have the same shape. The result of this fitting is seen in fig. 4. 3. 2.

Before the spectrum was split into different contributions, it was corrected for background counting. No other corrections have been made because of the following: the two other beta decays have not been taken into account because the one with a high maximum energy is negligible compared with the 962-keV decay as well as the conversion distribution coincident with this decay, and the one with a low maximum energy can be neglected because it is not necessary to consider energies below 287 keV. At the same time it is so weak that coincidences between itself and conversion electrons from the 675-keV or 1087-keV decays can be neglected. The total conversion coefficient for the 675-keV decay is of the same size as, and that for the 1087-keV decay much less than, that of the 412-keV decay. In the same way the Compton contribution from the 675-keV and 1087-keV decays can be neglected. The Compton electrons from the 412-keV transition are in coincidence with the beta particles from the 962-keV decay. They are therefore spread out in more than 350 channels instead of the 65 channels corresponding to their maximum energy. So the average contribution per channel, which is calculated at about 11, will be too small to influence the spectrum significantly. Random coincidences can be neglected with the source strength used.

It will be recalled that in the case of ^{207}Bi all that kind of correction was taken into consideration. This was because the line spectrum gave the possibility of a very accurate measurement. In the case of beta spectra it does not seem reasonable to make corrections of an order less than 1% because for other reasons the result is uncertain by 5% or even more.

In principle the remarks said in subsection 4.2 about comparison of beta- and conversion distributions are valid, but again the lacking knowledge of the energy dependence of the tail means that it cannot be said in advance how great the influence will be in this case. At any rate the distortion because of the detector window is limited to a much smaller part of the spectrum because of the higher maximum energy of the beta particles as well as the higher energy of the conversion electrons. According to the impression mentioned in section 4.2 the tail should be relatively decreased at higher energies, so this effect is not expected to be important.

In fact it appears that the fitted distributions are in very good agreement in the energy interval 300-700 keV. Below 300 keV they cannot be compared for different reasons. First the real beta spectrum has another beta spectrum below 287 keV superimposed as discussed above. Secondly the KLM ... distribution is distorted in this region because of the displacement, especially between K and L, and because of the conversion peak formation. Above the said energy region the KLM ... distribution is again influenced by the mutual displacement of the individual distributions, which will give a distortion tending to increase the intensity compared with that of the real beta spectrum.

The calculation of α is made by means of the distributions in the interval 300-700 keV. As mentioned earlier in section 4, $\alpha = N_e/N_\beta$, and the best value has been found by a least squares fit of KLM/α - for different α's. The main cause of the uncertainty in deciding the conversion coefficient for ^{203}Hg was the non-linear energy response. This is not important to the same extent in the case of ^{198}Au because the slope of the beta spectrum is much smaller than for ^{203}Hg, so a horizontal displacement of the beta distribution will only result in a small change in the conversion coefficient.

Table 3

^{198}Au	Experimental	Theoretical	Other experiments
412 keV	0.046 (± 5%)	0.0450[a)] 0.0440[b)]	0.045[c)] 0.048[d)] 0.044[e)]

a) Ref. 30 b) Ref. 22 c) Ref. 31 d) Ref. 32 e) Ref. 33

The final result is given in table 3 and compared with other experiments as well as theoretical values. In the latter case the total α is taken as the sum $\alpha = \alpha_K + \alpha_L + \alpha_M$. The uncertainty, written in brackets, is given with reservation for the distortions discussed, which do not seem to be important for the conversion coefficient at higher energies.

5. BETA SHAPE

The purpose of measuring the beta-ray distribution is to determine the end-point energies and the relative abundance of the several beta-ray groups that may occur. The beta-ray spectrum is analysed by comparing the measurement with the result to be expected from the theory of beta decay. Since the spectrum from a substance emitting a single group of beta rays extends from the maximum energy E_o to low energies with a certain theoretical shape, and since, in many disintegration schemes, several beta-ray groups are emitted, it is clear that a determination of these groups will depend on a shape analysis.

The theoretical expression for this shape is given by[34)]

$$N(W)\,dW = \text{const.}\; F(Z,\; W)\; p\; W(W_o - W)^2\; dW\; S_n(W)\;, \tag{5.1}$$

which gives the number of beta rays in the energy range dW at the energy W, which is the total energy in m_oc^2 units. p is the momentum in m_oc units. $pW(W_o - W)^2\, dW$ represents the so-called statistical shape, F(Z, W) denotes the Coulomb factor and $S_n(W)$ the shape factor for forbidden spectra. For allowed spectra, $S_n(W) = 1$. Apart from the superallowed transitions, which include mirror nuclei, e.g. the neutron decay, the table below gives the selection rules for the vast majority of beta decays[35)].

	Change of parity	Spin change
Allowed	no	0 ± 1
1st forbidden	yes	$0 \pm 1 \pm 2$
2nd forbidden	no	$\pm 2 \pm 3$

The shapes considered here are from the beta decay of ^{203}Hg, ^{32}P and ^{198}Au (the 962-keV transition). Of these only that of ^{32}P is an allowed decay with no change of parity and a spin change of - 1. Both ^{198}Au and ^{203}Hg are 1st forbidden with a change of parity and spin changes 0 and - 1 respectively. In fact most of the 1st forbidden spectra should show an allowed shape, particularly beta transitions from elements of high atomic numbers[36]. Therefore $S_n(W)$ has been set equal to 1 for ^{198}Au and ^{203}Hg as well.

However, in the last ten years it has been discussed whether even allowed shapes should be corrected to be in agreement with the theoretical form. At the present time it is often difficult to decide whether this correction factor, $c(W) = 1 + aW + b/W + cW^2$, is of theoretical significance or of instrumental origin. In the case of ^{32}P numerous experimenters have given different values of the constants in c(W). Some of the recent experiments have returned to $c(W) = 1$[37, 38].

The factor F(Z, W) has been taken from the table of Dzhelepov and Zyryanova[39], which includes corrections for the finite size of the nucleus as well as for screening by the atomic electrons.

If eq. (5.1) is rearranged and $S_n(W)$ set equal to 1, the equation becomes

$$(N(W)/F(Z,\ W)pW)^{1/2} = \text{const.}' \cdot (W_o - W)\ . \qquad (5.2)$$

It is then clear that if the function on the left-hand side of eq. (5.2) is plotted against W, a straight line will result. The interception of this line with the W-axis will be W_o, the total disintegration energy in $m_o c^2$ units.

When a shape analysis is used for the investigation of the spectra, it is very important to prevent distortion of the spectra. The most serious distortions take place at the low-energy end of the spectrum and are caused by the source thickness, the source backing and the thickness of the detector window. Some distortion may result from the resolution of the instrument and may be of influence at all energies.

As mentioned earlier, we use carrier-free sources on a source backing of 35 µg/cm^2 VYNS-film. The detector window is about 50 µg/cm^2 thick and thus stops beta particles with energies less than 5 keV at normal incidence. The transmission of the window rises gradually as the energy of the electron is increased until 100% transmission is reached. A good working rule is that the window thickness will not influence the shape of the spectrum above an energy that is four times the cut-off energy. The circumstances that make the problem of source backing and window thickness rather serious in our instrument are first that, because of the helical orbit of the electron in the magnetic field, the angle of incidence is very often large so as to give a longer path in the insensitive regions, resulting in higher cut-off energies, and secondly that the great backscattering from the solid-state detectors will force many of the particles to penetrate the detector windows as well as the VYNS-film more than once.

5.1. Investigation of FK-Plots for ^{203}Hg, ^{198}Au and ^{32}P

The beta spectra of ^{203}Hg, ^{198}Au and ^{32}P are seen in figs. 4.2.2, 4.3.2 and 5.1.1 respectively. ^{203}Hg has been plotted logarithmically because of a very steep rise in the spectrum at decreasing energies. The two other spectra have been plotted linearly. In the case of ^{198}Au the beta spectrum can only be decided for energies above 250 keV because of the transients of the total conversion distribution. The shape of the real beta spectrum below this energy has therefore been taken from a linear FK-plot. Only for ^{32}P was the pure beta spectrum measured directly, while the two others were measured with conversion distributions superimposed. In the latter cases the beta distribution was extended in the way discussed above. The FK-plots for the three beta decays are seen in figs. 5.1.2, 5.1.3 and 5.1.4 respectively.

Starting with ^{203}Hg, which has the lowest maximum energy, it is seen that with some deviations the FK-plot is linear for energies above 75 keV. Below this energy the distortion because of the window effect will influence the spectrum and spoil the linearity. According to other experiments the spectrum would be expected to be linear in any case for energies above 20 keV[40, 41, 42]. In the case of ^{198}Au the linearity is considerably better for energies above 287 keV, below which the spectrum has another beta spectrum from the same isotope superimposed. It is seen that the window effect will have no influence at energies above the said 287 keV. In the case of ^{32}P the FK-plot is linear for energies above 248 keV. Under this energy it has another beta spectrum for ^{33}P superimposed.

In finding linear FK-plots we are in agreement with Shera et al.[14)], but in fact we know that the spectra are influenced by some instrumental distortion as discussed in subsection 4. 2; therefore linear plots should in principle not be expected. That linear FK-plots are nevertheless observed might indicate that the approximated calculation of the internal Compton effect, discussed in subsection 4. 1, gives a too small result, so this effect is a more dominating cause of the distorting tail than previously expected.

Common to all three FK-plots is that the extrapolation of the straight line will give an energy too small compared with the normally accepted average value from numerous other experiments[29)]. This indicates that except for the highest energies, which do not satisfy the straight line, the instrumental distortion should be so special that the linearity of the FK-plots is preserved, but the whole line is displaced towards lower energies.

The deviation from linearity for the highest energies is greater than may be explained by resolution distortion from a Gaussian distribution with a width corresponding to that of the conversion electron peaks.

Another fact that might contribute to the displacement is that the energy calibration comes from measurement of conversion electrons instead of beta particles. For instance a conversion electron is very often followed by an Auger electron which might suffer a rather great energy loss in the source support or detector window and therefore only shift the pulse height by a value corresponding to a few channels in the channel analyser. In this case a certain channel will be given an energy that is too low, in agreement with the measurements.

The measured maximum energies are given in table 4 and compared with normally accepted values.

Table 4

	Experimental	Other experiments
^{203}Hg	204 keV	212 keV
^{198}Au	946 keV	962 keV
^{32}P	1677 keV	1708 keV

It is seen from the table that in the case of ^{203}Hg, which was the most distorted spectrum because of the low energies, the deviation from the accepted value is 3.9%, while the deviations for ^{198}Au and ^{32}P are 1.7% and 1.8% respectively. The measured energies have been given without uncertainties because of the discussed effects, which are still not well enough known.

6. POSSIBLE EXTENDED APPLICATIONS OF THE INSTRUMENT

The system developed is suitable for measurement on isotopes with reasonably long half-lives, not less than a couple of hours. If it was possible to irradiate the source in the system, isotopes with much shorter half-lives could be investigated.

This might be done most easily by putting the system into the cryostat through a slide-bush and having a window placed in the cryostat just above the magnet. On irradiation of the source the whole system is raised in the cryostat so that the source is situated in the beam. After activation the system is again pushed down to its original place with the source and detectors in the magnetic field.

If a split-coil were used, it would even be possible to measure and activate the source at the same time. The space needed to allow the entrance of the activating beam, neutrons, high-energy electrons, or heavy charged particles, should be reasonably large to reduce scattering in the beam channel, see fig. 6.1. As mentioned in subsection 2.4, the field must not dive between the detectors, and the only way to obtain such a field profile with two similar magnets is to use reverse-biased compensating coils. The whole magnetic system will be very expensive because of this condition, and it is not very attractive to use a lot of wire to create the field and then more wire to remove the same field. However, there is another possibility because the only important thing is that the particles do not meet a magnetic barrier while going towards any of the detectors. Therefore the solution of the problem would be a magnetic field steadily decreasing from one detector to the other, which is the case if the source is placed just outside the magnetic coil, but still in the axis of the coil. In this case simultaneous activation and measurement is possible, but because of reduction of possible gamma interaction in the detectors they should, as said earlier, be placed at some distance from the source. In this case the detector outside the magnet will be placed in such a weak field that the 4π-geometry of the instrument is spoilt. For this reason a second magnet might be used to extend the field without any change of the sign of the field gradient. An example of such a system is given in subsection 6.1.

Furthermore the same system with its inhomogeneous magnetic field might be used to measure the angular correlation for conversion electrons as discussed in subsection 6.2.

6.1. Design of Magnets for Split-Coil System

Because of the potential use of this system for angular correlation measurements it will be expedient to take the field strength at the high-field magnet rather high, e.g. 100 kG. If a 20-kG magnet is used as the low-field magnet to give a reasonable field strength for the other detector, figs. 6.1.1 and 6.1.2 show that a space between the coils of about 2 cm may be obtained and that this set-up will give a source to detector distance of about 6 cm with the source in the middle of the space and the "low-field detector" in 20 kG. A 2-cm^2 detector in 20 kG will still give 4π-geometry for electron energies up to 1.5 MeV. Fig. 6.1.1 gives the field distribution both for the 100-kG magnet alone and for the combined field of both magnets with the low-field magnet near its highest allowable field strength. The two magnets are designed to be as cheap as possible for the desired fields in contrast to the 46-kG magnet used, which was made rather long to give a fairly homogeneous magnetic field. In both cases the inner bore in the magnet and the magnetic-field strength in the middle of the magnet are given while the outer diameter and the price of the magnet are calculated vs. the half length, b, of the winding. The winding lengths for the two magnets are taken as 8 cm and 4 cm for the 100-kG and the 20-kG magnet respectively. The full design of the magnets is seen in fig. 6.1.2.

For the 100-kG magnet, "RCA" superconducting ribbon is used, SR 2101 for the inner section and "Supercon" superconducting wire, T 48 B (0.024"), for the outer section. This design has been approved by specialists at "Supercon". For commercial 100-kG magnets, for instance from Oxford Instruments, it is known that RCA-ribbon is used for the whole magnet, SR 2101 for the inner and SR 2100 for the outer section. This is a safer design, but the price will rise by nearly a factor of two.

6.2. Angular Correlation Measurement by Magnetic-Mirror Effect

Angular correlation measurement is a nuclear-spectroscopy method by which certain nuclear parameters can be determined. The most important and most frequently investigated correlation is the γ-γ-correlation, where the angular distribution of the last gamma ray in a cascade is measured relative to the first.

In a γ-γ-cascade in which both gamma rays of multipole orders L_1 and L_2 respectively are pure, the most convenient form of describing the directional correlation is

$$W_{\gamma-\gamma}(\theta) = \sum_{k \text{ even}} A_k P_k(\cos\theta) ; \quad K_{max} = \min(2I, 2L_1, 2L_2), \qquad (6.2.1)$$

where I is the spin in the intermediate state and $P_k(\cos\theta)$ are Legendre polynomials$^{43)}$.

The coefficients A_k are dependent on the multipole order of the emitted radiation and the spins of the three nuclear states, the initial, the intermediate and the final state, but not the parities. The relative parities can be determined, however, if one observes in addition to the direction the polarization of the gamma rays.

Another method of obtaining multipole order as well as spin and parity is measurement of the directional correlation between conversion electrons. Furthermore the conversion correlation depends on the energies of the converted transitions and on the nuclear charge, and thus it may yield more information than the γ-γ-directional correlation. Measurement of the conversion correlation is required in cases where at least one of the transitions is very strongly converted ($\alpha \gg 1$) so that it may even be impossible to measure the γ-γ-correlation, and only the conversion correlation yields the desired information (e.g. ^{121m}Te, ^{123m}Te).

The relativistic theory of the directional correlation involving electrons from the K-shell is due to Rose, Biedenharn and Arfken$^{44, 45)}$. For the cascade in which the gamma rays are replaced by conversion electrons the correlation function is obtained from the γ-γ-correlation function by multiplying each coefficient A_k by a particle parameter $b_k(e^-)$ for each conversion electron$^{43)}$:

$$W_{e^- - e^-}(\theta) = \sum_{k \text{ even}} b_k(e^-_1)\, b_k(e^-_2)\, A_k\, P_k(\cos\theta) ;$$

numerical values for the particle parameters $b_k(e^-)$ for conversion in the K-shell have been calculated in ref. 45. Curves for the coefficients $b_2(e^-)$ are given in ref. 44.

The expressions for the directional correlations for conversion electrons and gamma radiation are formally the same; only the constants are changed. $W(\theta)$ can therefore in both cases be written

$$W(\theta) = \sum_{k\ \text{even}} a_k P_k(\cos\theta) .$$

The expression for $W(\theta)$ assumes that the nucleus is free, i. e. that no extranuclear fields act on the nucleus and disturb its orientation in the intermediate state. The correlation pattern is sensitive to extranuclear fields if the lifetime of the intermediate nuclear state is longer than, say, 10^{-11} sec.

Assuming reasonable conversion ratios, directional correlation experiments involving conversion electrons introduce two characteristic problems: (1) K-electrons must be selected in order to make a comparison with the theoretical calculations meaningful; (2) excessive scattering of the electrons in the source and in the path between source and electron detector must be avoided. The first problem is easily overcome by the use of solid-state detectors. The scattering in gas molecules between the source and the detector can easily be avoided by placing source and detector in vacuum. No complete theory of the scattering of electrons in the source and source backing is available, and the allowable thicknesses of the source and the backing are therefore somewhat uncertain. For estimates one may use the monogram based on Frankel's calculation46). It gives a correction factor defined by

$$A_k^{\text{corr.}} = A_k^{\text{uncorr.}} / c_k ,$$

where c_k depends on the source thickness, the energy of the electrons and the source material. If the lifetime of the intermediate nuclear state is less than 10^{-11} sec, the problem might be reduced by using a very thin source. With a longer lifetime this might give problems because a true correlation demands a suitable environment of the nucleus because of the extranuclear fields.

In the conventional set-up a fixed and a movable detector are used, so that different angles between the detectors may be obtained, see fig. 6. 2. 8. The new set-up discussed in this report uses two fixed detectors on the same axis, but with the desired angles for the electrons determined by an inhomogeneous magnetic field, see fig. 6. 2. 1.

Because of the magnetic field all electrons that leave the source inside the loss cone will be detected by detector 1 and the remaining ones by detector 2. The efficiency of solid-state detectors is 1 for electrons. In this way we have a 4π-geometry, so a single correlation measurement will at the same time give the absolute strength of the source. Backscattering from detector 2 to detector 1 will be reduced without material shielding because of the "magnetic barrier".

The loss cone θ_L is determined by $\sin^2\theta_L = B_o/B_{max}$, where B_o is the field strength at the source and B_{max} is the maximum field strength, which in the figure occurs above the source.

The important question is whether this set-up with the same source strength and time of measurement can give a_2 and a_4 with greater accuracy than the ordinary set-up. (Experience shows that k = 4 will generally be the highest term.) To solve this question, the uncertainties of a_2 and a_4 will be compared in the two cases for the conversion coefficient $\alpha = 1$.

The probability of one particle being emitted in the solid angle $d\Omega_1$, the other in the solid angle $d\Omega_2$ and the angle between the particles being θ (see fig. 6.2.2) is

$$dS = \frac{d\Omega_1}{4\pi} \frac{d\Omega_2}{4\pi} W(\theta)$$

$$dS = \frac{1}{16\pi^2} \sum_k a_k P_k(\cos\theta)\, d\Omega_1\, d\Omega_2 \quad .$$

The probability of having the particles in the finite solid angles Ω_1 and Ω_2 is

$$S = \frac{1}{16\pi^2} \int_{\Omega_1} \int_{\Omega_2} \sum_k a_k P_k(\cos\theta)\, d\Omega_1\, d\Omega_2$$

$$d\Omega_1 = \sin\theta_1\, d\varphi_1\, d\theta_1 ; \qquad d\Omega_2 = \sin\theta_2\, d\varphi_2\, d\theta_2$$

$$S = \frac{1}{16\pi^2} \int_{\varphi_1 \theta_1} \int_{\varphi_2 \theta_2} \sum_k a_k P_k(\cos\theta) \sin\theta_1\, d\varphi_1\, d\theta_1 \sin\theta_2\, d\varphi_2\, d\theta_2 .$$

Using the addition theorem

$$P_k(\cos\theta) = \frac{4\pi}{2k+1} \sum_m Y^*_{km}(\theta_1, \varphi_1)\, Y_{km}(\theta_2, \varphi_2) \quad ,$$

we have

$$S = \frac{1}{16\pi^2} \sum_k a_k \frac{4\pi}{2k+1} \int_{\varphi_1\theta_1} \int_{\varphi_2\theta_2} \sum_m Y^*_{km}(\theta_1,\varphi_1)\, Y_{km}(\theta_2,\varphi_2)\, d\cos\theta_1$$

$$d\cos\theta_2\, d\varphi_1\, d\varphi_2 \ .$$

Using

$$Y^*_{km}(\theta_1, \varphi_1) \cdot Y_{km}(\theta_2, \varphi_2) = f(\theta_1)\, e^{-im\varphi_1} \cdot f(\theta_2)\, e^{im\varphi_2}$$

and

$$\int_0^{2\pi} e^{im\varphi}\, d\varphi = 0 \qquad \text{for} \quad m \neq 0$$

we have

$$\int_{\varphi_1\theta_1} \int_{\varphi_2\theta_2} \sum_m Y^*_{km}(\theta_1, \varphi_1)\, Y_{km}(\theta_2, \varphi_2)\, d\cos\theta_1\, d\cos\theta_2\, d\varphi_1\, d\varphi_2$$

$$= \int_{\varphi_1\theta_1} \int_{\varphi_2\theta_2} Y^*_{k0}(\theta_1, \varphi_1)\, Y_{k0}(\theta_2, \varphi_2)\, d\cos\theta_1\, d\cos\theta_2\, d\varphi_1\, d\varphi_2 \ .$$

$$Y^*_{k0}(\theta_1, \varphi_1) = \sqrt{\frac{2k+1}{4\pi}}\, P_k(\cos\theta_1)$$

$$Y_{k0}(\theta_2, \varphi_2) = \sqrt{\frac{2k+1}{4\pi}}\, P_k(\cos\theta_2) \ ,$$

which gives

$$S = \frac{1}{16\pi^2} \sum_k a_k \int_{\varphi_1\theta_1} \int_{\varphi_2\theta_2} P_k(\cos\theta_1)\, P_k(\cos\theta_2)\, d\cos\theta_1\, d\cos\theta_2\, d\varphi_1\, d\varphi_2$$

or

$$S = \frac{1}{4} \sum_k a_k \left\{ \int_{\theta_1} P_k(\cos\theta_1)\, d\cos\theta_1 \int_{\theta_2} P_k(\cos\theta_2)\, d\cos\theta_2 \right\} .$$

The expression gives the probability of one of the particles being emitted through band 1 and the other being emitted through band 2 in fig. 6.2.2 with regard to the angular correlation. $a_2 = a_4 = 0$ means isotropic distribution.

a_0 can be determined by using the orthogonality of the Legendre polynomiums together with $P_0(\cos\theta) = 1$:

$$S = \frac{1}{4} \sum_k a_k \left\{ \int_\theta P_k(\cos\theta)\, P_0(\cos\theta)\, d\cos\theta \right\}^2 .$$

Integration over the whole space will give S = 1, from which $a_0 = 1$.

Calculation of the required integrals will give the following: The probability of both particles being emitted in the loss cone:

$$S_{cc} = F_{1cc}(\theta_L) + a_2 F_2(\theta_L) + a_4 F_4(\theta_L) . \qquad (6.2.1)$$

The probability of one particle in the loss cone and the other outside:

$$S_{co} = 2(F_{1co}(\theta_L) - a_2 F_2(\theta_L) - a_4 F_4(\theta_L)) . \qquad (6.2.2)$$

The probability of both particles outside the loss cone:

$$S_{oo} = F_{1oo}(\theta_L) + a_2 F_2(\theta_L) + a_4 F_4(\theta_L) , \qquad (6.2.3)$$

where

$$F_{1cc}(\theta_L) = \frac{1}{4}(1-\cos\theta_L)^2 \qquad (6.2.4)$$

$$F_{1co}(\theta_L) = \frac{1}{4}(1-\cos^2\theta_L) \qquad (6.2.5)$$

$$F_{1oo}(\theta_L) = \frac{1}{4}(1+\cos\theta_L)^2 \qquad (6.2.6)$$

$$F_2(\theta_L) = \frac{1}{16}(\cos^3\theta_L - \cos\theta_L)^2 \qquad (6.2.7)$$

$$F_4(\theta_L) = \frac{1}{256}(7\cos^5\theta_L - 10\cos^3\theta_L + 3\cos\theta_L)^2 . \qquad (6.2.8)$$

Necessarily $S_{cc} + S_{co} + S_{oo} = 1$.

a_2 and a_4 appear in the same way in the three expressions, so in reality there is only one equation to determine the two constants. It is therefore necessary to measure at two different loss angles, θ_1 and θ_2. From the measurements the probabilities S_{cc}, S_{co} and S_{oo} cannot be determined, only the total counts W_{cc}, W_{co} and W_{oo}, where W = NS with N as the total emission of electrons during the time of accumulation. The three expressions will then be

$$W_{cc} = f_{1cc}(\theta_L) + a_2 f_2(\theta_L) + a_4 f_4(\theta_L)$$

$$W_{co} = 2(f_{1co}(\theta_L) - a_2 f_2(\theta_L) - a_4 f_4(\theta_L))$$

$$W_{oo} = f_{1oo}(\theta_L) + a_2 f_2(\theta_L) + a_4 f_4(\theta_L) ,$$

where $f_i(\theta_L) = N \cdot F_i(\theta_L) \qquad i = 1, 2, 4.$

For measurements at the two angles θ_1 and θ_2 we have, using the first equation,

$$a_2 = \frac{(W(\theta_1) - f_1(\theta_1))\, f_4(\theta_2) - (W(\theta_2) - f_1(\theta_2))\, f_4(\theta_1)}{f_2(\theta_1)\, f_4(\theta_2) - f_2(\theta_2)\, f_4(\theta_1)} \qquad (6.2.9)$$

$$a_4 = \frac{(W(\theta_2) - f_1(\theta_2))\, f_2(\theta_1) - (W(\theta_1) - f_1(\theta_1))\, f_2(\theta_2)}{f_2(\theta_1)\, f_4(\theta_2) - f_2(\theta_2)\, f_4(\theta_1)} \qquad (6.2.10)$$

with index cc omitted.

If N is taken without uncertainty (the measurement could be made with present N) and the loss angles θ_1 and θ_2 are assumed to be determined so accurately that their uncertainties are negligible, we have

$$\frac{sa_2}{a_2} = \frac{\sqrt{f_4^2(\theta_2)\, W(\theta_1) + f_4^2(\theta_1)\, W(\theta_2)}}{(W(\theta_1) - f_1(\theta_1))\, f_4(\theta_2) - (W(\theta_2) - f_1(\theta_2))\, f_4(\theta_1)}$$

$$\frac{sa_4}{a_4} = \frac{\sqrt{f_2^2(\theta_1)\, W(\theta_2) + f_2^2(\theta_2)\, W(\theta_1)}}{(W(\theta_2) - f_1(\theta_2))\, f_2(\theta_1) - (W(\theta_1) - f_1(\theta_1))\, f_2(\theta_2)}$$

or

$$\frac{sa_2}{a_2} = \frac{\sqrt{F_4^2(\theta_2)\, S_{cc}(\theta_1) + F_4^2(\theta_1)\, S_{cc}(\theta_2)}}{\sqrt{N}\ \{(S_{cc}(\theta_1) - F_{1cc}(\theta_1))\, F_4(\theta_2) - (S_{cc}(\theta_2) - F_{1cc}(\theta_2))\, F_4(\theta_1)\}}$$

(6.2.11)

$$\frac{sa_4}{a_4} = \frac{\sqrt{F_2^2(\theta_1)\, S_{cc}(\theta_2) + F_2^2(\theta_2)\, S_{cc}(\theta_1)}}{\sqrt{N}\ \{(S_{cc}(\theta_2) - F_{1cc}(\theta_2))F_2(\theta_1) - (S_{cc}(\theta_1) - F_{1cc}(\theta_1))F_2(\theta_2)\}} \,. \tag{6.2.12}$$

When a_2 and a_4 are to be determined for a given cascade, the angles giving the smallest values for the relative uncertainties should be used. Exact calculations of these angles demand knowledge of S_{cc} at different angles. Such knowledge might be acquired by measuring W_{cc}, which gives S_{cc}, for a number of combinations of θ_1 and θ_2, and calculating sa/a, which would be a laborious task, or S_{cc} could be calculated from equation (6.2.1) if a_2 and a_4 are known; this will be the case if a decay investigated earlier is to be reinvestigated for higher accuracy. However, it is possible to make an approximation giving a reasonable choice of the angles to be used.

First it should be noted that $F_4(\theta) = 0$ for $\theta = 49.1^o$; hence sa_2/a_2 is independent of θ_2 if $\theta_1 = 49.1^o$:

$$\left.\frac{sa_2}{a_2}\right|_{\theta_1=49.1^o} = \left.\frac{\sqrt{S_{cc}(\theta_1)}}{\sqrt{N}(S_{cc}(\theta_1) - F_{1cc}(\theta_1))}\right|_{\theta_1=49.1^o} \simeq \left.\frac{\sqrt{F_{1cc}(\theta_1)}}{\sqrt{N}\, a_2\, F_2(\theta_1)}\right|_{\theta_1=49.1^o} .$$

$F_4(\theta_1) = 0$ will decrease the numerator in eq. (6.2.11), while its influence on the denominator cannot be given generally. Nevertheless the choice of θ_1 may be expected to be fair if only $\theta_1 = 49.1^o$ is reasonable for the ratio $\sqrt{F_{1cc}(\theta_1)}/F_2(\theta_1)$. This ratio is shown in dependence on θ_1 in fig. 6.2.3; it is seen that $\theta_1 = 49.1^o$ is a good choice.

From eq. (6.2.9) it is seen that with this choice of θ, a_2 may be determined by only one measurement.

In the case of a_4 we then have

$$\frac{sa_4}{a_4} = \frac{\sqrt{F_2^2(49.1)\, S_{cc}(\theta_2) + F_2^2(\theta_2)\, S_{cc}(49.1)}}{\sqrt{N}\ \{(S_{cc}(\theta_2) - F_{1cc}(\theta_2))F_2(49.1) - (S_{cc}(49.1) - F_{1cc}(49.1))F_2(\theta_2)\}}$$

$$\frac{sa_4}{a_4} \simeq \frac{\sqrt{F_{1cc}(\theta_2) + F_2^2(\theta_2) \cdot F_{1cc}(49.1)/F_2^2(49.1)}}{\sqrt{N}\, a_4\, F_4(\theta_2)} \quad \text{using } F_4(49.1) = 0 .$$

The ratio $\sqrt{F_{1cc}(\theta_2) + F_2^2(\theta_2) \cdot F_{1cc}(49.1)/F_2^2(49.1)}/F_4(\theta_2)$ is shown in fig. 6.2.4; the best choice for θ_2 is seen to be 22.5°.

The angles obtained give

$$sa_2 = \frac{20.5}{\sqrt{N}} \qquad sa_4 = \frac{70}{\sqrt{N}} .$$

As an example is taken the cascade 165 keV-133 keV for ^{197}Hg (see fig. 6.2.5), which is especially suitable for the e^- - e^- correlation. The transitions are known to be M4 and E2, and their theoretical correlation coefficients are $a_2 = 0.450$ and $a_4 = 0.032$ 47), neglecting attenuation due to extranuclear fields because of the half-life of 7 nsec in the intermediate state, and neglecting a possible weak mixing of E5 into M4 in the first transition 48).

Figs. 6.2.6 and 6.2.7 show the dependence of the relative uncertainties of a_2 and a_4 on different angle combinations. In agreement with the general considerations it is seen that the above-mentioned angles are a reasonable choice, giving the uncertainties $sa_2 = 21/\sqrt{N}$ and $sa_4 = 95/\sqrt{N}$.

Furthermore the curves show that the choice of angle combinations is very important for the uncertainties and that a decidedly unfavourable choice could be made, for instance $\theta_1 = 30^\circ$ and $\theta_2 = 70^\circ$ or vice versa.

The angles 22.5° and 49.1° require the source to be placed in 14.6 kG and 57.1 kG respectively if $B_{max} = 100$ kG. The placing in the magnetical system might then be found from the field distribution curve in fig. 6.1.1. In the case of 14.6 kG the "low-field detector" could not be placed in 20 kG as assumed in subsection 6.1. However, with a 2-cm^2 detector in 10 kG, 4π geometry could still be obtained for electron energies up to a little above 600 keV, which is sufficient in the case of ^{197}Hg. If the field strength of the low-field magnet and the space between the two magnets are adjusted so that the horizontal tangent of the total magnetic-field distribution appears at about 15 kG, the source to detector distance may be improved, decreasing the interaction probability of possible gamma rays.

The principle of a conventional set-up for angular correlation measurement is shown in fig. 6.2.8.

Assuming full absorption in the detectors we have, as in the case discussed above, the probability of one particle in each detector:

$$S = \int_{\Omega_1}\int_{\Omega_2} \frac{d\Omega_1}{4\pi}\frac{d\Omega_2}{4\pi} W(\theta') = \frac{1}{16\pi^2} \sum_k a_k \int_{\Omega_1}\int_{\Omega_2} P_k(\cos\theta')\, d\Omega_1\, d\Omega_2 \ .$$

Following the development of Rose[49)], using the addition theorem twice, we have the required integrals

$$I_k = \int_{\Omega_1}\int_{\Omega_2} P_k(\cos\theta')\, d\Omega_1 \quad d\Omega_2 = 4\pi^2 P_k(\cos\theta)\, J_k(1)\, J_k(2) \ .$$

On the assumption of equal detectors, $J_k(1) = J_k(2) = J_k$ where

$$J_k = \int_0^{\gamma} P_k(\cos\beta) \sin\beta\, d\beta$$

$$I_k = 4\pi^2 P_k(\cos\theta) \left\{ \int_0^{\gamma} P_k(\cos\beta)\, d\cos\beta \right\}^2 .$$

According to the case discussed above this gives

$$S = F_1(\gamma) + a_2 P_2(\cos\theta) F_2(\gamma) + a_4 P_4(\cos\theta) F_4(\gamma)$$

with the F functions taken from eqs. (6.2.4), (6.2.7) and (6.2.8). In this case, where we do not have a 4π-geometry to give the total emission N, it is necessary to measure at three different angles in order to determine the three unknowns N, a_2 and a_4. We then have to solve the system of the three equations:

$$F_1(\gamma) = \frac{1}{N} W(\theta_i) - a_2 F_2(\gamma) P_2(\cos\theta_i) - a_4 F_4(\gamma) P_4(\cos\theta_i) \qquad i = 1, 2, 3,$$

which gives for instance

$$a_2 = \frac{F_1(\gamma)\,[\,W(\theta_1)(P_4(\theta_2) - P_4(\theta_3)) - W(\theta_2)(P_4(\theta_1) - P_4(\theta_3))}{F_2(\gamma)\,[\,W(\theta_1)(P_2(\theta_2)\,P_4(\theta_3) - P_2(\theta_3)\,P_4(\theta_2)) - W(\theta_2)(P_2(\theta_1)\,P_4(\theta_3)}$$

$$\frac{+\,W(\theta_3)(P_4(\theta_1) - P_4(\theta_2))\,]}{-P_2(\theta_3)\,P_4(\theta_1)) + W(\theta_3)(P_2(\theta_1)\,P_4(\theta_2) - P_2(\theta_2)\,P_4(\theta_1))\,]} \ .$$

In this set-up, where measurement at three different angles is necessary, a simple investigation of the optimal angles is not possible, but the commonly used angles are 90°, 135° and 180°, and according to the development of Gimmi et al.$^{48)}$ this will give

$$a_2 = \frac{F_1(\gamma)}{F_2(\gamma)} \ \frac{10(5A + 4U)}{7A + 56U + 105} \ ,$$

where

$$A = \frac{W(180^\circ) - W(90^\circ)}{W(90^\circ)} \quad \text{and} \quad U = \frac{W(135^\circ) - W(90^\circ)}{W(90^\circ)} \ .$$

The relative statistical uncertainty of a_2 is derived as follows:

$$\frac{sW}{W} \simeq \frac{1}{\sqrt{N \cdot S}} \ .$$

For the auxiliary functions A and U we have, neglecting the relative uncertainty of the denominator compared with the much larger one of the numerator,

$$\frac{sA}{A} \simeq \frac{sW\sqrt{2}}{W(180^\circ) - W(90^\circ)} \qquad sA \simeq \frac{sW\sqrt{2}}{W} \quad \text{or} \quad sA \simeq sU \simeq \sqrt{\frac{2}{N \cdot S}} \ ;$$

a_2 then gets the relative uncertainty

$$\frac{sa_2}{a_2} \simeq \sqrt{\frac{82}{(5A + 4U)^2} + \frac{6370}{(7A + 56U + 105)^2}} \ \frac{1}{\sqrt{N \cdot S}} \ .$$

For a_4 we have quite similarly

$$a_4 = \frac{F_1(\gamma)}{F_4(\gamma)} \, \frac{48(A - 2U)}{7A + 56U + 105} \; ,$$

which gives

$$\frac{s a_4}{a_4} \simeq \sqrt{\frac{10}{(A - 2U)^2} + \frac{6370}{(7A + 56U + 105)^2}} \; \frac{1}{\sqrt{N \cdot S}} \; .$$

With the use of $\gamma = 20^{\circ}$, to get a reasonable intensity, calculations on the case ^{197}Hg with $a_2 = 0.450$ and $a_4 = 0.032$ give

$$s a_2 = \frac{31.7}{\sqrt{N}} \qquad\qquad s a_4 = \frac{80}{\sqrt{N}} \; .$$

As seen from the calculations, the two set-ups are equal for conversion electron correlations with respect to uncertainty if the acceptance angle γ (see fig. 6.2.8) is taken not less than 20°, but other circumstances speak for the new method. First the conventional set-up requires measurement at three different angles while the new only needs two different angles, which furthermore might very conveniently be calculated to the best uncertainty. If only a_2 is wanted, even a single measurement will do.

Furthermore, the backscattering from the "low-field detector" will be decreased without material shielding, as said previously, because of the "magnetic barrier".

7. CONCLUSION

On comparison of the results obtained with the instrument it is seen that it is very suitable for measurement of line spectra, and a very high accuracy can be obtained in calculations on these spectra. In the case of continuous spectra the instrument is usable, but still there are some distorting instrumental effects which prevent the high accuracy hoped for. The main problem in these effects is the tail of the peaks discussed, and to clear this problem properly, careful investigations with a coincidence set-up will be necessary as mentioned in subsection 4.2. These measurements have not been possible with the instrumental set-up used, but will demand another detector mounted in the system; they will probably be taken up at a later time.

ACKNOWLEDGEMENTS

The author wants to thank C. J. Christensen very much for his inspiring collaboration and P. Andersen, F. Hansen and J. Strømstad for their excellent technical support.

The work was carried out in the Physics Department of the Danish AEC Research Establishment Risö, and the author is indebted to Professor O. Kofoed-Hansen, head of the department, for his support and interest.

A scholarship from the Technical University of Denmark and the possibility to finish the work after my employment at Risö are acknowledged.

ABBREVIATIONS

FET:	field effect transistor
FK:	Fermi-Kurie
fwhm:	full width at half maximum
VYNS:	no direct abbreviation, but a designation of a polyvinyl chloride acetate copolymer compound (~ 85% chloride, ~ 15% acetate).

REFERENCES

1) J.T. Holloway, D.C. Lu and D.J. Zaffarano, Revs. Sci. Instr. 31 (1960) 91-95.

2) C.J. Christensen, A. Nielsen, A. Bahnsen, W.K. Brown, and B.M. Rustad, Phys. Letters 26B (1968) 11-13.

3) V. Andersen and C.J. Christensen, Nucl. Instr. Meth. 61 (1968) 77-83.

4) W.M. Gibson, G.L. Miller and P.F. Donovan, in: K. Siegbahn (editor), Alpha-, Beta- and Gamma-Ray Spectroscopy (North-Holland Publishing Company, Amsterdam, 1965) 345-378.

5) Fred S. Goulding, Nucleonics 22 (1964) 54-61.

6) V. Andersen, Nucl. Instr. Meth. 65 (1968) 225-227.

7) D.N. Cornish, Culham Laboratory, Perks, personal communication.

8) Supercon, General Catalog and Specification Sheets (Jan. 1, 1965).

9) S. Hagström, C. Nordling and K. Siegbahn, in ref. 4, 845-862.

10) G. Knop and W. Paul, in ref. 4, 1-25.

11) H. Frank, Z. Naturf. 14a (1959) 247-261.

12) B.G. Pettersson, in ref. 4, 1579-1582.

13) L. Spruch and G. Goertzel, Phys. Rev. 94 (1954) 1671-1678.

14) E.B. Shera, M.P. Bedesem and K.J. Casper, Rev. Sci. Instr. 38 (1967) 1110-1114.

15) A. Smekal, Z. Physik 10 (1922) 275.

16) M.H. Hebb and G.E. Uhlenbeck, Physica 5 (1938) 605-608.

17) B.N. Subba Rao, Nucl. Instr. Meth. 45 (1966) 22-40.

18) C.M. Davisson, in ref. 4, 827-839.

19) A.M. Iakobson, JETP 2 (1956) 751-753.

20) D.E. Alburger and A.W. Sunyar, Phys. Rev. 99 (1955) 695-702.

21) V. Andersen and C.J. Christensen, Nucl. Phys. A113 (1968) 81-85.

22) R.S. Hager and E.C. Seltzer, Nuclear Data A4 (1968) 1-235.

23) F.P. Brady, N.F. Peek and R.A. Warner, Nucl. Phys. 66 (1965) 365-368.

24) S.I.H. Rizvi and S.K. Sen, Bull. Am. Phys. Soc. 12 (1967) 715.

25) P. Kleinheinz, R. Vukanovic, L. Samuelsson, D. Krmpotic, H. Lindström, and K. Siegbahn, Nucl. Phys. A93 (1967) 63-73.

26) B. van Nooijen and H. van Krugten, Phys. Letters 25B (1967) 510-511.

27) I. Bergström and C. Nordling, in ref. 4, 1523-1543.

28) F. Pleasonton and A.H. Snell, Proc. Roy. Soc. A241 (1957) 141-152.

29) Nuclear Data Sheets, National Academy of Sciences, National Research Council.

30) M.E. Rose, Internal Conversion Coefficients (North-Holland Publishing Company, Amsterdam, 1958).

31) R.M. Steffen, O. Huber and F. Humbel, Helv. Phys. Acta 22 (1949) 167-223.

32) D. Saxon and R. Heller, Phys. Rev. 75 (1949) 909-910.

33) L. Simons, Phys. Rev. 86 (1952) 570.

34) A.C.G. Mitchell, in ref. 4, 485-491.

35) M. Goeppert Mayer and J.H.D. Jensen, in ref. 4, 578-580.

36) C.S. Wu, in ref. 4, 1365-1389.

37) R. Quivy, C.R. Congres Int. de Phys. Nucl., Paris, 2 (1965) 1176. J. de Physique 26 (1965) 241-245.

38) B. Persson and J. Reynolds, Nucl. Phys. 66 (1965) 439-448.

39) B.S. Dzhelepov and L.N. Zyryanova, Vliyanie elektricheskogo Polya atoma na beta raspad (The Influence of the Atomic Electric Field on Beta Decay), AN SSSR, 1956.

40) H.W. Wilson and S.C. Curran, Phil. Mag. 42 (1951) 762-774.

41) S. Thulin and K. Nyboe, Arkiv for Fysik I (1954) 289-290.

42) N. Marty, Compt. Rend. 240 (1955) 291-294.

43) H. Frauenfelder and R.M. Steffen, in ref. 4, 997-1100.

44) M.E. Rose, L.C. Biedenharn and G.B. Arfken, Phys. Rev. 85 (1952) 5-16.

45) L.C. Biedenharn and M.E. Rose, Rev. Mod. Phys. 25 (1953) 729-776.

46) S. Frankel, Phys. Rev. 83 (1951) 673.

47) E. Breitenberger, Nature 173 (1954) 737-738.

48) F. Gimmi, E. Heer and P. Sherrer, Helv. Phys. Acta 29 (1956) 147-186.

49) M. E. Rose, Phys. Rev. 91 (1953) 610-615.

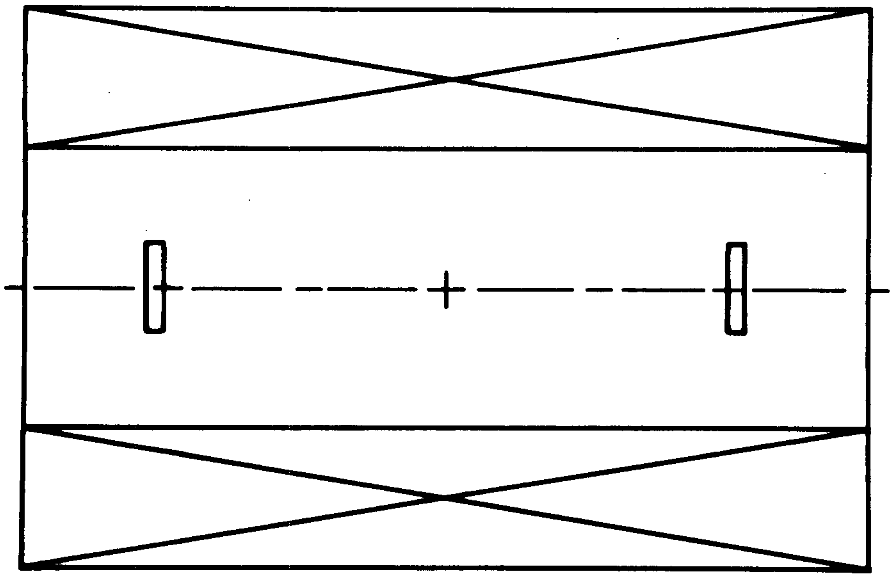

Fig. 2.1. Cut in the superconducting magnet showing the positions of detectors and source.

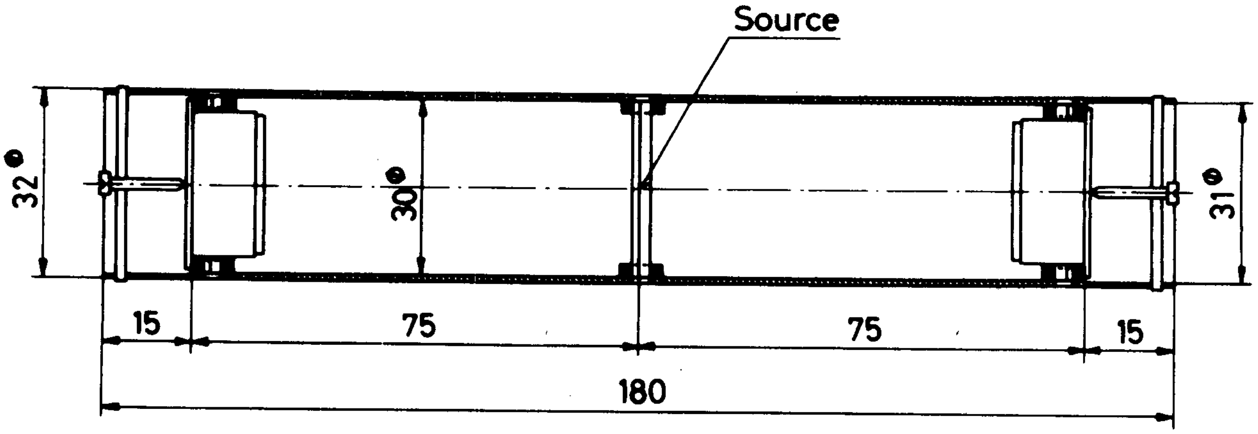

Fig. 2.2. Cut in the counting chamber showing the mounting of detectors and source.

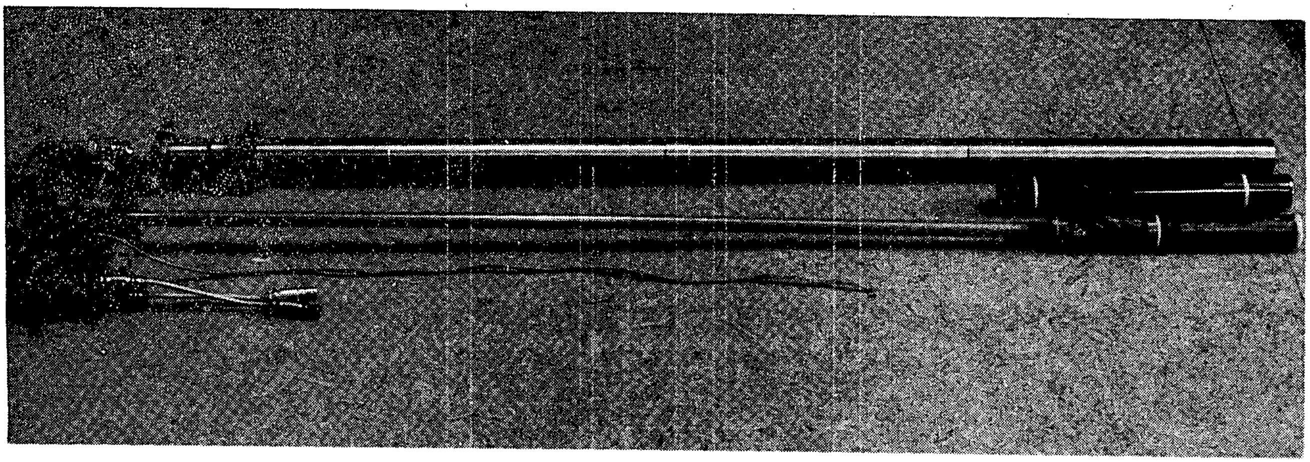

Fig. 2.3. The disassembled system.

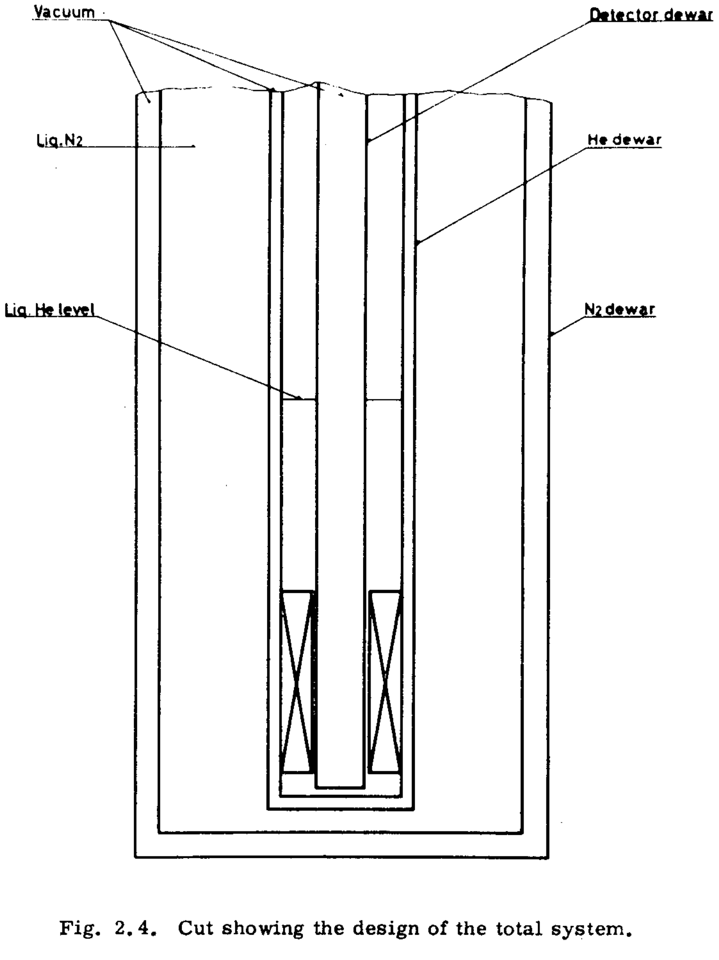

Fig. 2.4. Cut showing the design of the total system.

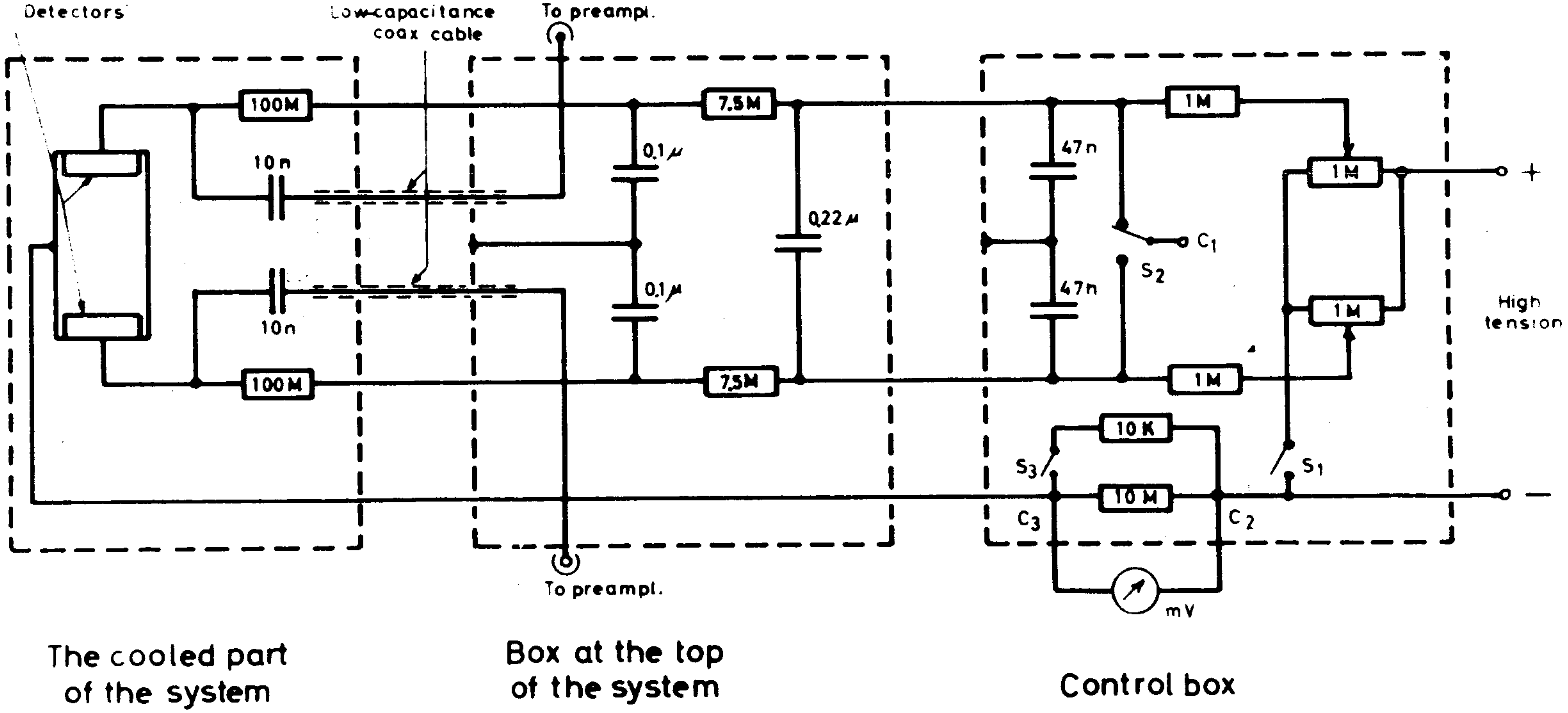

Fig. 2.5. Diagram of the electrical set-up.

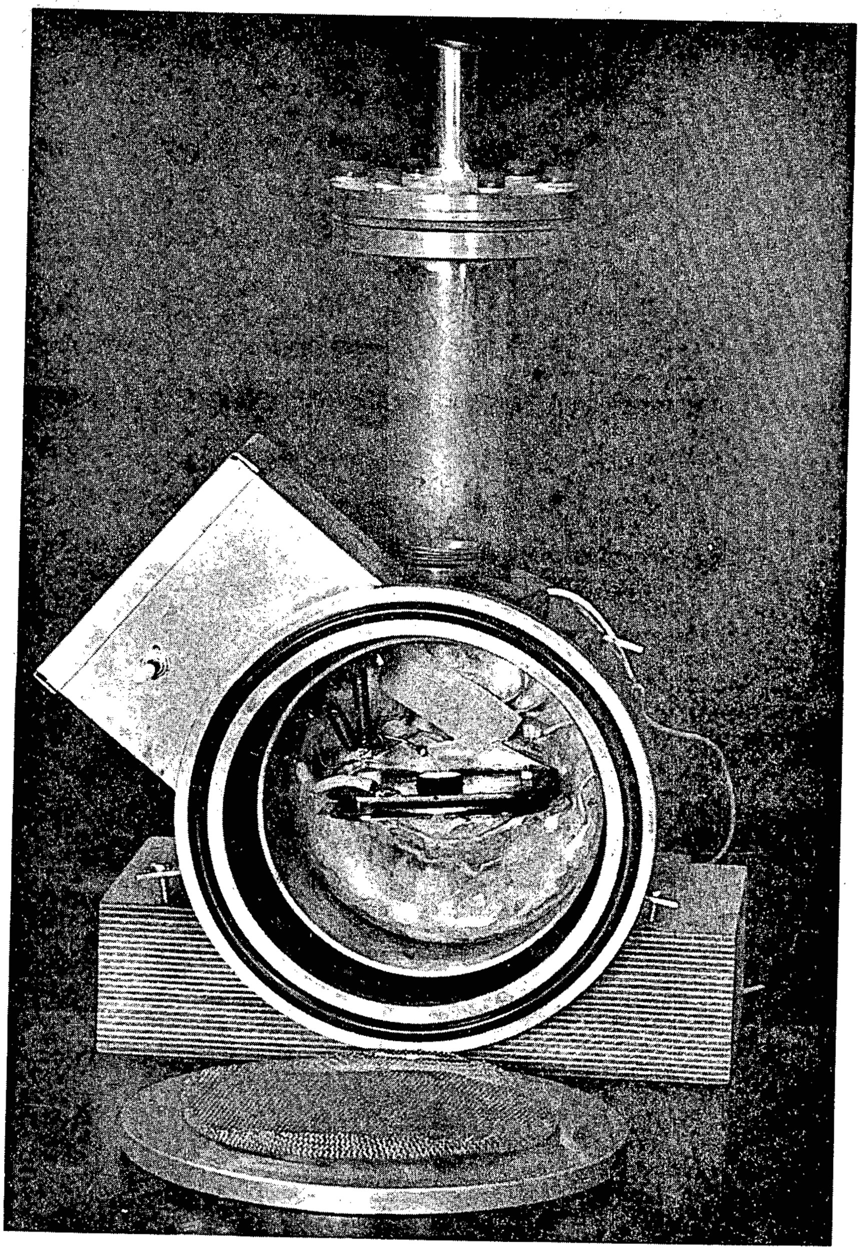

Fig. 2.1.1. Test chamber for the detectors.

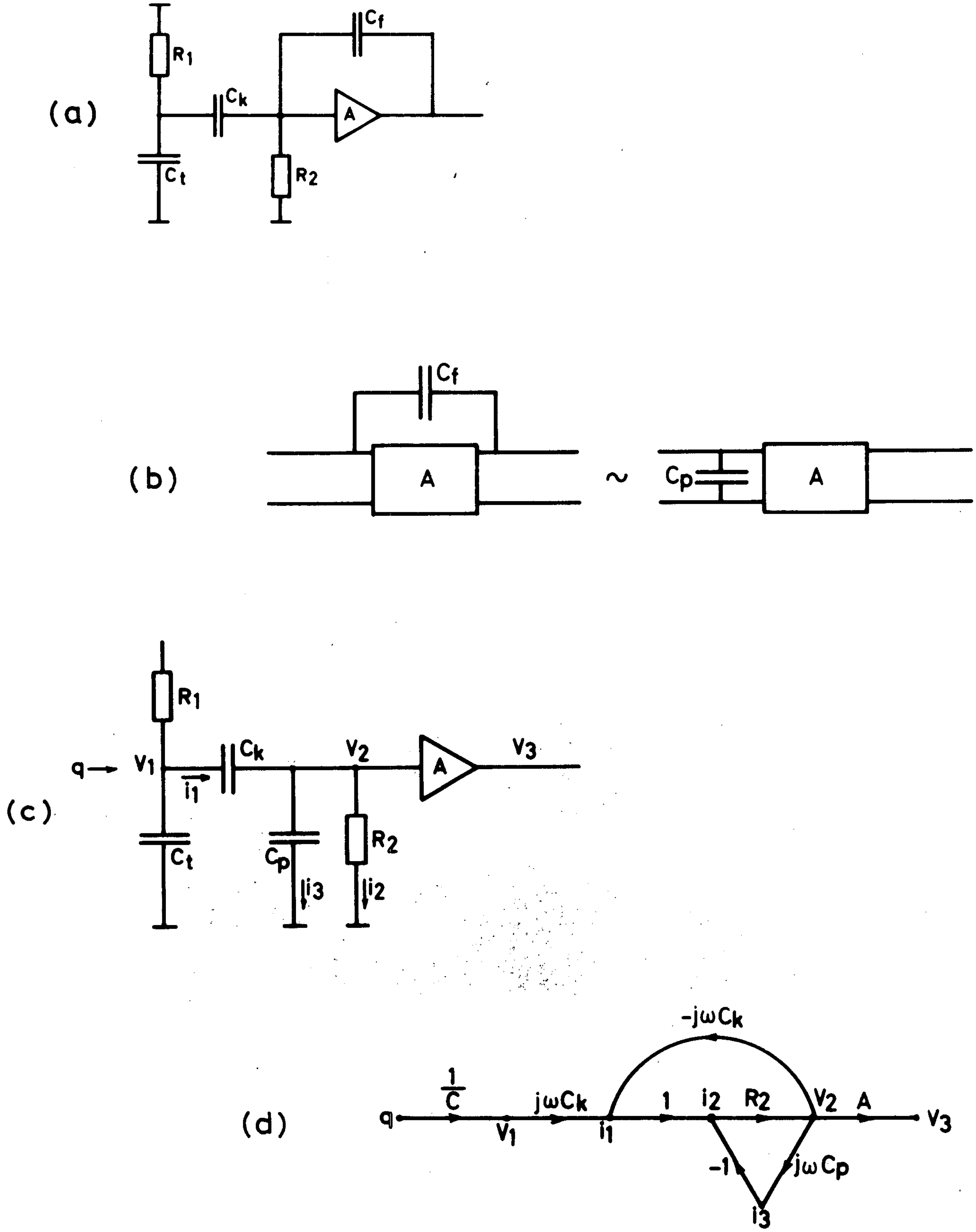

Fig. 2.2.1. The circuit configuration of the charge-sensitive part of the preamplifier, with signal flow graph.

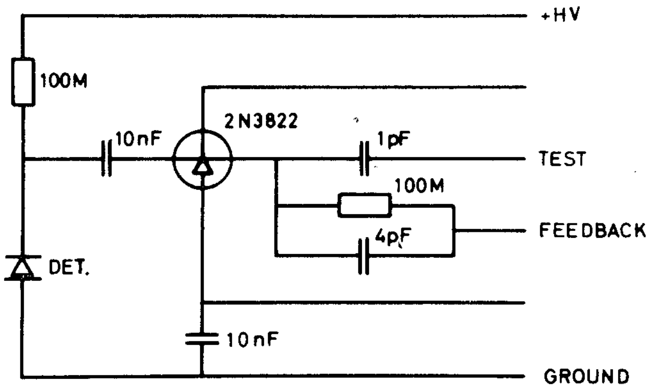

Fig. 2.2.2. Set-up for each detector in the cooled part of the system.

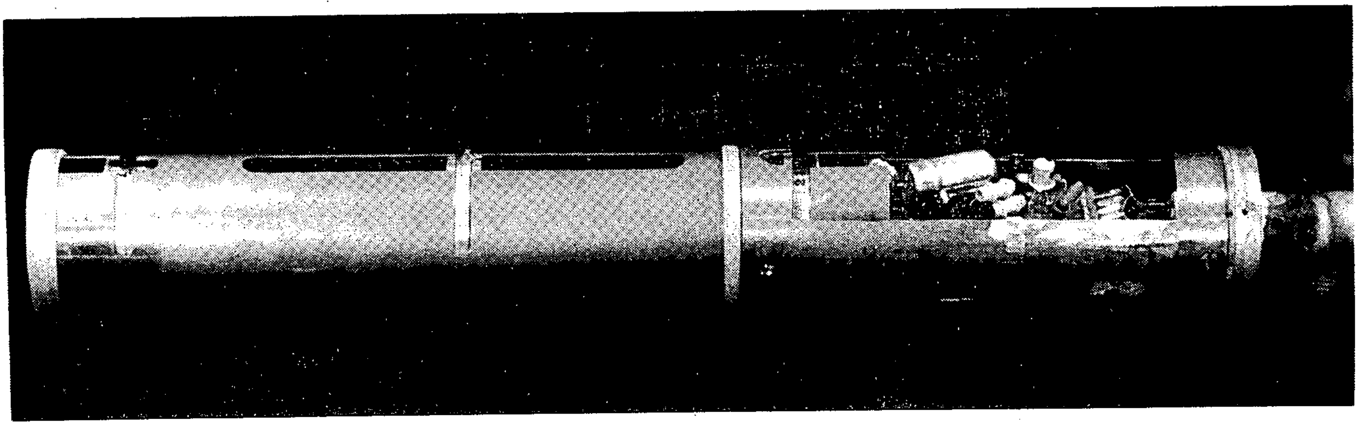

Fig. 2.2.3. The counting chamber with the first stage of the preamplifier.

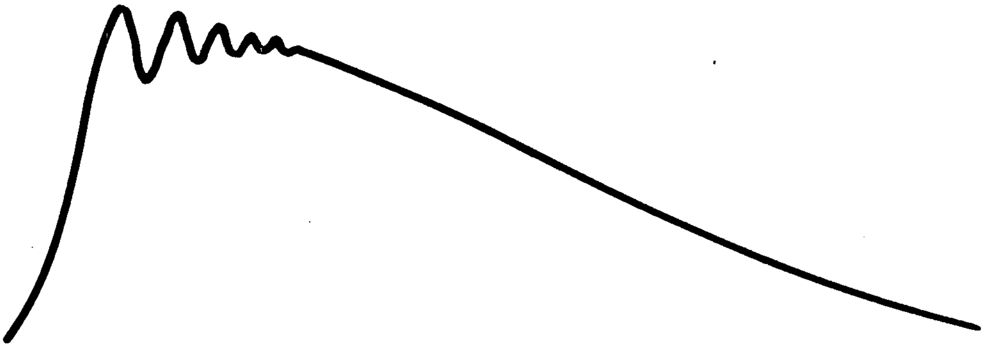

Fig. 2.2.4. Shape of the pulse after the charge-sensitive part of the preamplifier.

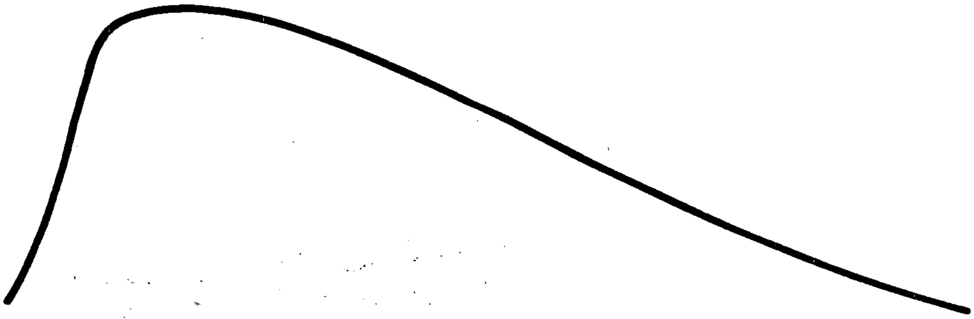

Fig. 2.2.5. Shape of the pulse in fig. 2.2.4 after integration.

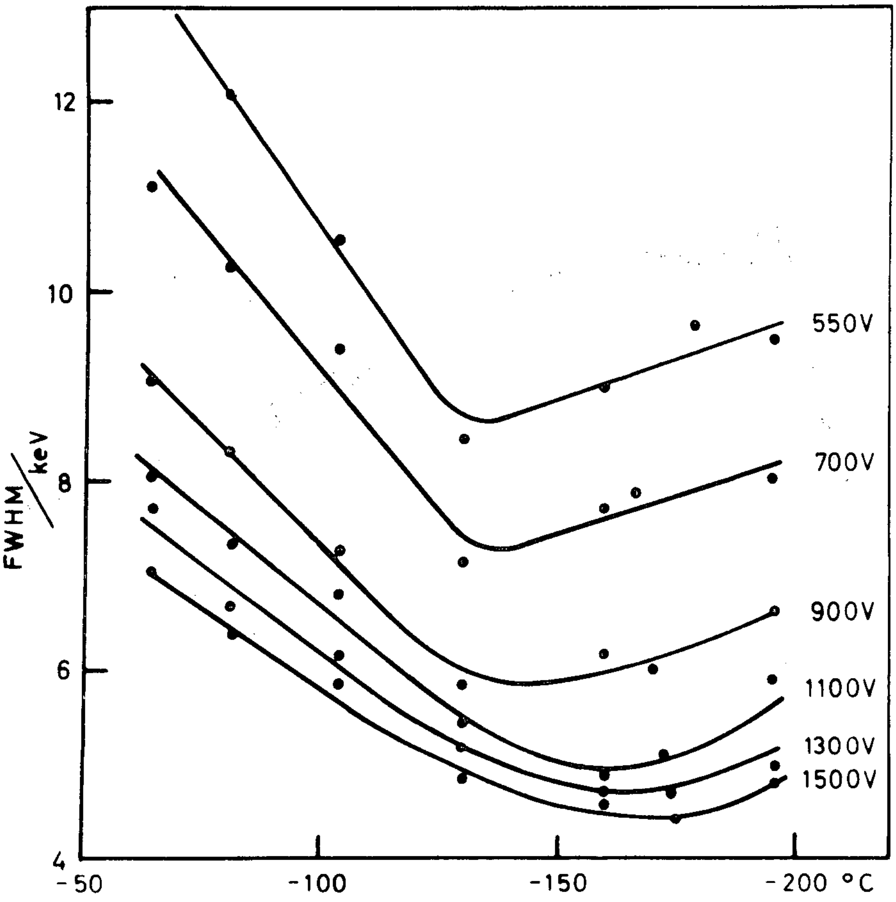

Fig. 2.2.6. The resolution of the system with a single detector vs bias and temperature of the detector.

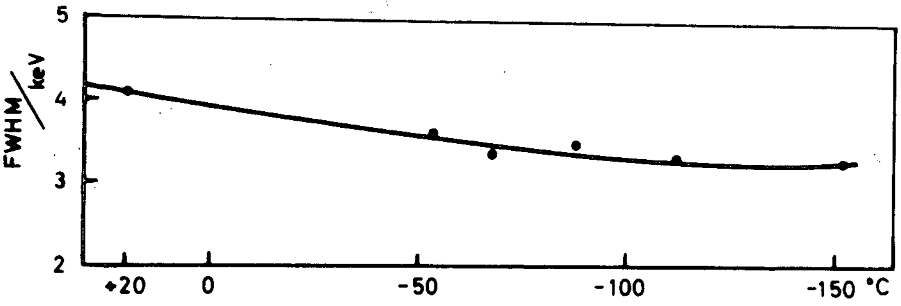

Fig. 2.2.7. The resolution of the same system as in fig. 2.2.6 minus detector vs the temperature of the FET.

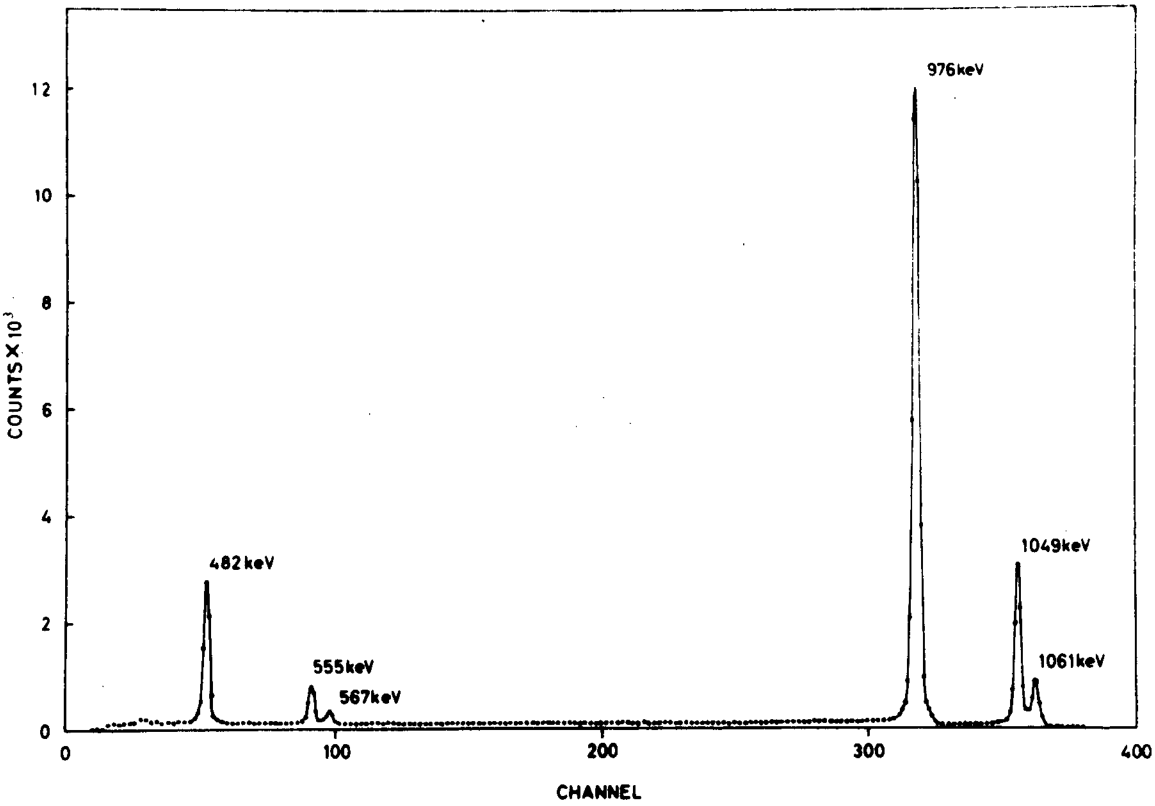

Fig. 2.2.8. Conversion-electron spectrum of ^{207}Bi with a single detector in the spectrometer.

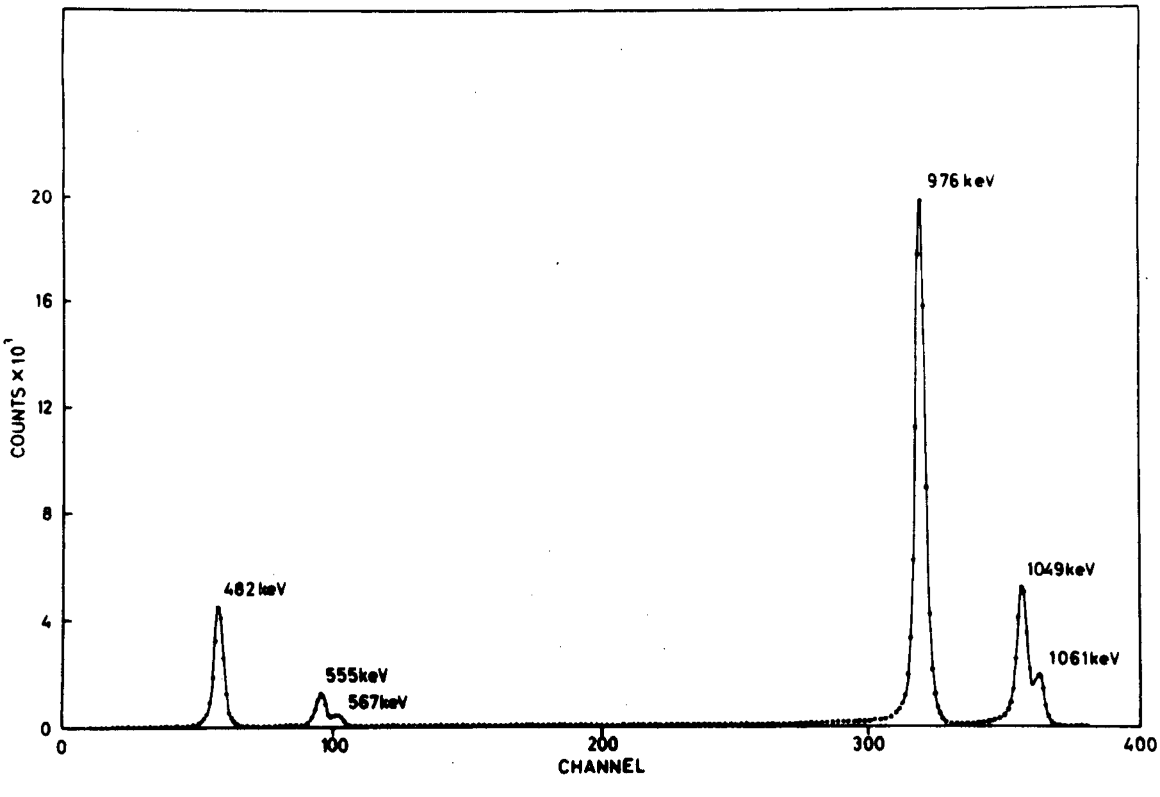

Fig. 2.2.9. Conversion-electron spectrum of ^{207}Bi with parallel-operating detectors.

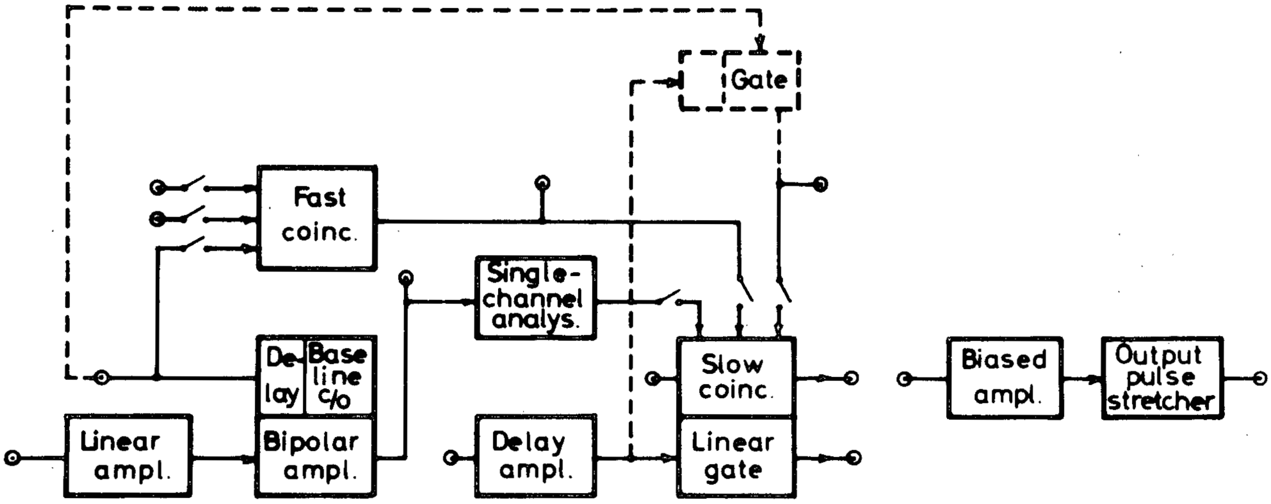

Fig. 2.3.1. Block diagram of the linear pulse analysis system.

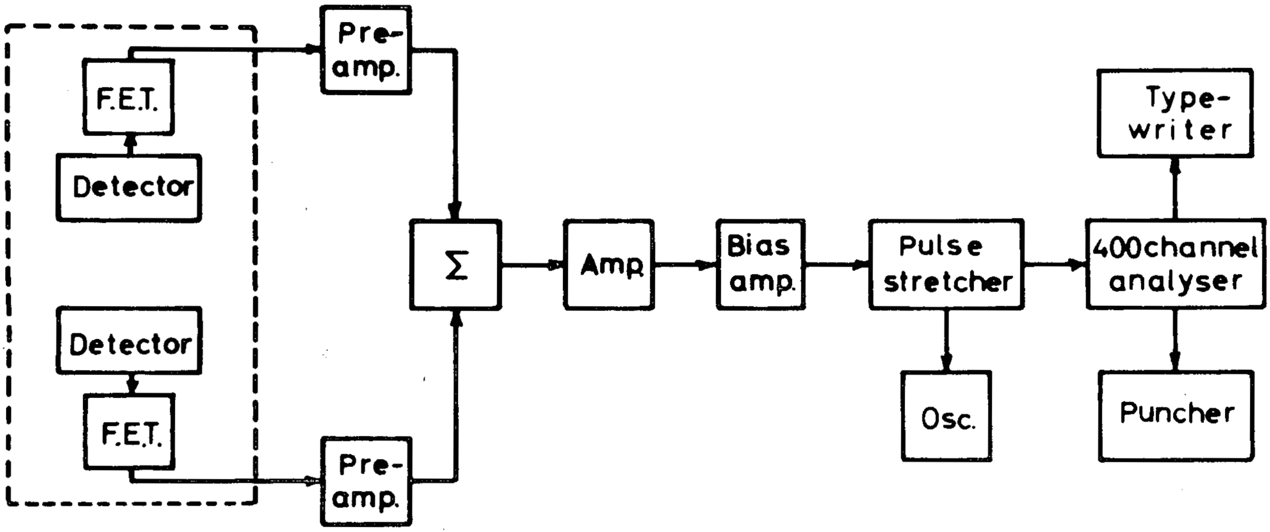

Fig. 2.3.2. Block diagram of the set-up normally used.

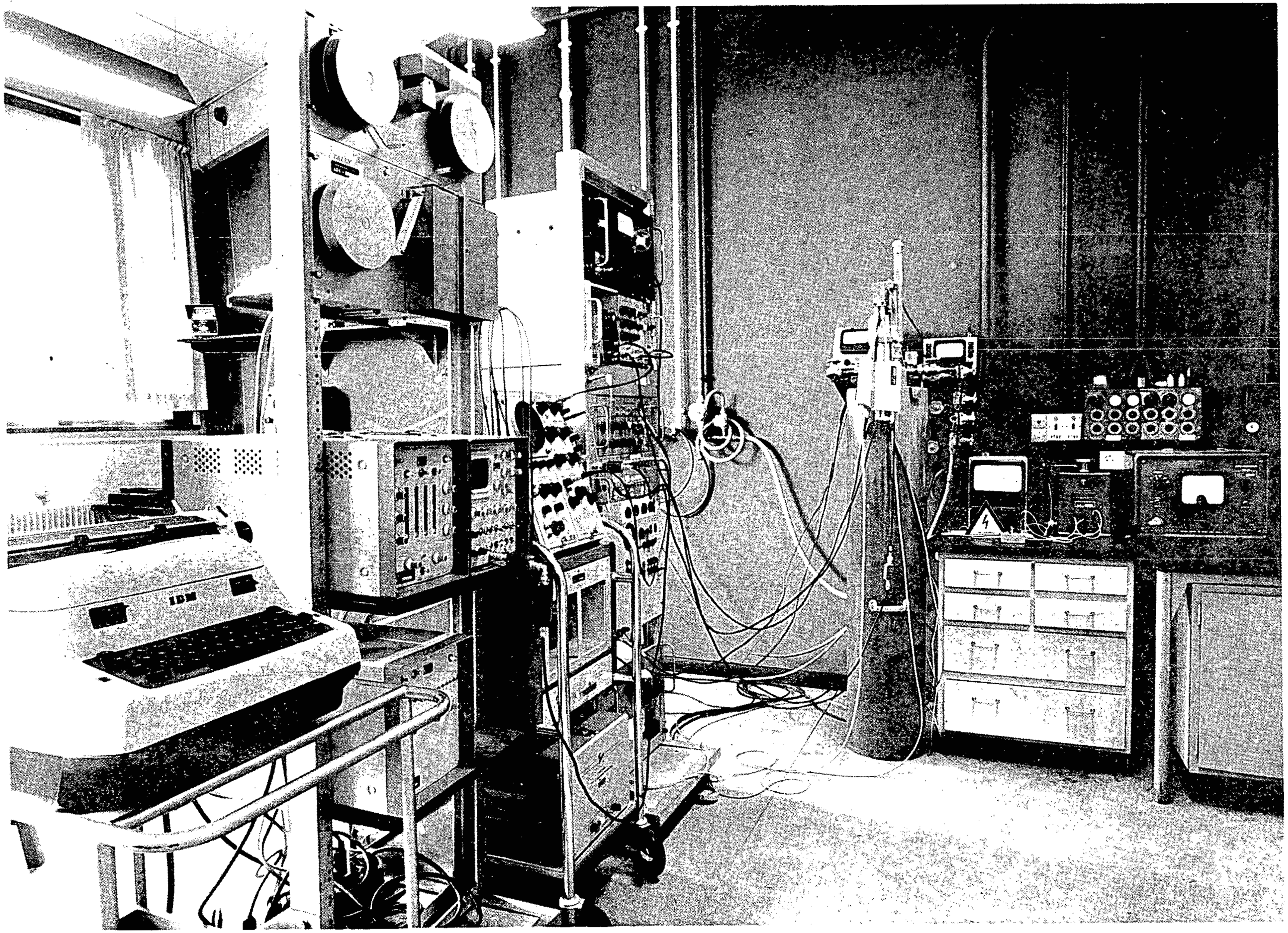

Fig. 2.3.3. The total measuring equipment.

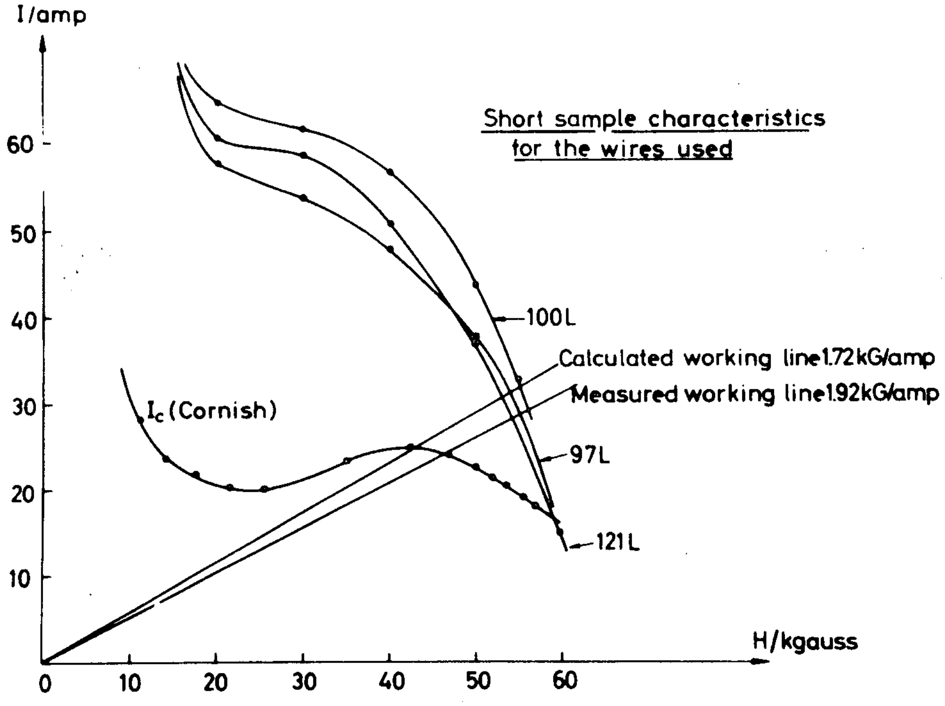

Fig. 2.4.1. Short sample characteristics of the wires used, expected coil characteristic and calculated and measured working lines for the magnet.

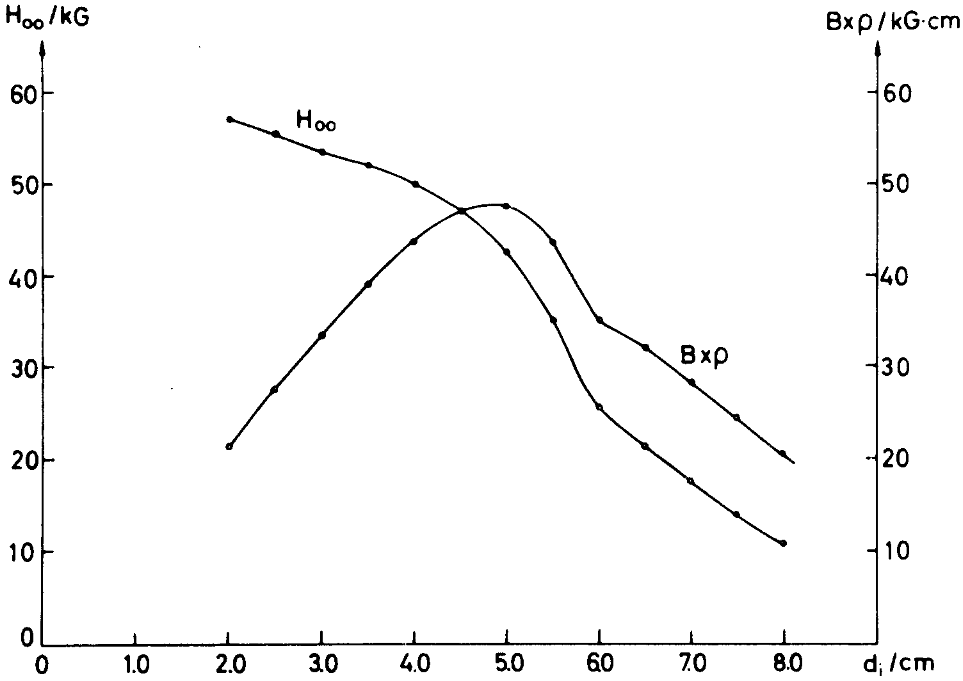

Fig. 2.4.2. Maximum magnetic field H_{oo} and magnetic rigidity Bρ vs the bore of the magnet d_i.

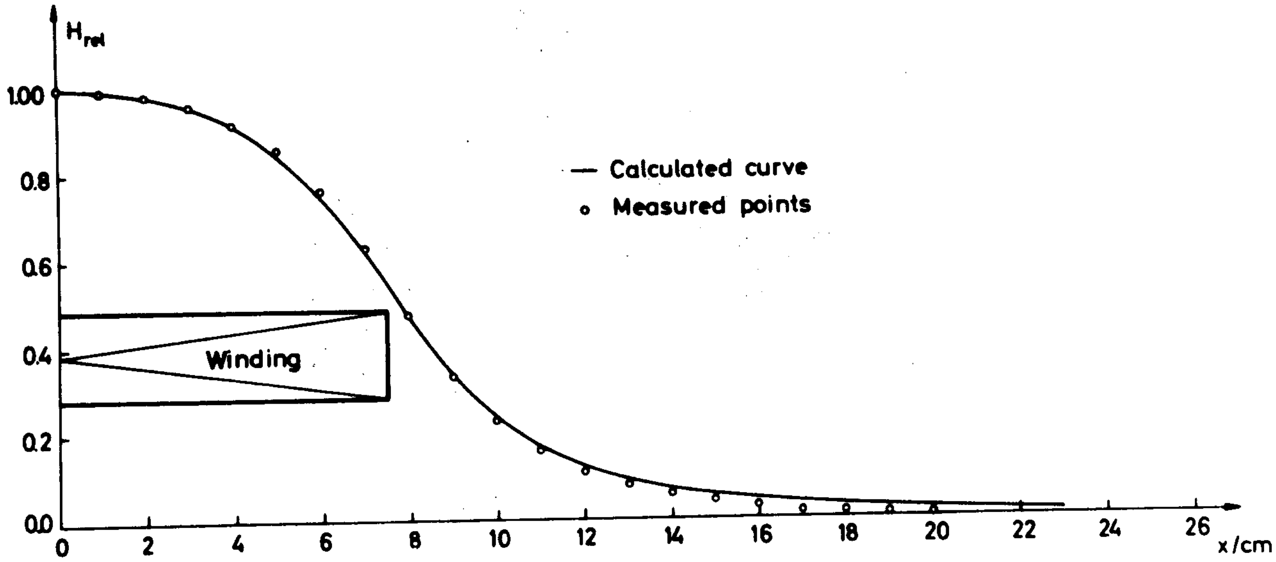

Fig. 2.4.3. Calculated and measured distribution of the field along the axis.

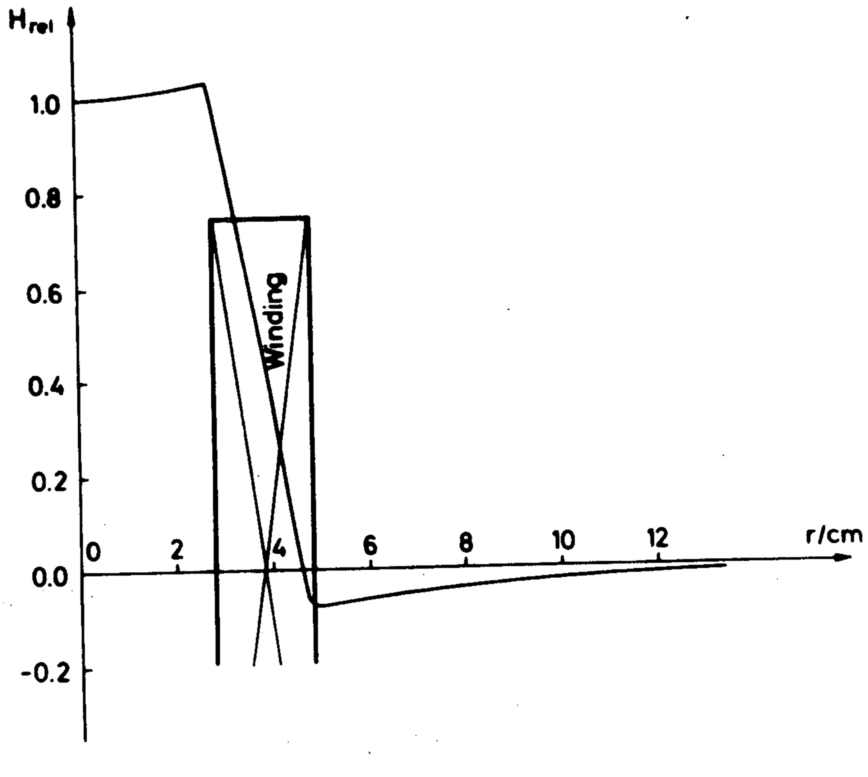

Fig. 2.4.4. Calculated distribution of the field in a plane perpendicular to the axis through the centre of the magnet.

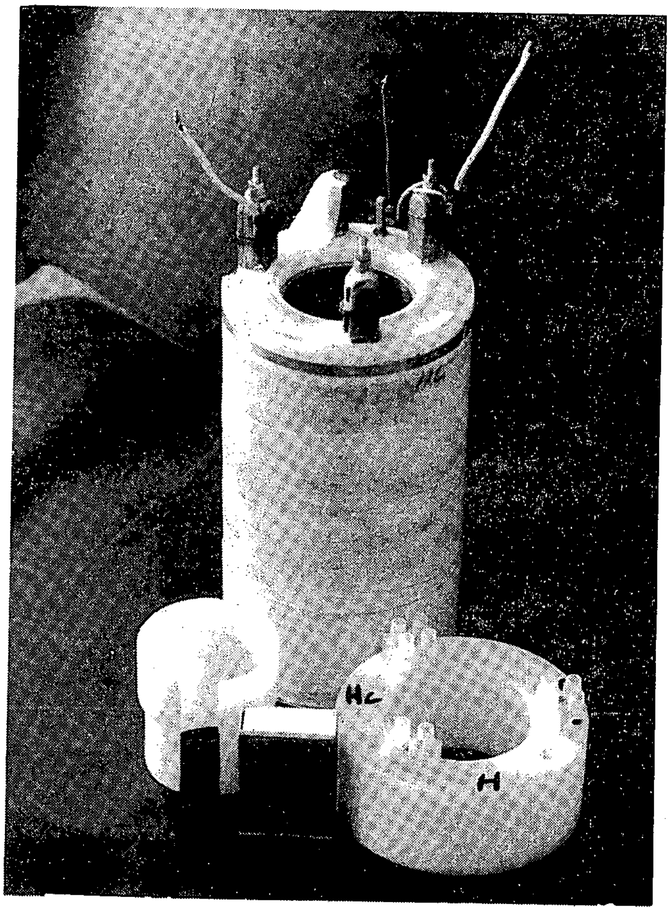

Fig. 2.4.5. The finished magnet.

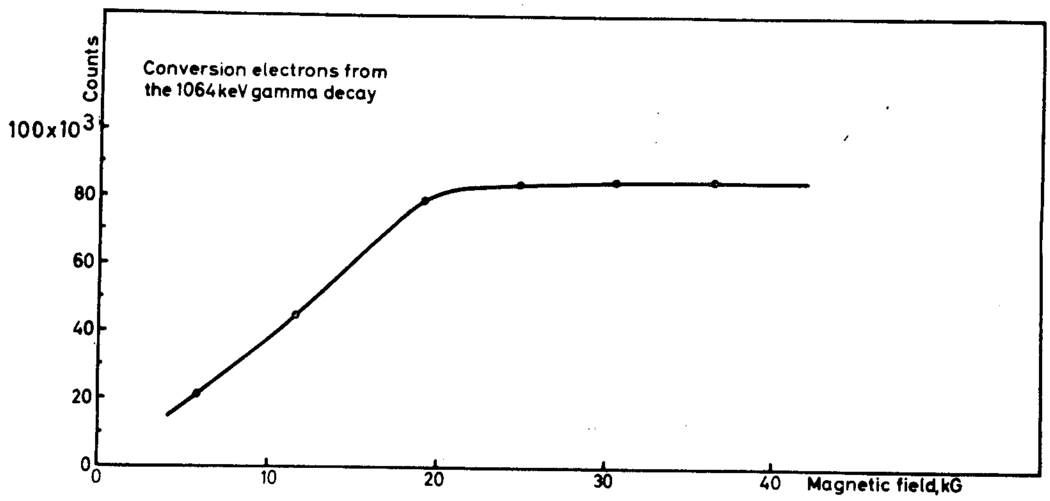

Fig. 3.1. Conversion electrons from the 1064 keV gamma decay caught by the detectors vs the magnetic-field strength.

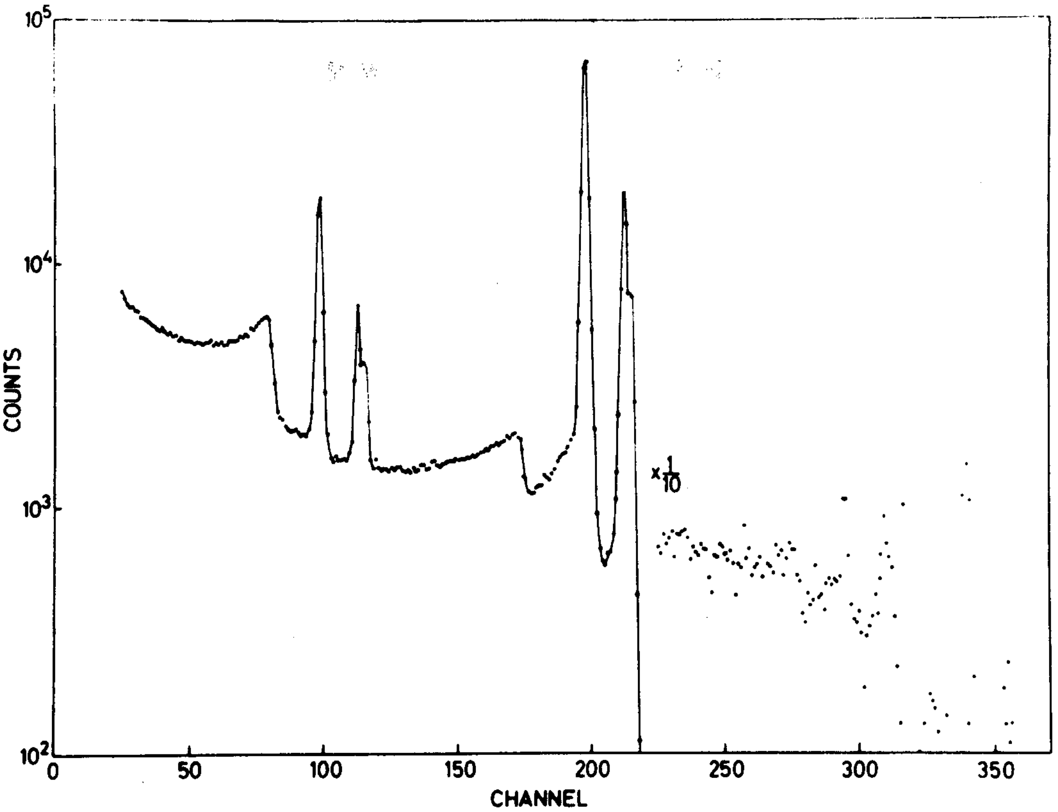

Fig. 3.2. Conversion-electron spectrum of ^{207}Bi taken outside the system.

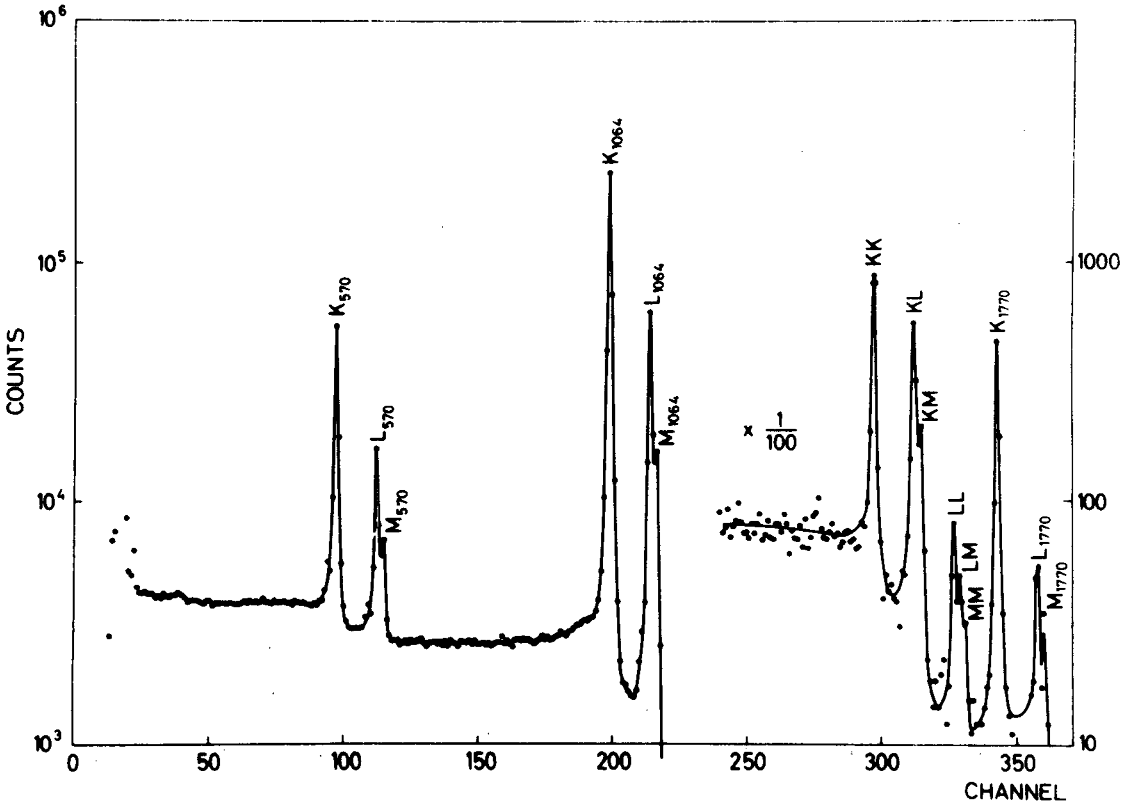

Fig. 3.3. Conversion-electron spectrum of ^{207}Bi taken inside the system with one detector operating.

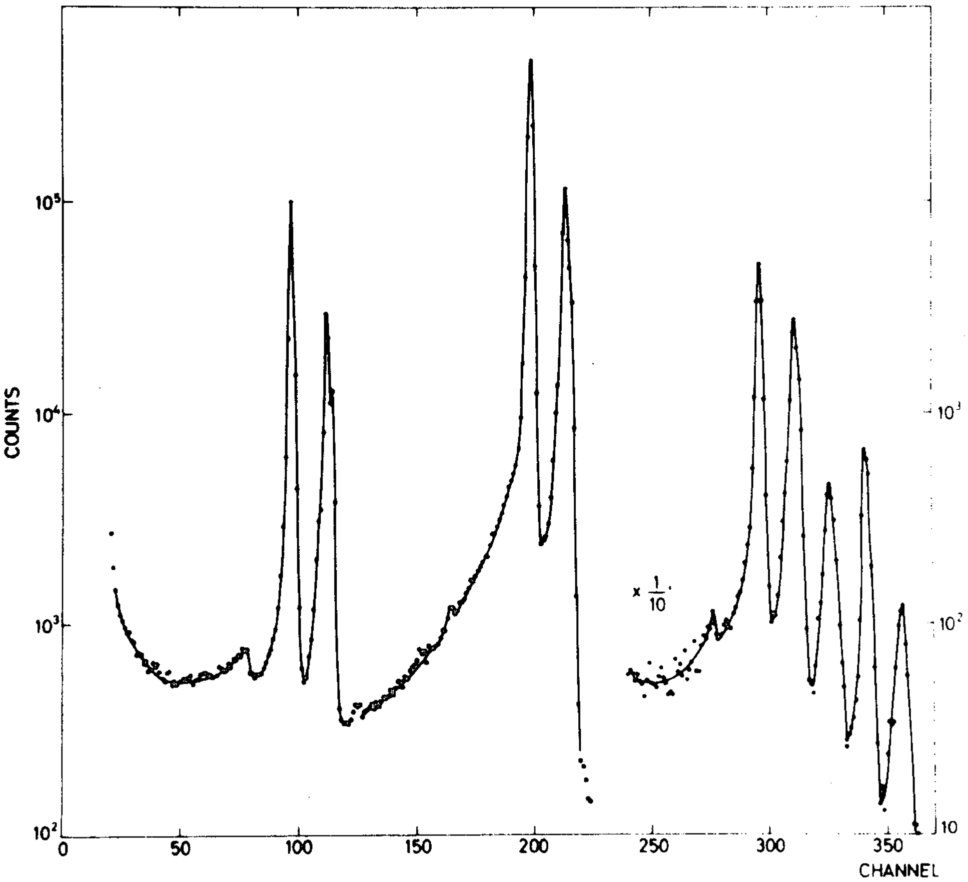

Fig. 3.4. Conversion-electron spectrum of ^{207}Bi taken inside the system with parallel-operating detectors.

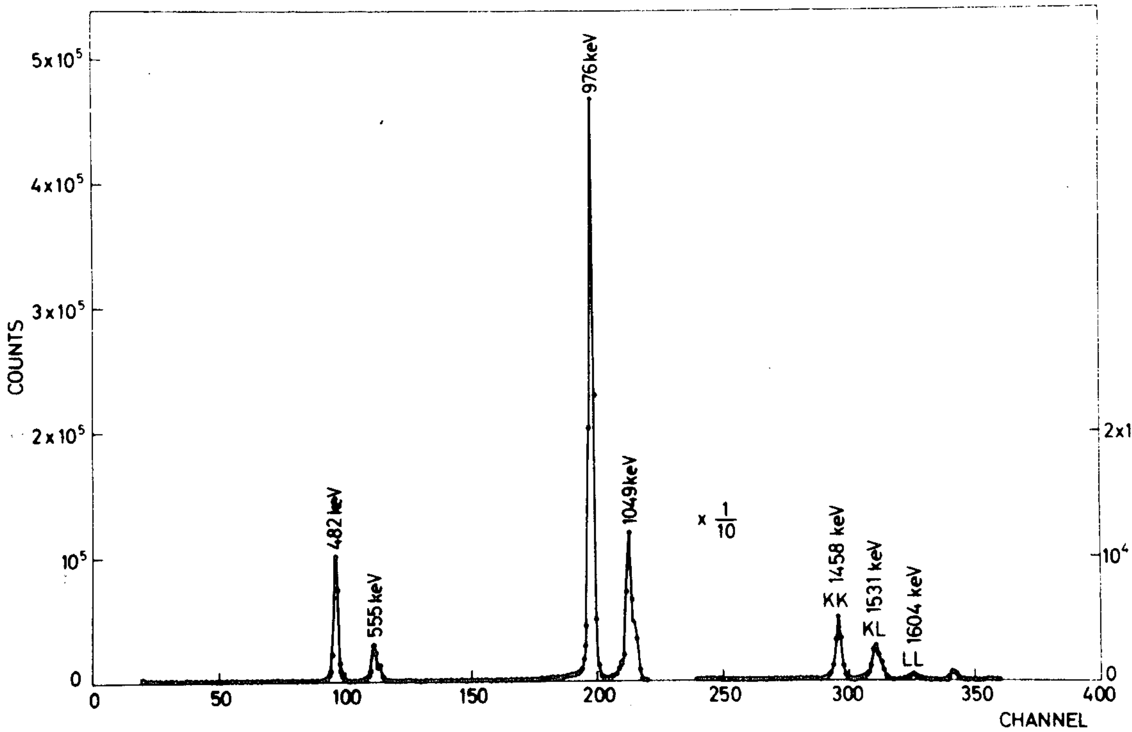

Fig. 3.5. Conversion-electron spectrum of ^{207}Bi taken inside the system with parallel-operating detectors.

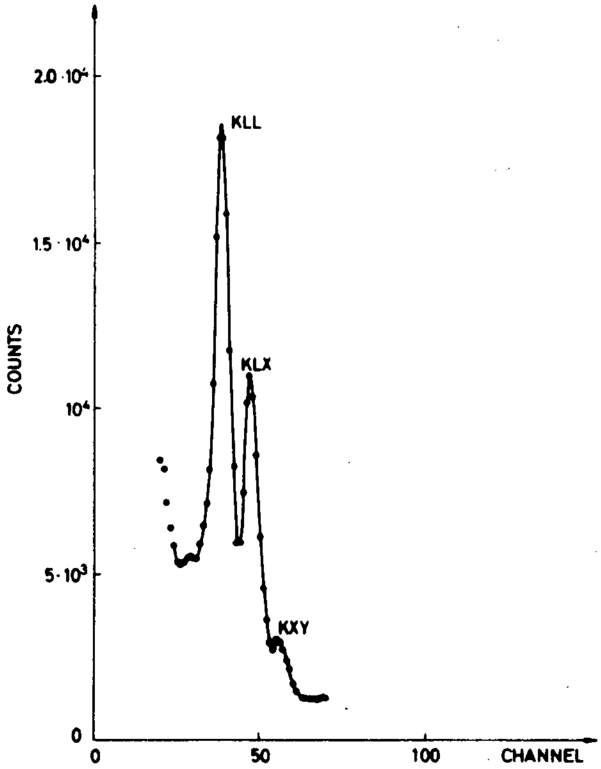

Fig. 3.6. The three main Auger groups from ^{207}Bi.

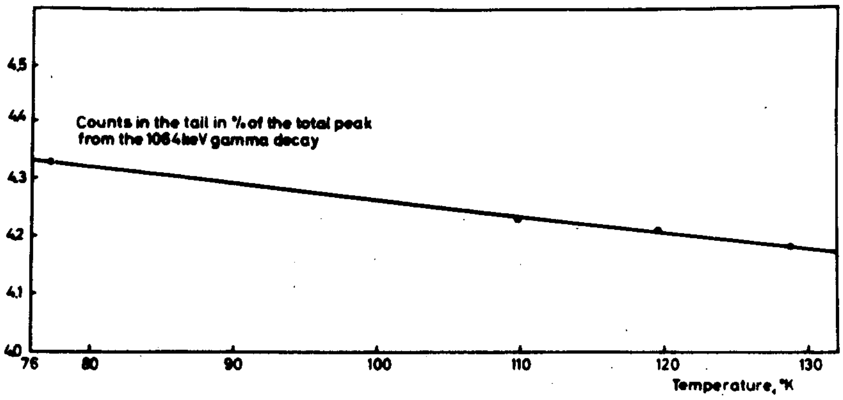

Fig. 3.7. Counts in the tail in per cent of the total peak from the 1064 keV gamma decay vs the temperature of the detectors.

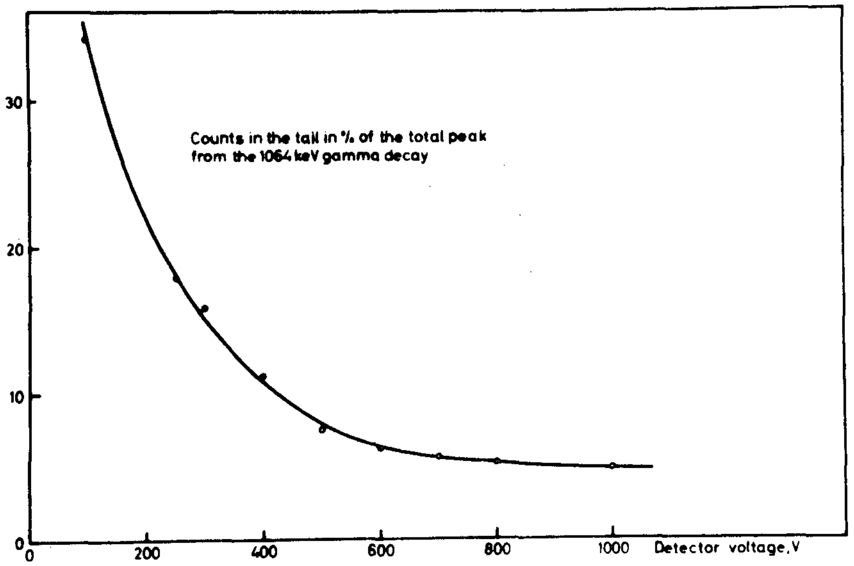

Fig. 3.8. Counts in the tail in per cent of the total peak from the 1064 keV gamma decay vs the voltage of the detectors.

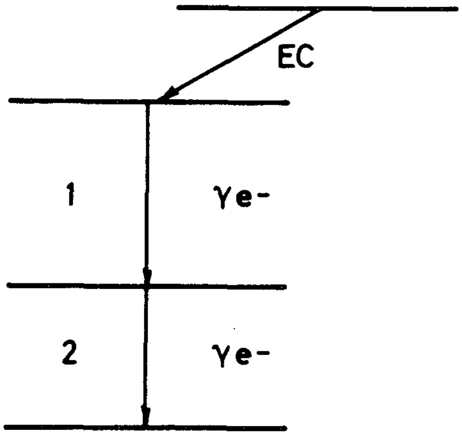

Fig. 4.1. Decay type especially suitable for measuring conversion coefficients in our instrument.

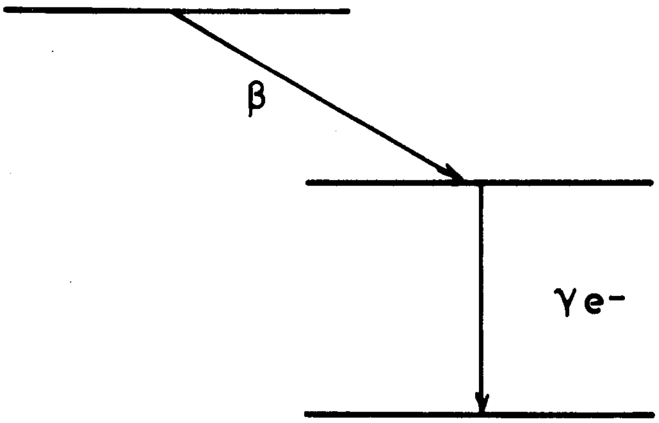

Fig. 4.2. Decay type suitable for measuring conversion coefficient in our instrument.

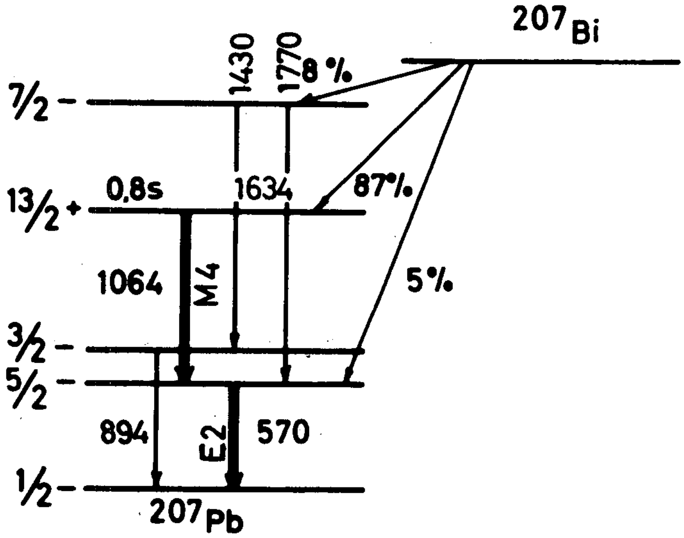

Fig. 4.1.1. The generally accepted decay scheme for ^{207}Bi.

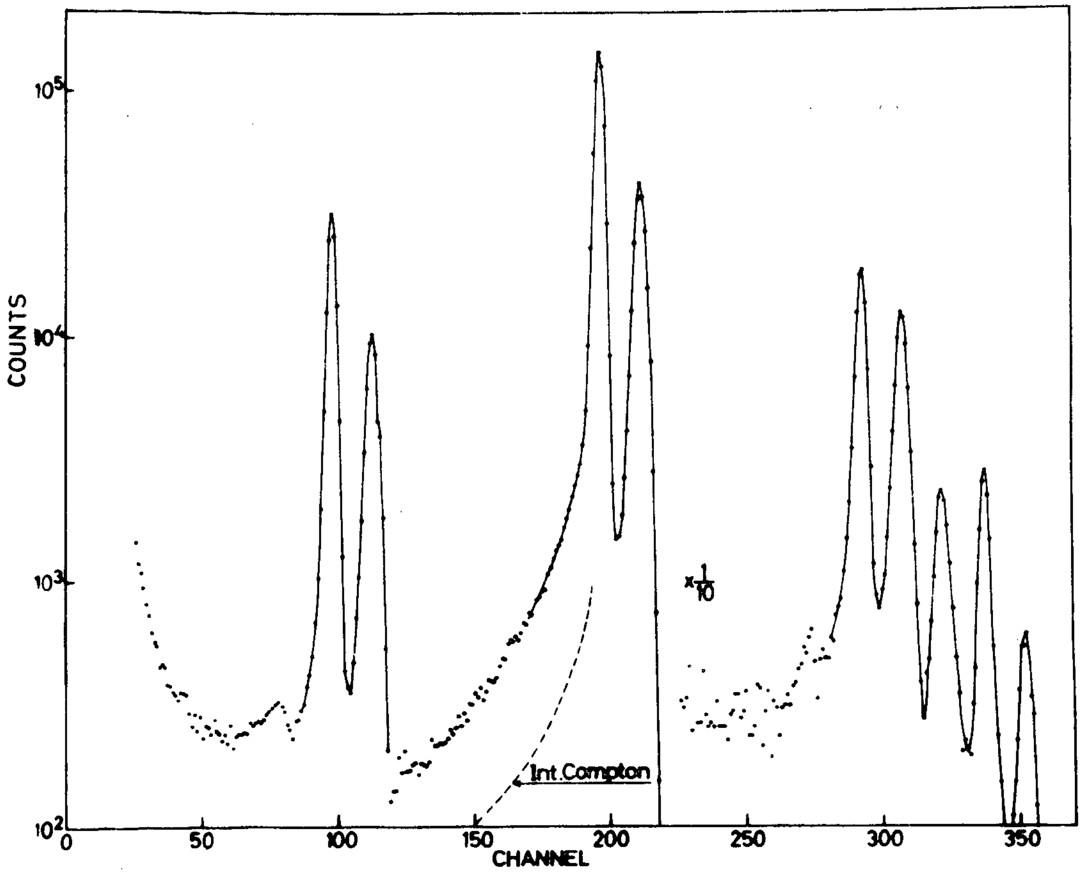

Fig. 4.1.2. Conversion-electron spectrum of ^{207}Bi taken inside the system with parallel-operating detectors.

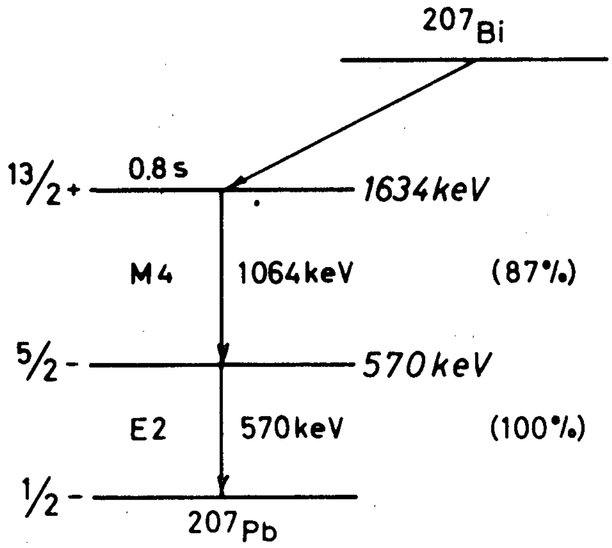

Fig. 4.1.3. Reduced decay scheme for ^{207}Bi.

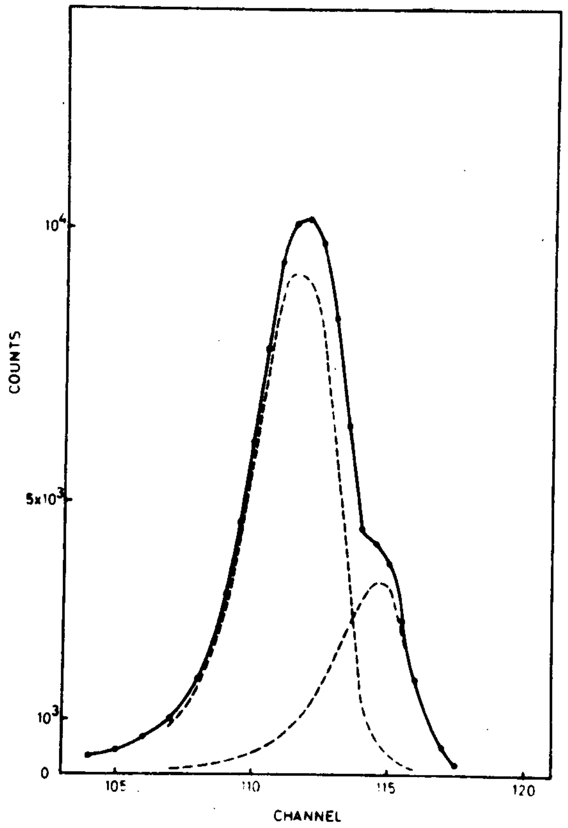

Fig. 4.1.4. Splitting of the LM... peak into the L and M... peaks for the 570 keV decay.

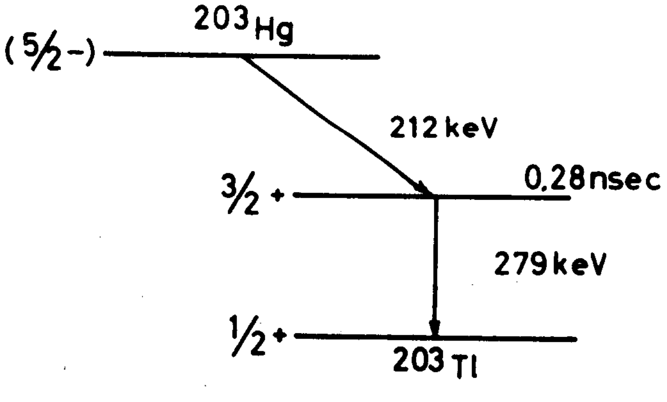

Fig. 4.2.1. The generally accepted decay scheme for ^{203}Hg.

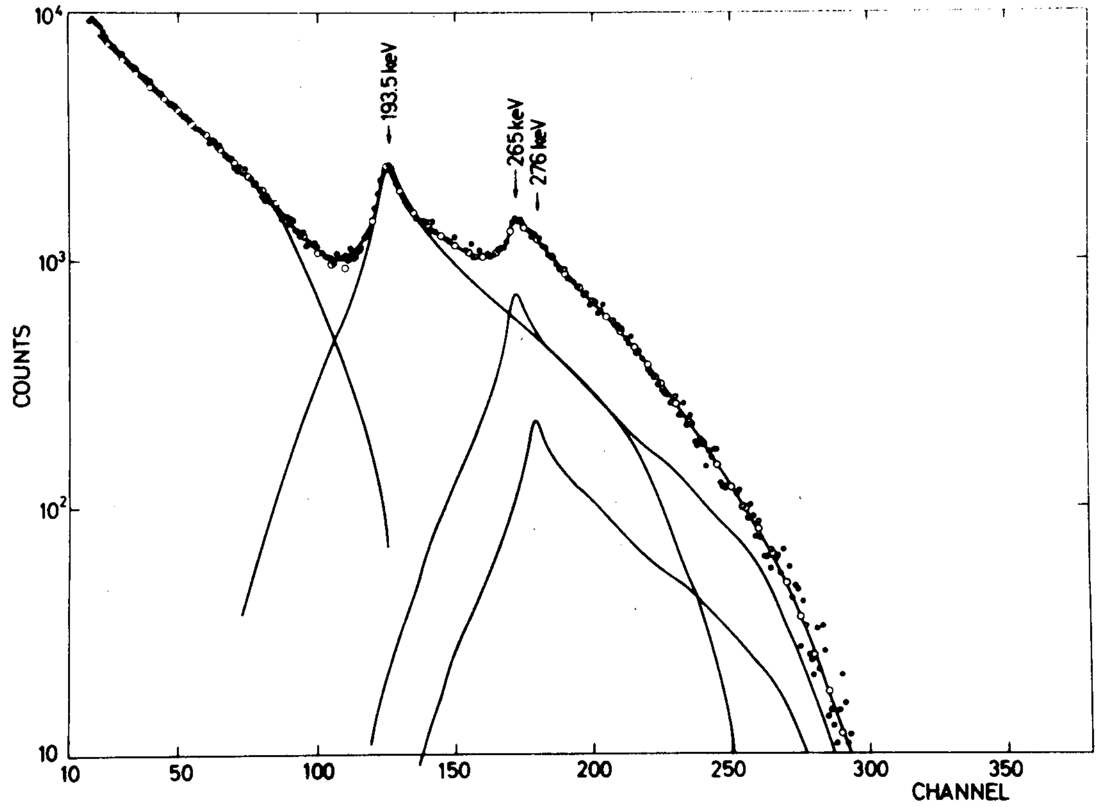

Fig. 4.2.2. Beta- and conversion-electron spectrum of ^{203}Hg taken inside the system with parallel-operating detectors.

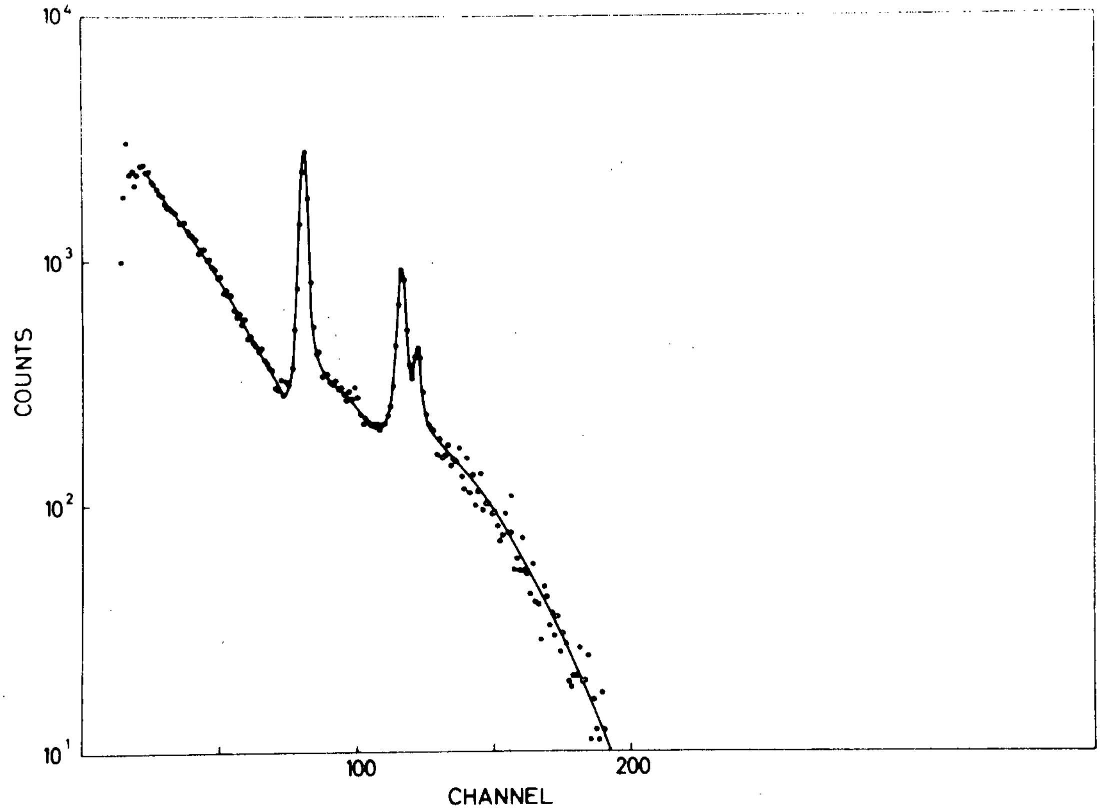

Fig. 4.2.3. Beta- and conversion-electron spectrum of ^{203}Hg taken inside the system with one detector operating.

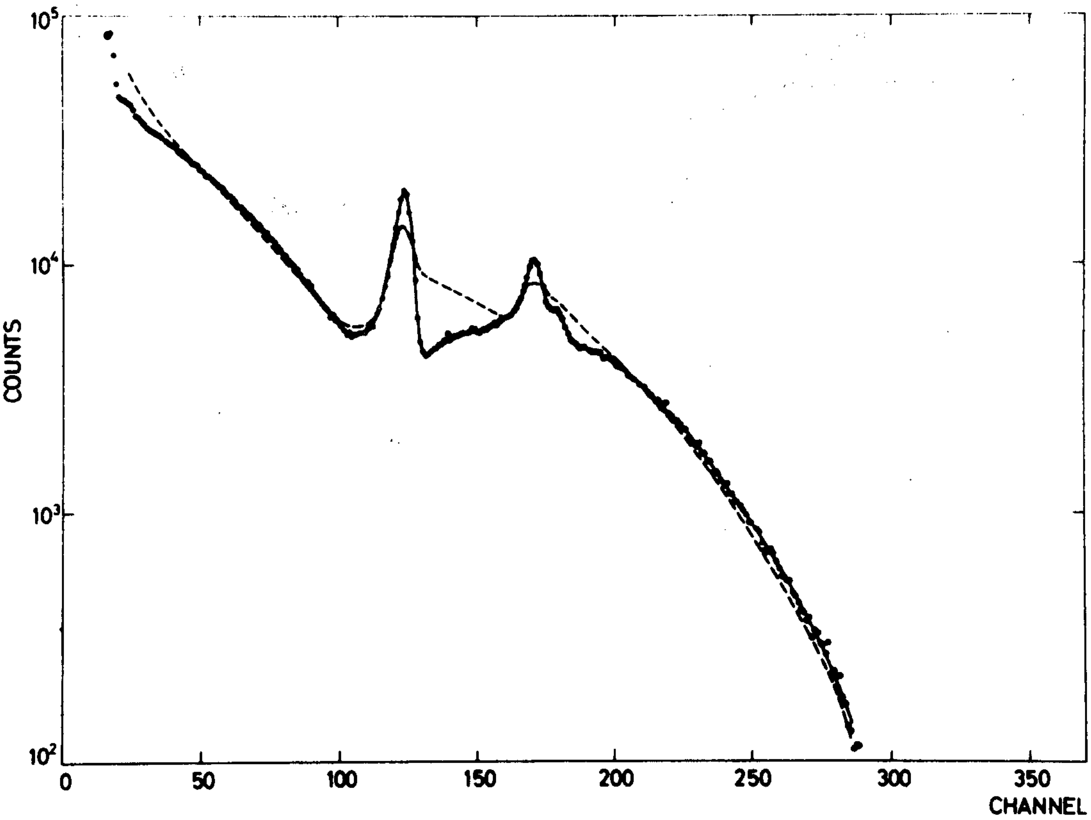

Fig. 4.2.4. Comparison between two spectra similar to that in fig. 4.2.2, but with two different sets of detectors.

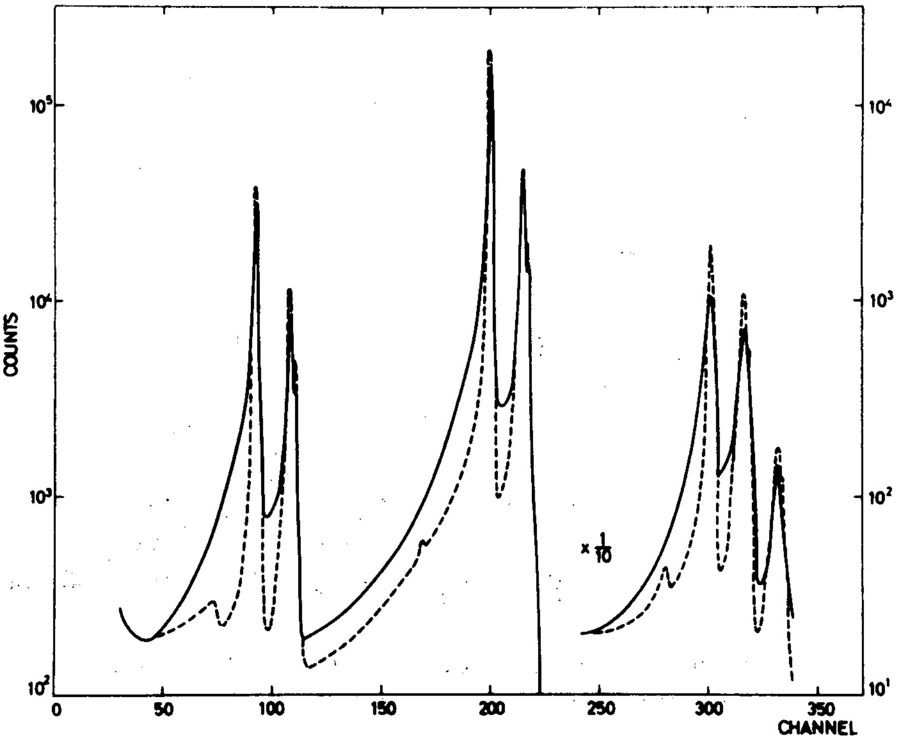

Fig. 4.2.5. Comparison between two conversion-electron spectra of ^{207}Bi taken with two different sets of detectors.

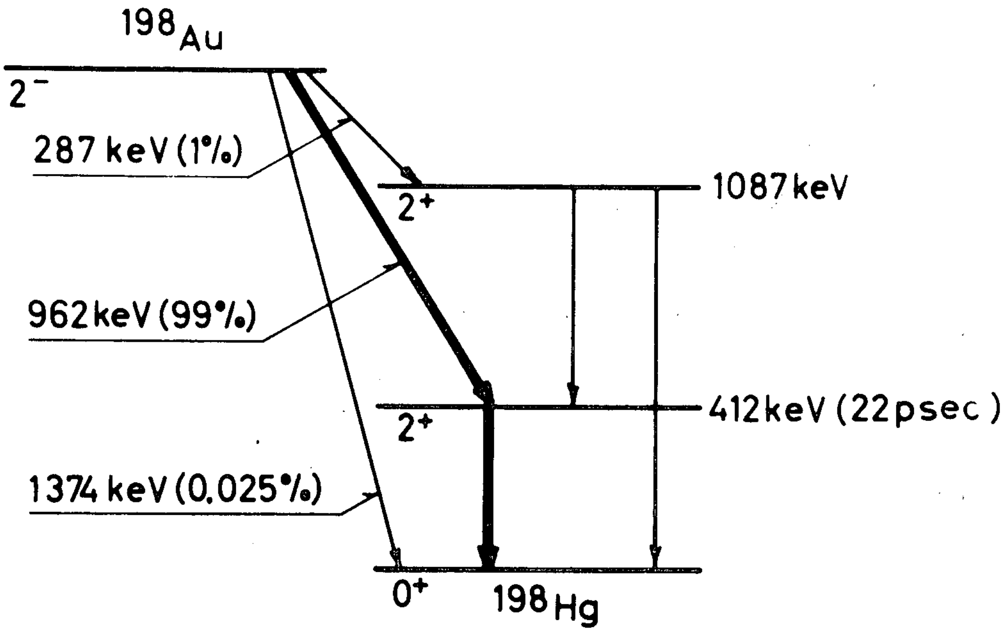

Fig. 4.3.1. The generally accepted decay scheme for ^{198}Au.

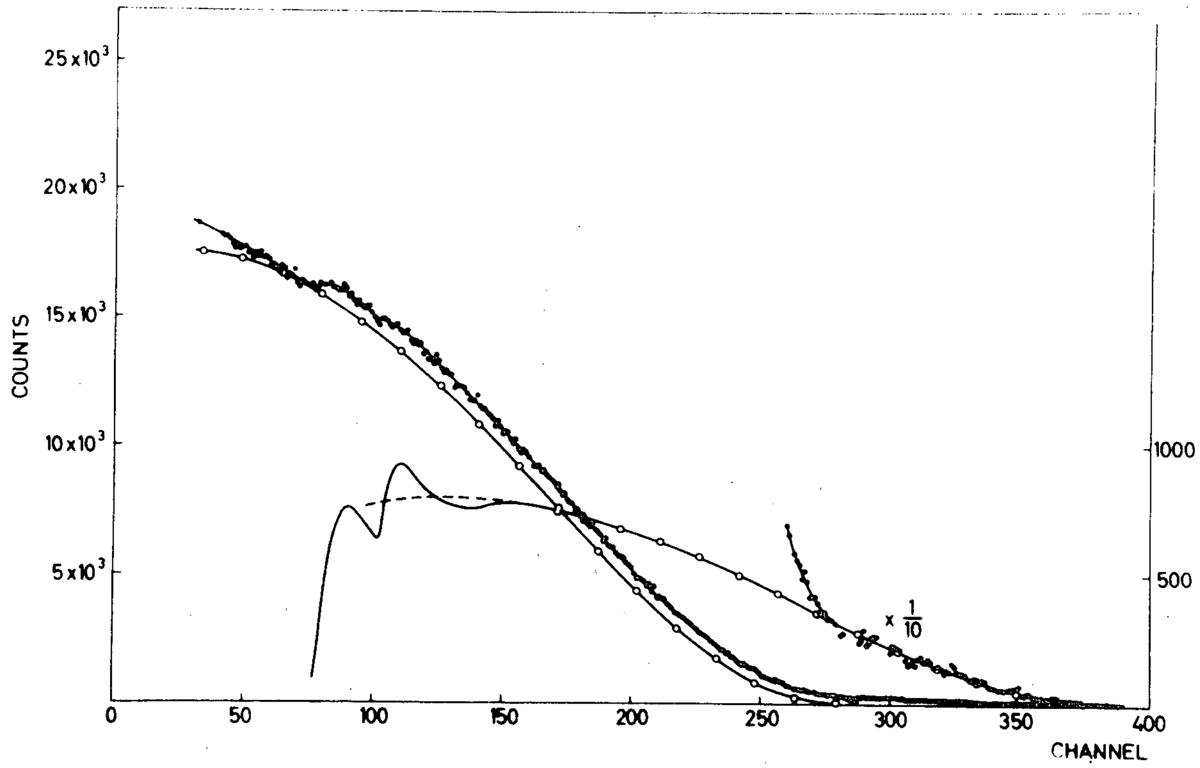

Fig. 4.3.2. Beta- and conversion-electron spectrum of ^{198}Au taken inside the system with parallel-operating detectors.

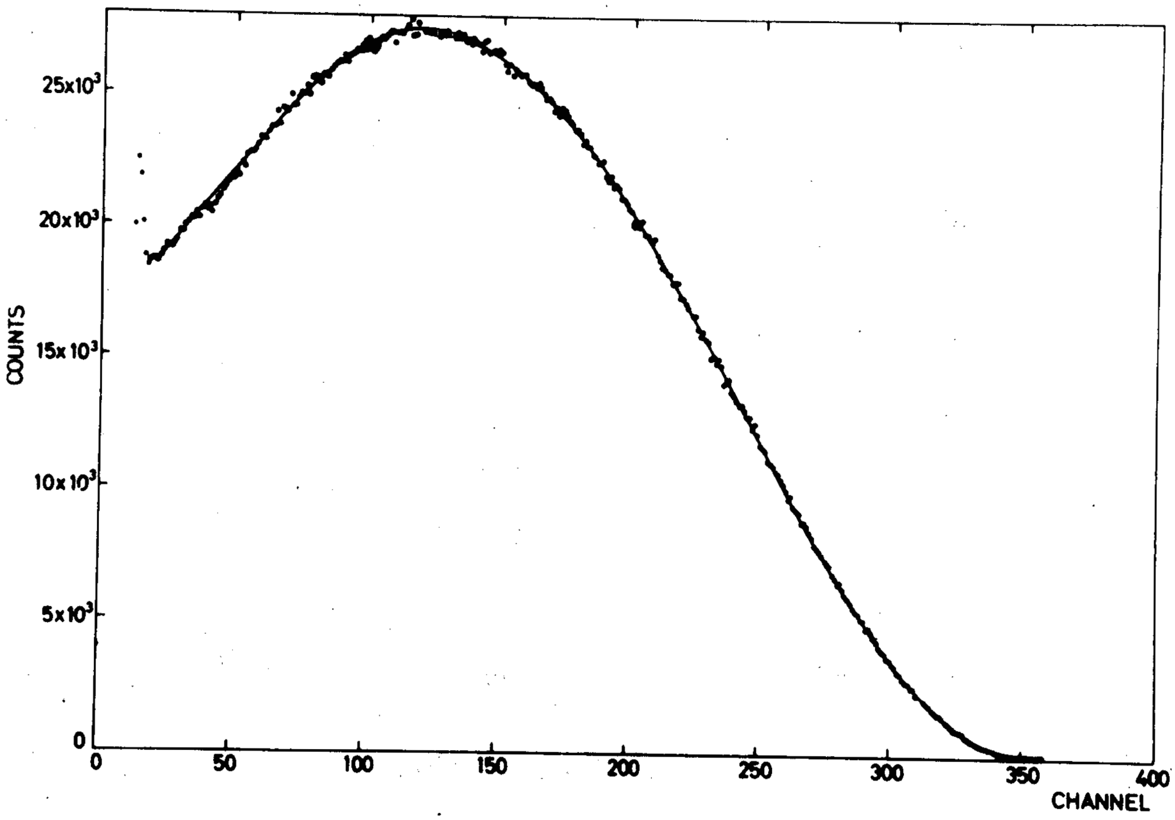

Fig. 5.1.1. Beta spectrum of ^{32}P.

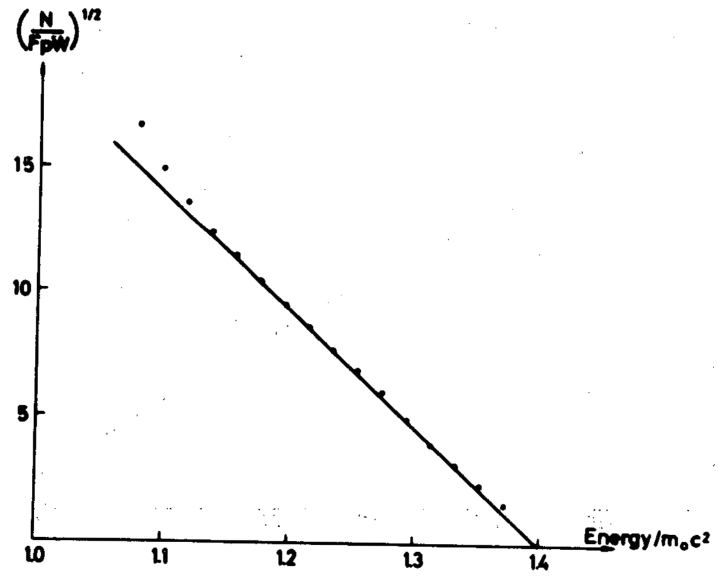

Fig. 5.1.2. FK-plot for ^{203}Hg.

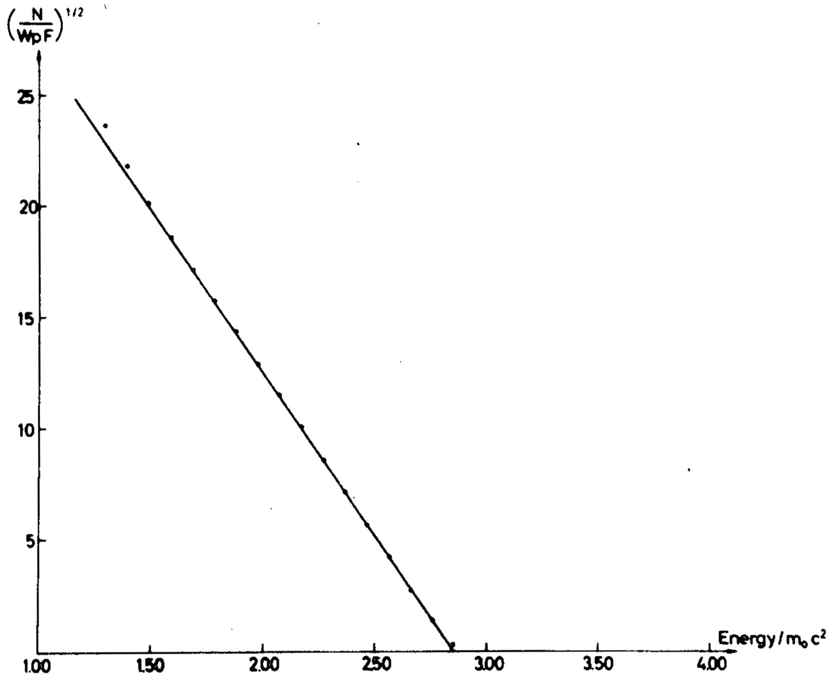

Fig. 5.1.3. FK-plot for ^{198}Au.

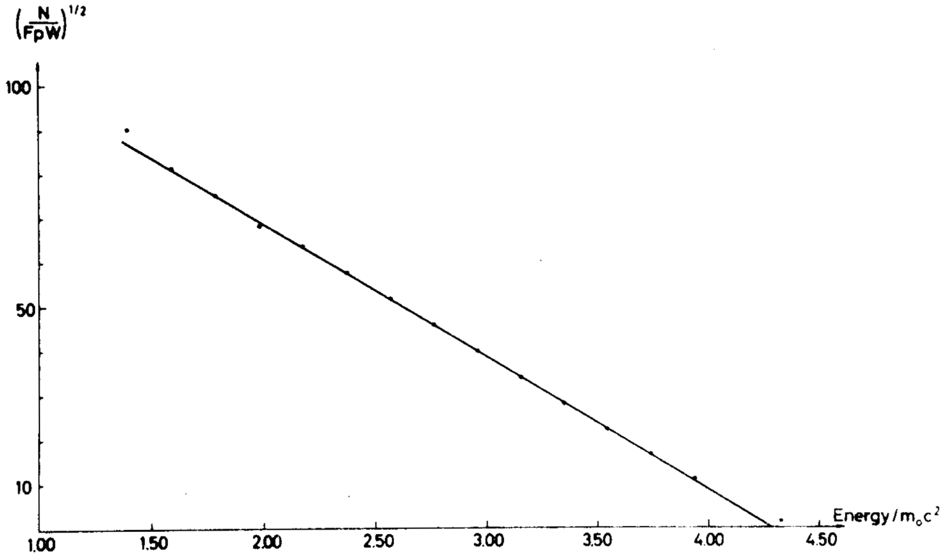

Fig. 5.1.4. FK-plot for ^{32}P.

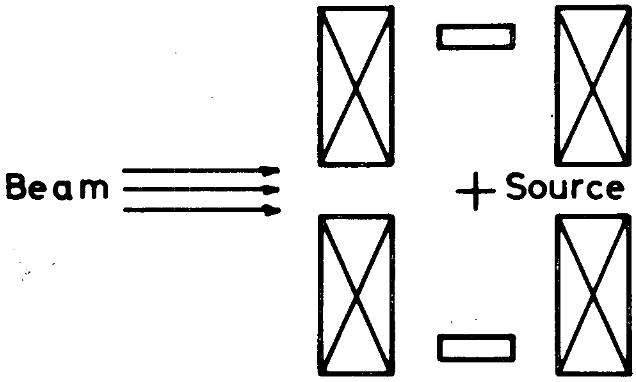

Fig. 6.1. Split-coil system.

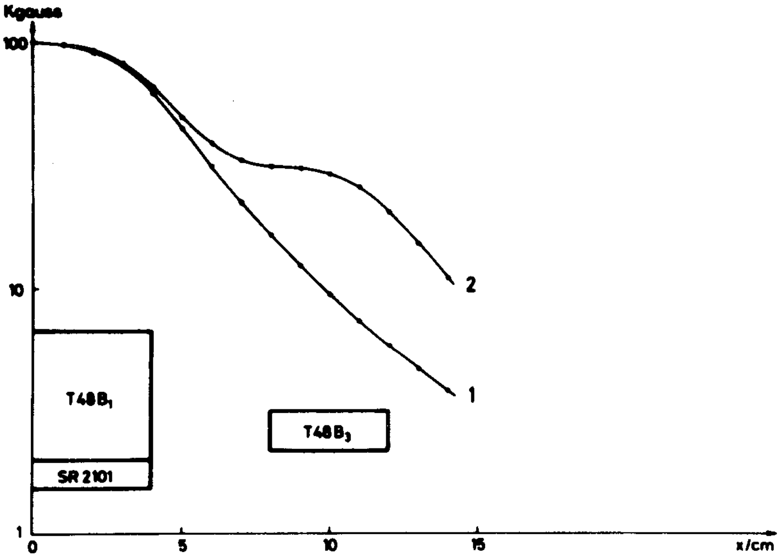

Fig. 6.1.1. Field distribution of the split-coil system; (1) high-field magnet alone at 100 kgauss, (2) high-field magnet at 100 kgauss, low-field magnet at 20 kgauss.

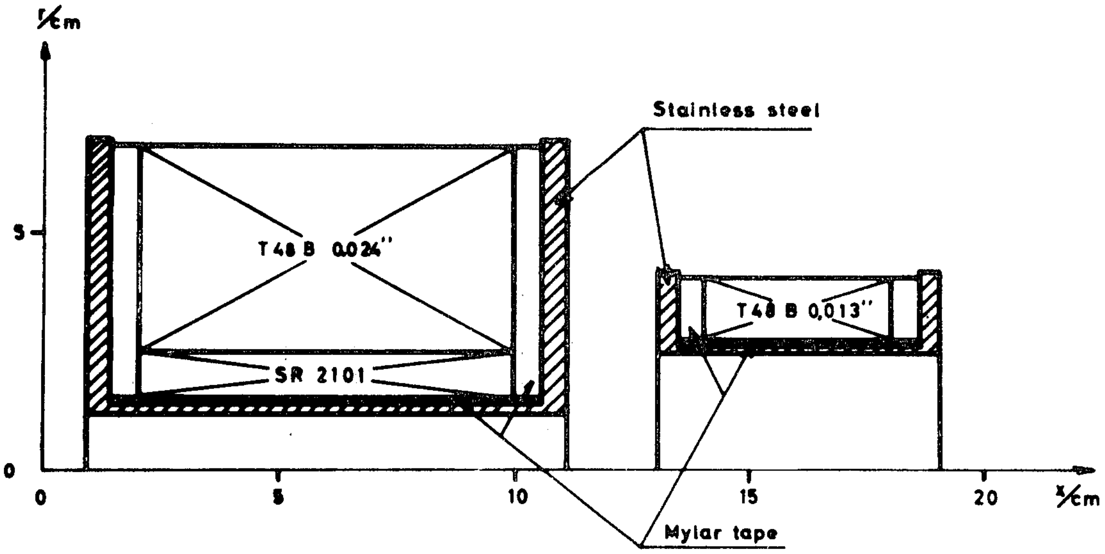

Fig. 6.1.2. Full design of the magnets.

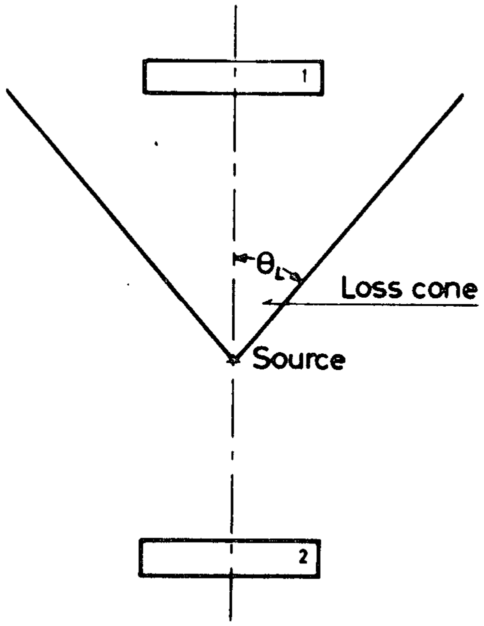

Fig. 6.2.1. The two detectors in an inhomogeneous magnetic field.

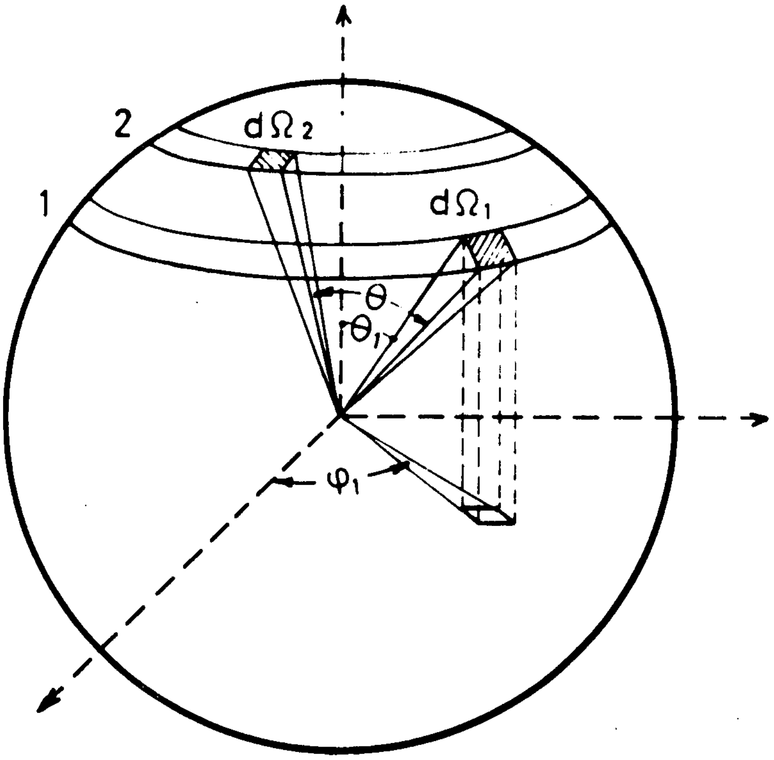

Fig. 6.2.2. The angles of the directions of emission.

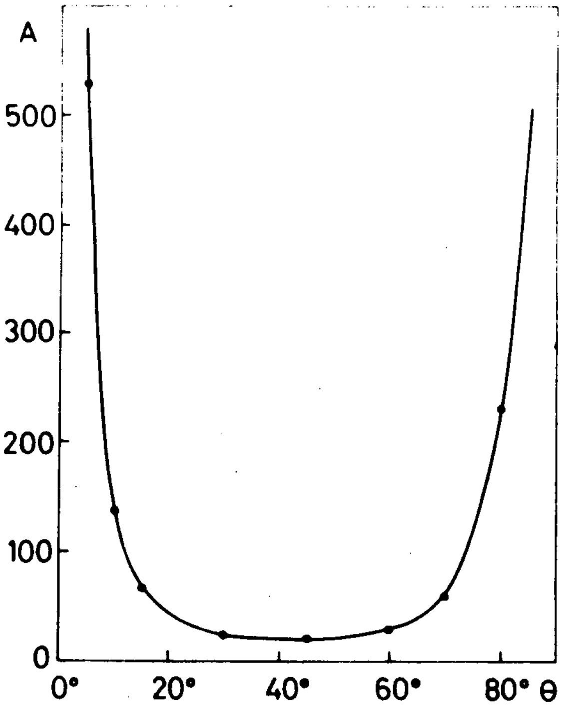

Fig. 6.2.3. The ratio $A = \sqrt{F_1(\theta_1)/F_2(\theta_1)}$ vs θ_1.

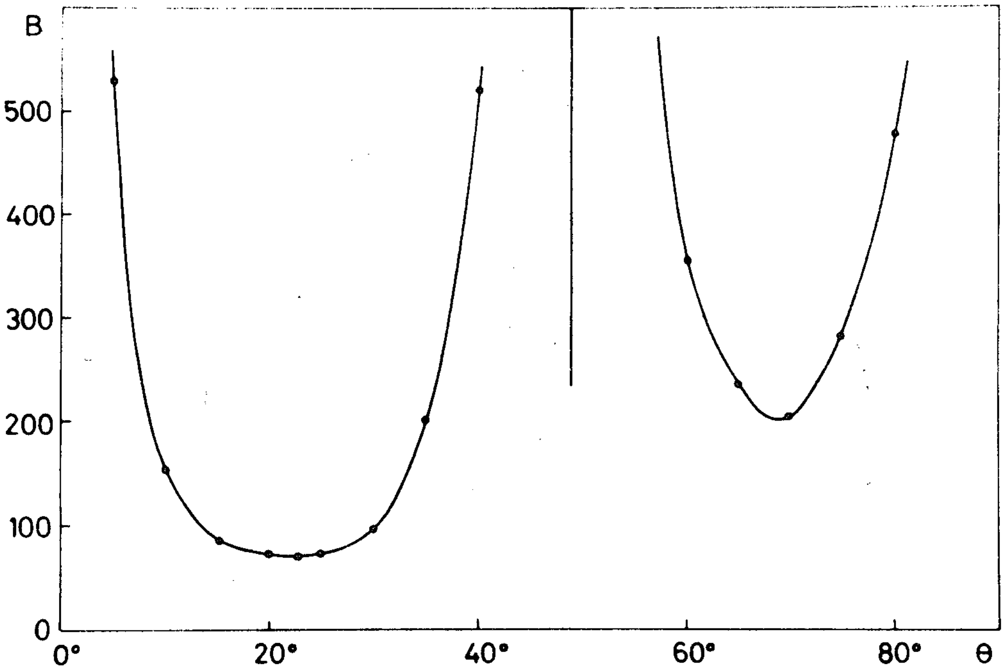

Fig. 6.2.4. The ratio $B = \sqrt{F_1(\theta_2) + F_2^2(\theta_2)\, F_1(49.1)/F_2^2(49.1)}/F_4(\theta_2)$ vs θ_2.

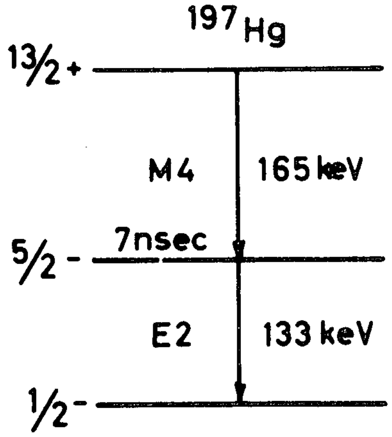

Fig. 6.2.5. The generally accepted decay scheme for ^{197}Hg.

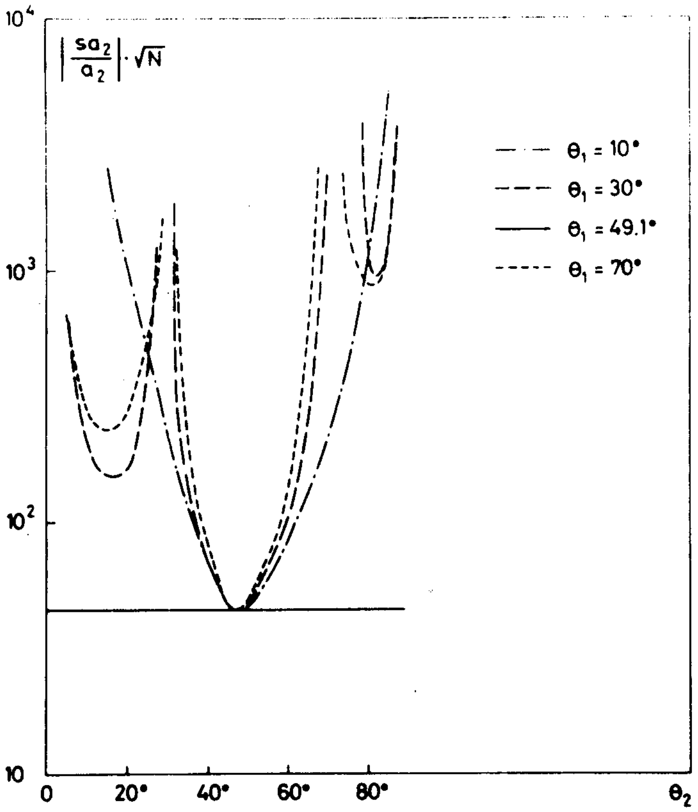

Fig. 6.2.6. The relative uncertainty at a_2 for different choices of angle combinations for ^{197}Hg.

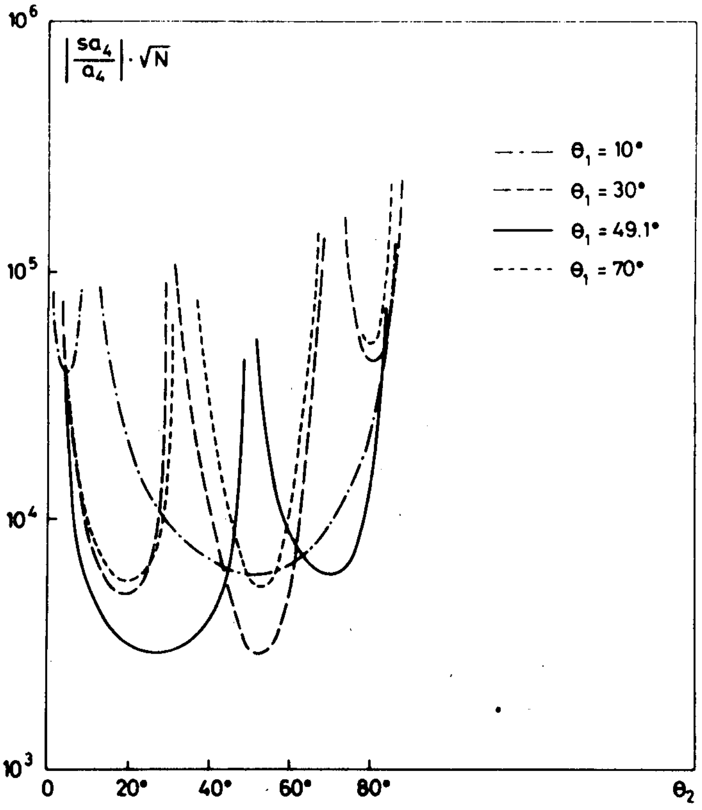

Fig. 6.2.7. The relative uncertainty at a_4 for different choices of angle combinations for ^{197}Hg.

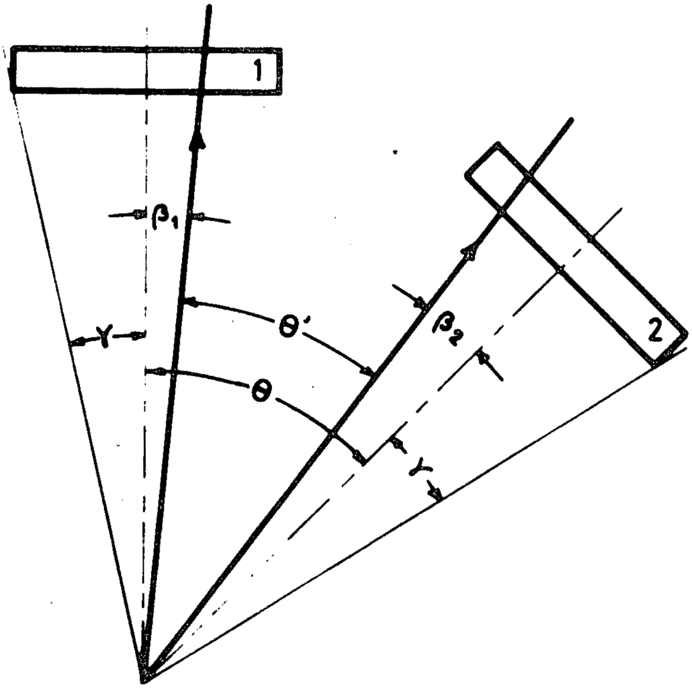

Fig. 6.2.8. Conventional set-up for angular correlation measurement.